# Optimization of Near Field Coupling for Efficient Power Transfer Utilizing Multiple Coupling Structures

Devin Wells Williams

Thesis submitted to the faculty of the Virginia Polytechnic Institute and State University in partial fulfillment of the requirements for the degree of

Master of Science
In
Electrical Engineering

Majid Manteghi
William Davis
Gary Brown

May 3, 2011
Blacksburg, VA

Keywords:
*magnetic resonant coupling, wireless energy transfer, matching networks, magnetic induction*

# Optimization of Near Field Coupling for Efficient Power Transfer Utilizing Multiple Coupling Structures

Devin W. Williams

## (ABSTRACT)

A rise in the need for dynamic energy allocation has been associated with the saturation of available portable wireless electronic devices. Currently, the methods for transmitting this energy efficiently have been limited to a number of options, including near field resonant magnetic coupling. Previous research with mid-range ($d \approx 4r$) wireless power transfer has resulted in coupling efficiencies of close to 40%. In order to increase efficiency in transfer a more directive transmission system was developed using a phased array. Coupling networks were used to shift the resonance of the coupling device, leading to a tightly coupled network by array phasing. Coupling networks for the phased array were optimized using a hybrid combination of a full wave Method of Moments simulation with circuit simulation. Results were validated in a full wave simulator, and field results were shown during resonance. S-parameter results show simulated transfer efficiencies of 70% (-1.5dB) for a phased array structure and 62.3% (-2.4dB) for a single feed structure. Single feed prototyping S-parameter results show coupling efficiencies of 25% (-5.9dB). All coupling measurements are at a distance $4r$ with reference to the largest transmitting coupler.

# Acknowledgments

I would like to acknowledge all of the people who made this research possible with their support and appreciation. First, I would like to thank my advisor Dr. Majid Manteghi, and my workmates in the VTAG (Virginia Tech Antenna Group) lab for their engineering support and advice. I would also like to thank Dr. William Davis for his input on some engineering aspects to my thesis as well as his advice for proper communication of work. The aforementioned expertise tremendously helped along the research process.

I would also like to thank and give my love to my family Kelly, Randye, and Karlye and my close friends at Virginia Tech for their unending support during the last two years. They are always there for me and hope to be there for them in the future.

# Table of Contents

# Table of Figures

# List of Tables

# Chapter 1: Introduction

Wireless energy transfer has been the topic of research for over a century. Motivations for this research have come in a variety of forms, and, until the last decade, have primarily been associated with high power, large scale transfer. The resurgence of the area of resonant coupling have spawned many different approaches to the application and integration of wireless energy transfer. The following chapter will delve into the history behind the concept of resonant magnetic coupling, provide motivations for the research in this paper, and describe some of the primary principals behind the research.

## 1.1 History/Developmental Theory

The investigation of what would come to be known as resonance started in the late 1800's with Heinrick Hertz, a German engineer and physicist. Hertz noticed that as he created a potential spark there would be a force that would act on conducting needles a distance away from the spark. He theorized that the "rapid oscillations" of electrical current had something to do with the force experienced on these light conductors[1]. Hertz had begun building what is described as modern electrodynamics. In his famous experiment, Hertz set a spark gap on the opposite side of a coil transformer, and was able to measure the intensity of the spark gap under certain situations. *Natural resonance* was the phenomena that Hertz was experiencing when observing this phenomena, and is the fundamental basis for many radiating antennas. Around 20 years later a Serbian born American citizen named Nikolai Tesla made a resurgence in the area of wireless transmission of energy. Tesla proposed a facility, named Wardenclyff, to become the branching point for a worldwide network of transmission points, in order to effectively send energy all over the planet. Figure 1-1 is an illustration of the proposed concept in Tesla's filed patent[2, 3].

During this time, the theory of electromagnetics, specifically practicality related to magnetic circuits and phenomena was making large strides. In 1900 Sir Alfred Ewing, a Scottish physicist and engineer, published a book describing the inductive properties of magnetic materials. He is known for coining the term hysteresis. He describes the electromagnetic concept known *magnetic flux* as the magnetic analog to Ohm's law, or as he states the "equation of conduction"[4]. This is the beginning of the theory involving magnetic induction. He states that

$$flux = \int Bds$$

and defines the magnetic permeability of a space, $\mu$,

$$B = \mu H$$

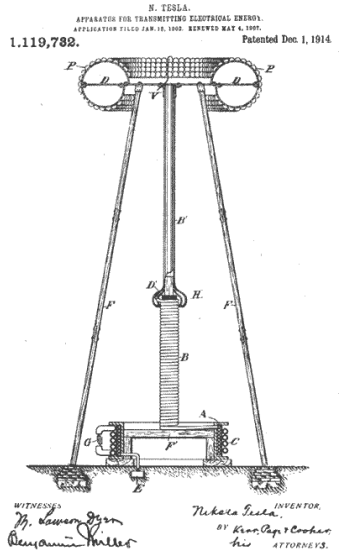

Figure 1-1 Early Design for Wireless Energy Transmitter

which led to the conclusion that

$$flux = \frac{\int Hdl}{\int \frac{dl}{\mu s}}$$

Of course when used in combination with Maxwell-Faraday's law the correlation between the magnetic field and the induced potential can be described by

$$\varepsilon = -\frac{d\varphi}{dt}$$

This derivation is the key to determining the effect of a current source on another conducting element. The fundamental basis for describing inductive coupling lies in this correlation. Toward the middle of the 20th century and beyond, there was a great deal of research in the concept of transformers, and other devices which operate on the basis of inductive coupling, including magnetorestrictive devices[5], and cross talk between devices[6-8].

From these exploration it was realized that a more efficient method for transmitting energy purposefully (not from parasitic inductance) can be implemented. This method, created by the sharing of stored energy, is called *resonant coupling*. In order to introduce the topic of resonant coupling, a model for the system must be present. Take for instance the model for two loosely coupled inductors (known as a transformer) seen in Figure 1-2. We can define the power efficiency between the two networks as

$$\eta = \frac{P_l}{P_{in}} = \frac{V_l I_l^*}{V_s I_s^*}$$

For purely inductive coupling it is assumed that

$$Z_l = R_l\ \Omega$$

which would lead to the power being transferred as

$$P_l = \frac{V_l^2}{Z_l}$$

Notice that for the purely inductive case we have

$$V_l = V_{induced}\left(\frac{Z_l}{Z_l + R_r + j\omega L_r}\right) V$$

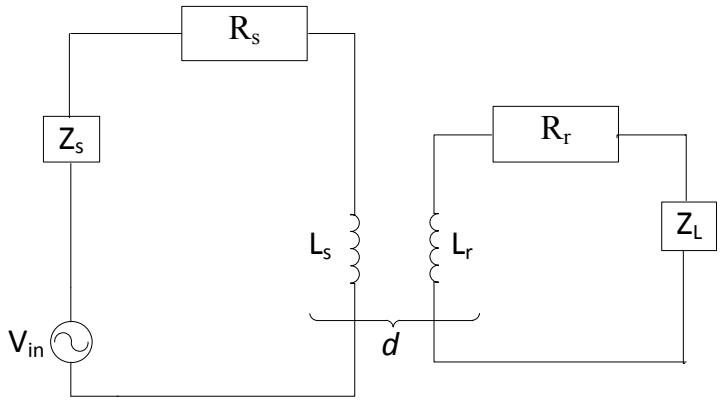


Figure 1-2 Simple Inductively Coupled RLC Networks

For differing values of $\omega$ it can be shown that not only does the induced field changes but the impedance to the load also increases. For a variation in $d$, it can also be shown that the induced voltage on the receiving inductor also varies by Biot-Savart's equation[9]:

$$B = \int \frac{\mu_0}{4\pi}\left(\frac{Idl \times \bar{\boldsymbol{r}}}{|r^2|}\right)\frac{A}{m}$$

This issue that arises is that up to this point we can see that there isn't a conjugate reactance to share stored energy with the inductor. If a reactance is placed within the load, $Z_l$, and the source, $Z_s$, that matches the inductor ($-j\omega L_s\ or\ -j\omega L_r$) impedance at resonance, then it can be shown that the power delivered to the source is

$$P_l = \frac{\left[V_{ind}\left(\frac{R_l}{R_l + R_r}\right)\right]^2}{Z_l}$$

where $R_l$ is the real part of the load impedance.

This model, however, is a somewhat incomplete model of what can be described as resonant coupling, the reason being that the impedance of the two networks may not be matched. Figure 1-4 displays the model for a 2 port Z-parameter matrix. There is a mutual impedance between both of the networks, in this case, that is directly related to the mutual inductance that $L_s$ has on $L_r$. The $Z_{l2}$ parameter adds a reactance between networks, that must be accounted for optimal power transfer to occur. In this case it can be shown that matching must occur between networks. This mutual inductance, *M*, as described by Shadowitz [9], is a coefficient that describes the amount of current that is seen on a loosely coupled inductor as a result of current flow on another inductor. The mutual inductance is described as

$$\phi_{ij} = M_{ij} I_j$$

and the equation for the induced voltage in $L_r$ becomes

$$V_{ind} = L_r \frac{di_1}{dt} + M_{12} \frac{di_2}{dt}$$

$$M_{12} = M_{21}$$

If the reactance in the load $Z_l$ can compensate for the induced reactance between the inductors of the two networks, then the networks are considered to be *resonantly coupled*, where all reactive elements store no power. The result, for the case in Figure 1-5 would be

$$P_l = \frac{V_s \left( \frac{R_l}{R_l + R_{loss}} \right)}{{R_l}^2}$$

It is prudent, then, to understand how this might be designed from a network and circuit perspective. Take for instance the 4 element RLC circuit in Figure 1-3. In order to understand, from a design perspective, how the problem should be approached, a method for determining total input impedance should be used.

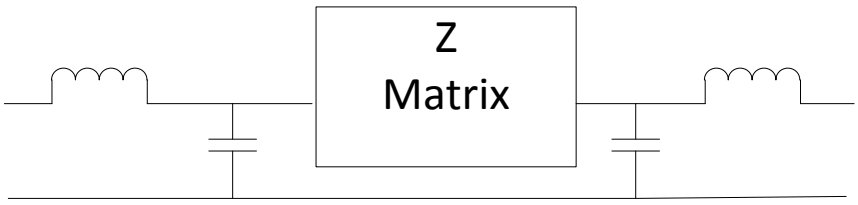


Figure 1-3 Overall Schematic of Resonant Coupling Network

As is illustrated, the mutual coupling between the inductors of both networks has a signature, and this signature is described within the *Z* matrix. The *Z* matrix can thus be expanded for a 2 port network as:

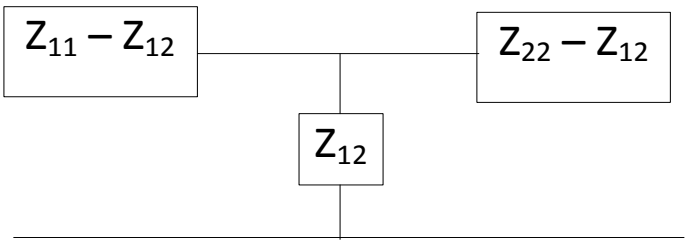


Figure1-4 Block Diagram of Impedances for a Z-Matrix

The network model can then be expanded to include the mutual inductance *Z* matrix as shown in Figure 1-5.

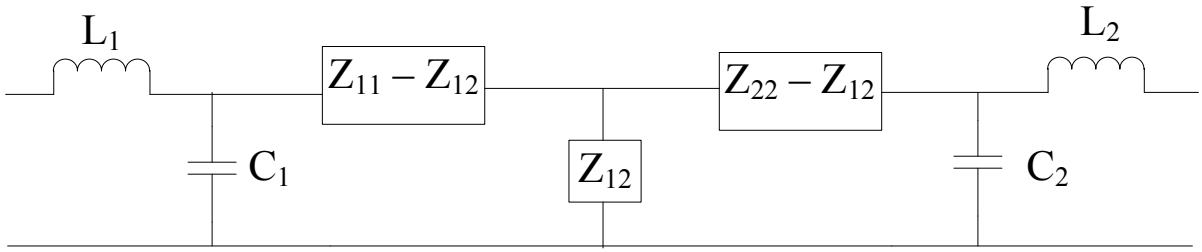


Figure 1-5 Expanded Resonant Coupling Network. The Z-matrix represents the inductive coupling between inductors.

In order to find the impedance seen by either port, the impedance of the network can be expanded in this way:

$$Z_{in} = \Big\{\big\{\{L_1, C_1\} + Z_{11} - Z_{12}, Z_{12}\big\} + Z_{22} - Z_{12}, C_2\Big\} + L_2$$

where {a,b} designates a in parallel with b.

The full derivation of the matching can be seen in Appendix A: Ancillary Figures and Derivations. The expansion leads to set of reactance equations that must be satisfied in order for the network reactance to be zero, which is the condition for resonance (no stored energy). To illustrate how this input impedance characteristic looks over a range of resonance, let us take the case of a 4 element network, with two extraneous inductors mutual coupling to each other. Once optimized (at 125MHz in this case), the element reactances were placed within the expanded input impedance equation. The resulting real and reactive parts of the impedance are displayed in Figure 1-6. As can be see there are two portions were the optimization has found resonance, one at 114MHz, and the other at 125MHz. The 125MHz resonance

seems to show less loss, and is more ideal. This case shows the entire network under the resonant coupling condition. It is important to note, however, that having the input impedance to the network does not directly correlate to the amount of power received at the load, because there may be internal reflections from the network that cause power dissipation. Observing the input impedance only shows the user the amount of power reflected at the port of excitation, which for this case is zero when the imaginary part of the impedance is also zero.

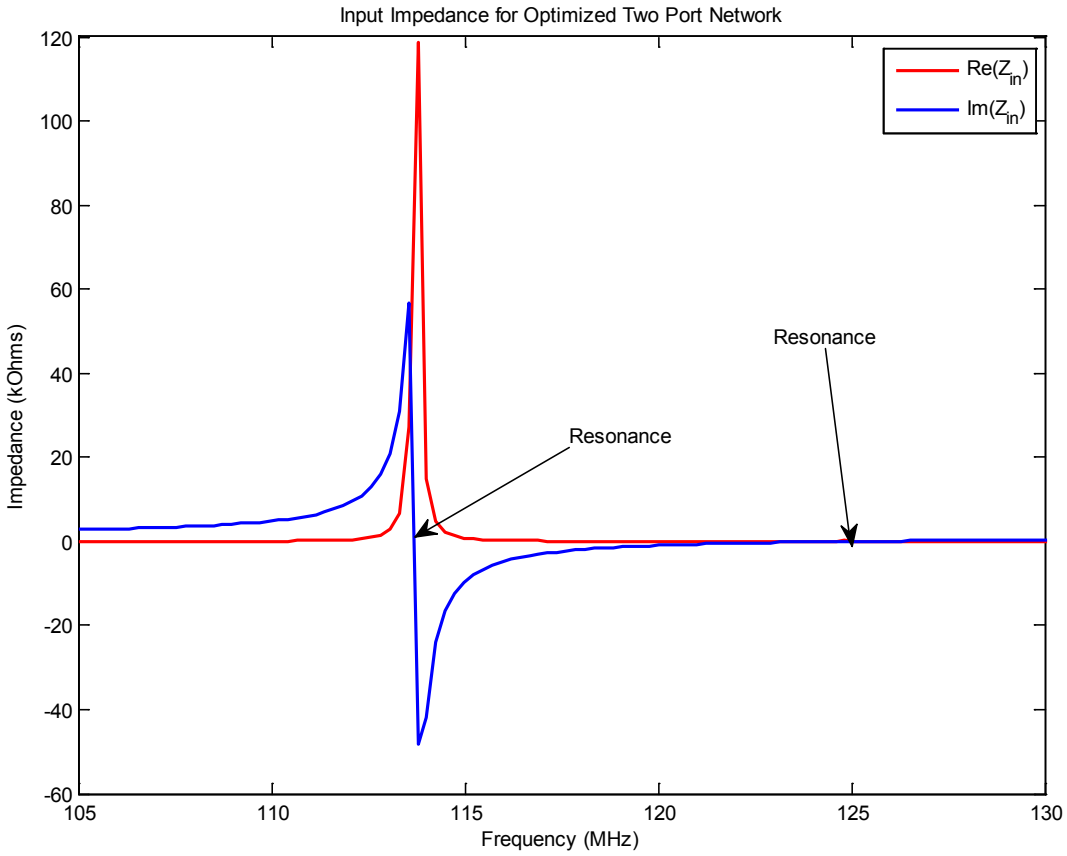


Figure 1-6 Input Impedance as Seen from Excitation Port under Resonance.

## 1.2 Related Research Background

There have been many groups and areas that have benefitted from research in the area of near field magnetic resonant coupling. The majority of work has been in the area of either electromagnetics, optics, or physics, with an emphasis in a variety of applications. Research from University of Innsbruck, Austria developed a geometric approach to understanding the coupling coefficient for an inductive RF-link (coils). The research conducted used two coils, as shown, with a lateral displacement, that would act as the mechanism for coupling degradation. Figure 1-7 displays the coupling coefficient results from lateral

displacing a secondary single turn coil at differing distances, *d*, between coils. These results display the correlation between axial directed mutual inductance, and the cost of moving the receiving coupler in azimuth. This same concept will be demonstrated in Chapter 3 of this paper.

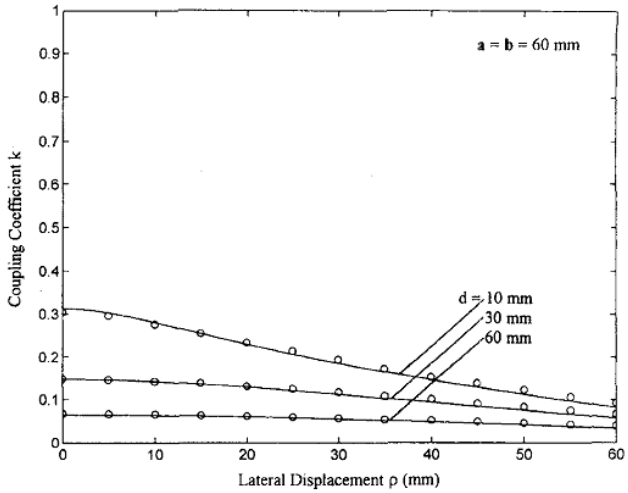


Figure 1-7 Degradation of the Coupling Efficiency with Variations in Lateral Displacement.

The gap from the use of inductive coupling for power transfer to resonant coupling came with the advent of self-powered RFID chips. Figure 1-8 displays a comparison between the frequency response for low and high Q coupling, as well as a reference for purely inductive coupling[10].

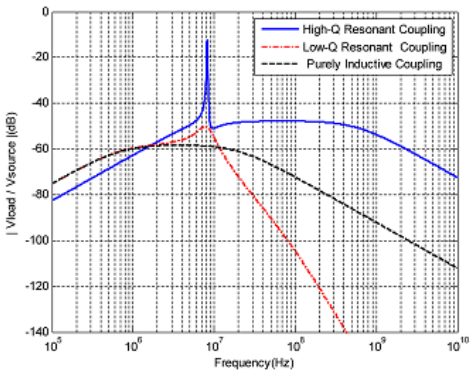


Figure 1-8 Comparison between Differing Coupling

In a recent investigation it was mentioned that a shunt capacitance on the receiving end of a secondary coil could amplify voltage from the when using a dual diode network to power scavenge for a RFID[11, 12]. This led to the development of resonance on both ends of the transfer process. A team of researchers from MIT experimented with the concept of using both networks in resonance at mid-range distances (*d* is a function of radii) [13, 14]. The theory that the team developed was fundamentally based off of the coupled-mode theory presented by Haus[15, 16]. Using this basis, the research expanded on the resonant modes of both a disk, and a capacitively loaded loop antenna. The capacitive nature of

the structure was implemented by using the two disks at opposing ends of the coil inductor (or loop in this case). The resulting structure looked as displayed in Figure 1-9.

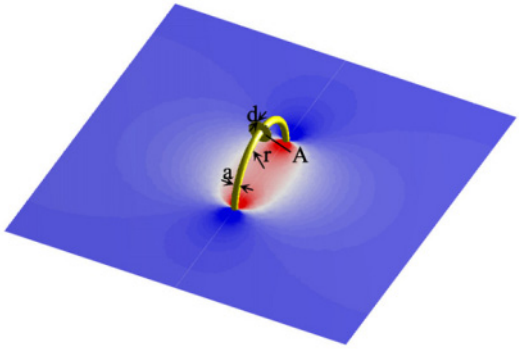


Figure 1-9 Magnetic field Variation from the Capacitively loaded Loop

The numerical calculation was validated with experimental results. The prototyping consisted of a driving circuit (loop) that was coupled to a driver coil, which then resonantly coupled to the same device at a given range. The results show a coupling efficiency of up to 40-50% for a two diameter coil distance. The results from this prototype are displayed in Figure 1-10.

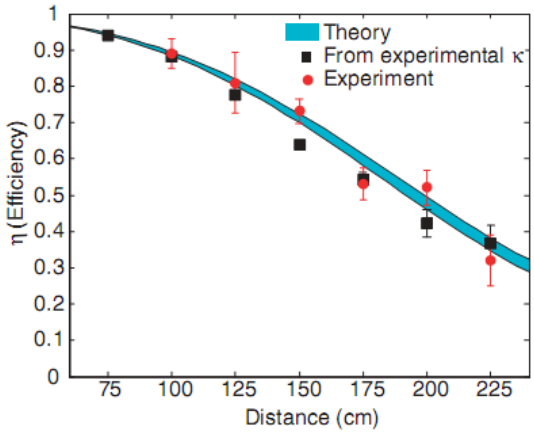


Figure 1-10 Resonant Coupling Efficiency with Differing Distances

Similar experiments have been improved upon for a variety of applications. Multiple receiver systems using magnetic resonance have been investigated using the aforementioned tuned coil approaches, and have shown results of power transfers with $S_{12}$ of -12.5dB[10]. This specific research provided background on the methodology behind finding links with multiple coils. This is particularly important within this investigation. Each separate coil that was tuned for resonance acts as a separate element in an array. In the case of Cannon, Hoburg, and Goldstein's work the flux linkages between the elements were pre-determined (the inductive coupling between them). After determining the mutual inductance between the coils, a matching network was added to the coils in order to cancel the reactive

portion of the impedance seen from the source. In this way all of the receivers would see only real power being delivered to the load. In this regard, this paper's investigation is similar, in that the transmitter will consist of multiple elements, acting as a single structure.

Other advances within the field of power transfer via resonant coupling have surfaced in the area of biomedical sensing devices. As is the case with most implantable electronic devices, the availability of the device is directly related to the lifespan of its power supply. A method for powering these devices seems to be a prudent concern for long term implants. The absence of spurious loss due to off resonant objects interfering with coupling allows for the passage of energy through biological tissues without the issue of cell destruction in the process (magnetic radiation tends to be less harmful than electric). In research from the University of British Columbia we see an approach to extending the life of biomedical implants by the use of resonant coils. An analysis to the coupling coefficient strength to the loss or Q of the network is presented in Figure 1-11[17]. The structural setup was similar to that of the mid-range coupling, that that a four coil system was utilized, with a driver, primary, secondary, and a load circuit. A correlation between the coupling efficiency and the network Q was derived as[18]

$$\eta = \frac{k^2 Q_p Q_s}{1 + k^2 Q_p Q_s}$$

This describes the characteristic of the coupling efficiency as the loss of either coil is increased. As with the coil driving circuits, it is important to note that all the power coupling efficiency is linearly related to the loss in the networks that are coupling. Further investigations with the four coil structure have shown an acute sensitivity in the resonant networks[19]. Figure 1-12 displays this sensitivity as a function of coil distance and operating frequency. Of course, as with all high Q resonant networks, the functional limitation to implementation usually lies in the sensitivity of the elements of the network. There is a general range in which most elements can be tuned until mutual resonance is broken, and the coupling becomes almost purely inductive. This, as with other characteristics that disturb coupling, will be analyzed later within the paper.

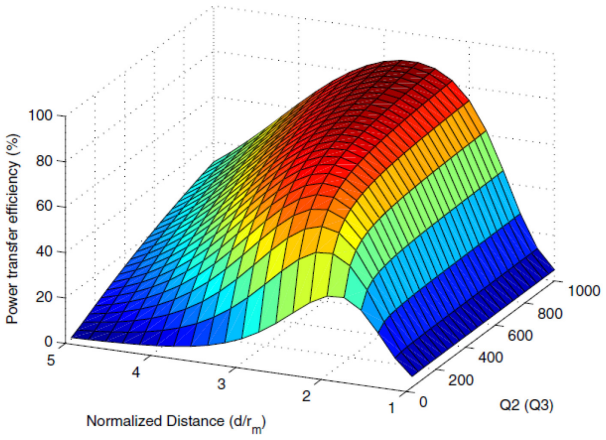


Figure 1-11 Coupling Efficiency with Respect to the Loss Found in Couplers

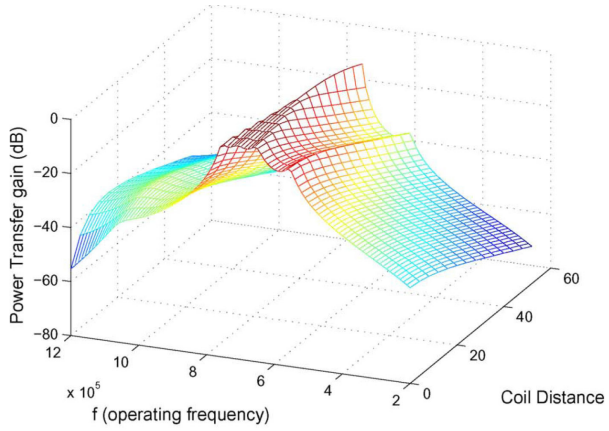


(a)

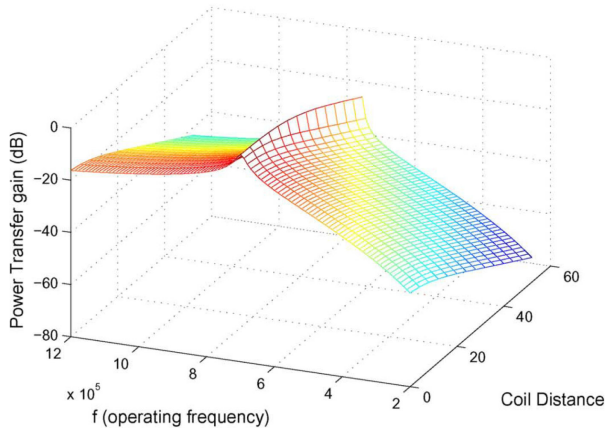


(b)

Figure 1-12 Coupling Efficiency with regard to Operating Frequency and Distance

## 1.3 Motivations for Research

As can be seen from current advances in wireless power, the majority of applications have utilized the helical coil to magnetically couple between networks. As is the case with inductive coupling, the helical coil provides a very strong reactive near field and is thus a promising choice as a magnetic coupler. However, in order to fully numerically investigate the coupling phenomena, it is prudent to use a coupling element that can be imaged, in order to see the effects of ground scattering. This leads to the fundamental basis of the research presented in this paper. By limiting the number of turns in the coil element, even down to one turn, and by tuning resonant networks between multiple single turn loops, it is possible to use an array to form multiple driving circuits in order to couple with another single turn receiver. In this way an optimization process between full wave 3D EM simulation and circuit simulation could be linked to quickly show the maximal coupling between two resonant networks. This process will embed the signature of electromagnetic interactions between elements under loose coupling and use circuit models to quickly and accurately match networks in order to achieve resonance.

A variety of applications arise from this optimization process. When an algorithm is known for the correlation between the lumped elements in a resonant circuit, and the coupling coefficient for a receiver anywhere in free space, a communication network between transmitter and receiver can be formed for power tracking. Multiple couplers with differing velocities can be receiving energy from a stationary source. By analyzing fields that arise during resonant coupling, an understanding of proper alignment of couplers can be ascertained. This clear understanding of geometric displacement and its effects on coupling strength can lead to the implementation of resonant networks that are less affected by off-resonant conductive objects.

# Chapter 2: Numerical Setup

## 2.1 Full Wave Method of Moments Simulation

The foundation for the simulation analysis of the coupling networks relies on the balance between optimization in a circuit simulation environment, and the interaction simulation in a 3D electromagnetic simulator. The methodology is somewhat recursive and self-validating in nature, as can be seen by the block diagram of the simulation setup in Figure 2-13.

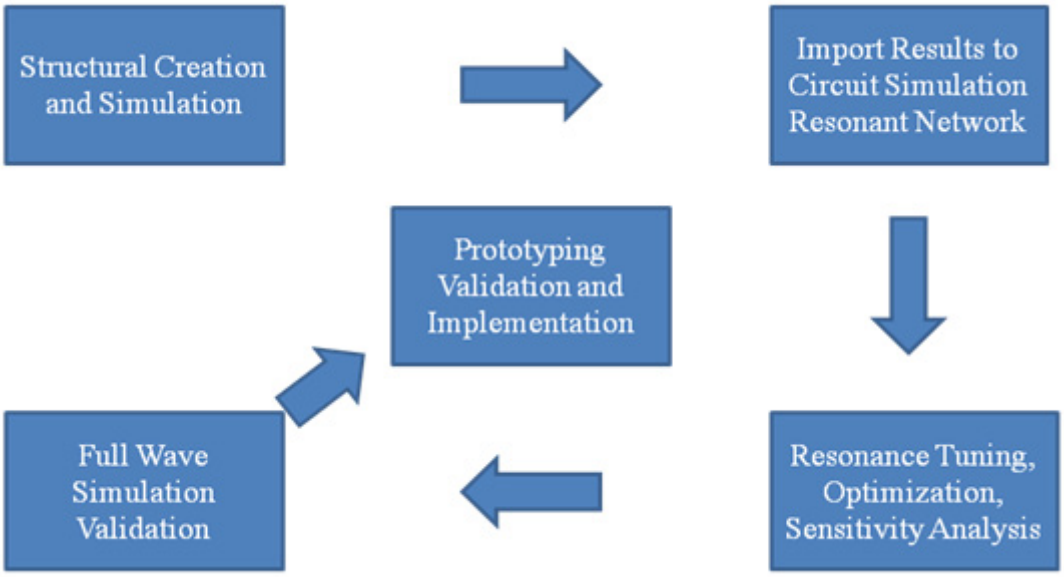


Figure 2-13 Methodology behind the Optimization and Validation Process

The primary tools for all simulation analysis were FEKO Suite V5.5® and Advanced Design System 2009®. FEKO is an electromagnetic simulation software that uses the Method of Moments approach to solving the integral equations present in surface radiation problems.

As with any numerical analysis, the resultant errors that are reported from the simulation can be minimized with *a priori* knowledge of the structure that you are simulating, the frequency of analysis, and the particular type of interactions that will be analyzed. Method of Moments is a type of mathematical model used to describe the electromagnetic interactions by utilizing a basis function with an impedance matrix to satisfy the Kirchoff network equation:

$$\sum_{n=1}^{N} Z_{mn} I_n = V_m \qquad m = 1, 2, 3, \ldots, N$$

Ultimately, we want to analyze the fields that are caused by exciting some structure. These fields can be mathematically modeled by Maxwell's equations. Let us use the example of a simple wire (dipole). The vector magnetic potential, $\bar{A}$, can be represented by the line integral:

$$\bar{A} = \frac{\mu}{4\pi} \oint I(z') \frac{e^{-jkr}}{r} dz'$$

for a z-directed wire. If we represent this equation in a simpler form where

$$\bar{A} = f_m$$

$$I(z') = I_n$$

$$\frac{e^{-jkr}}{r} = Z_{mn}$$

where m, n are the number of segments chosen along the wire. In order to solve for the currents we can see that we are going to need to use matrix inversion techniques:

$$[I_n] = [Z_{mn}]^{-1}[f_m]$$

The basis function $Z_{mn}$, in this particular case, plays an important role in determining whether the simple matrix operations can be used for inversion. In most small antenna cases (as is in this paper), the imaginary part of the impedance that is calculated is orders of magnitude larger than the real part. Take for instance the case of a 1$m$ dipole. At a frequency of 150MHz, the resonant frequency of the antenna, the input impedance for a centrally placed port is 300+500jΩ, while at a frequency of 1.5MHz ($l = \frac{\lambda}{200}$) the input impedance is .0095-31500jΩ. The real part of the impedance is so small compared to the when inverting the matrix, the impedance can't be delineated from numerical error. An important aspect to the Method of Moments simulation, in the case of a small antenna, is correct mesh sizing, and double precision accuracy. Double precision accuracy uses a predetermined floating point numerical system, that truncates at a larger number of decimal places, which allows for numbers to be distinguishable when much less than 1. Double precision significantly increases simulation time, but is required for accurate results with structures having length, $l \ll \lambda$.

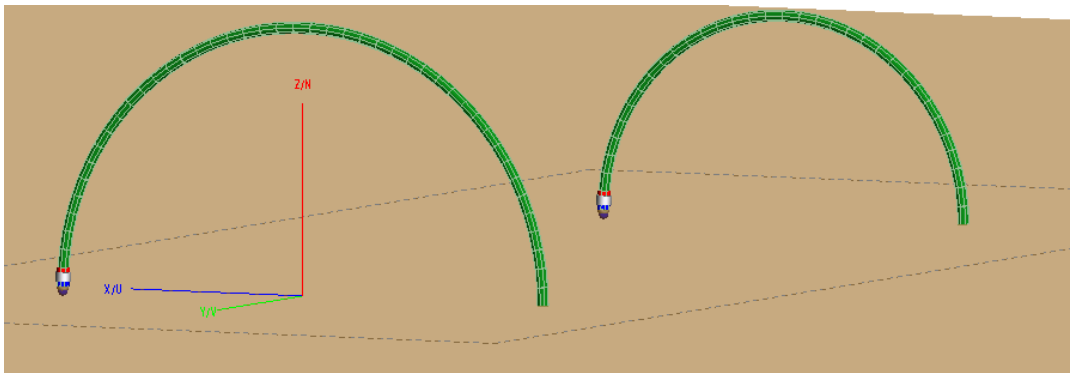

Figure 2-14 Properly Meshed Imaged Half Loops

This particular problem persists for the coupling structure that will be analyzed in this paper, given its small electrical length. Figure 2-14 shows the 3D structure as it will be analyzed after correct meshing is chosen. The smooth structure of the antenna is maintained, while double precision solution settings allow for accurate calculation of fields. It is important to choose a meshing length that does not sacrifice the geometric integrity of the structure, as this plays an important role in the magnetic field for a loop dipole (surface area changes). Figure 2-15 displays the same structure meshed at an inappropriate length for maintaining structural integrity.

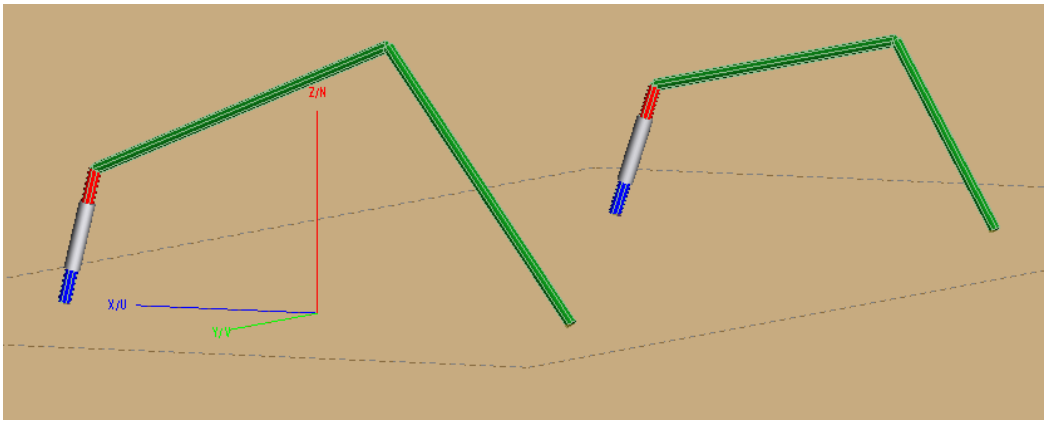

Figure 2-15 Improperly Meshed Imaged Half Loops

The main function of the full wave simulator during the optimization process is to provide an electromagnetic signature for the inductive coupling between two elements. In order to optimize for networks connected to the coupler, the circuit simulator needs to be able to calculate a proper impedance match with the through-loss between coupling elements. The full wave simulator provides an S-parameter matrix, which describes the reflections between the elements. This interaction matrix provides the circuit simulator with a suitable piece of data to analyze for a proper impedance match. The circuit simulator will be described in greater detail in the following Section 3.4.

## 2.2 Structural Geometry/Analysis

The structure of the coupling element will play an important role in determining the directionality of energy reception in free space. For HF and VHF frequencies (3-300MHz), in which this device operates, a variety of factors are present in the methodology behind choosing an appropriate structure. As described in Chapter 1, there have been many experiments with elements ranging from simple wire dipoles to rectangular loop helices. The coupler used in this particular structure is a imaged half loop, in order to nullify the effects of using a balun to feed the networks. The Green's function approach can be used to understand the specifics behind the directivity of the loop antenna. The structural geometry of the analysis will assume that the loop is axially z-directed, while the current will be in the phi (ϕ) direction.

A current can be defined in the spherical coordinate system from the cylindrical coordinate system as:

$$I = \tilde{\boldsymbol{a}}_{\boldsymbol{r}}\left[I_\rho sin\theta\, cos(\phi-\phi') + I_\phi sin\theta\, sin(\phi-\phi') + I_z\, cos\theta\right]$$

$$+\tilde{\boldsymbol{a}}_{\boldsymbol{\theta}}\left[I_\rho cos\theta\, cos(\phi-\phi') + I_\phi cos\theta sin(\phi-\phi') - I_z sin\theta\right]$$

$$+\tilde{\boldsymbol{a}}_{\boldsymbol{\phi}}[-I_\rho sin(\phi-\phi') + I_\phi cos(\phi-\phi')]$$

As known from the geometry in the loop, current will propagate in the ϕ direction only. The current can be reduced to *:*

$$I = \tilde{\boldsymbol{a}}_{\boldsymbol{r}} I_\phi sin\theta sin(\phi-\phi') + \tilde{\boldsymbol{a}}_{\boldsymbol{\theta}} I_\phi cos\theta sin(\phi-\phi') + \tilde{\boldsymbol{a}}_{\boldsymbol{\phi}} I_\phi cos(\phi-\phi')$$

This current allows for the calculation of the vector magnetic potential, $\bar{A}$, as shown in Eq. 3.2. This potential, expanded for any *r* around the source loop has the form:

$$\bar{\boldsymbol{A}}_\phi = \frac{a\mu}{4\pi}\oint I_\phi cos(\phi-\phi')\frac{e^{-jk\sqrt{r^2+a^2-2arsin\theta cos\phi-\phi'}}}{\sqrt{r^2+a^2-2arsin\theta cos\phi-\phi'}}d\phi'$$

For the ϕ directed vector magnetic potential, and

$$\bar{\boldsymbol{A}}_r = \frac{a\mu}{4\pi}\oint I_\phi sin\theta sin(\phi-\phi')\frac{e^{-jk\sqrt{r^2+a^2-2arsin\theta cos\phi-\phi'}}}{\sqrt{r^2+a^2-2arsin\theta cos\phi-\phi'}}d\phi'$$

$$\bar{\boldsymbol{A}}_\theta = \frac{a\mu}{4\pi}\oint I_\phi cos\theta sin(\phi-\phi')\frac{e^{-jk\sqrt{r^2+a^2-2arsin\theta cos\phi-\phi'}}}{\sqrt{r^2+a^2-2arsin\theta cos\phi-\phi'}}d\phi'$$

For the r and θ directed fields. From Maxwell's equations the magnetic field, $\bar{\boldsymbol{H}}$, can be calculated by

$$\bar{\boldsymbol{H}} = \frac{1}{\mu}\nabla \times \bar{\boldsymbol{A}}$$

In the spherical coordinate system the magnetic field for the r and θ directions are

$$\bar{\boldsymbol{H}}_r = \frac{acos(\phi-\phi')^2 cos\theta}{r^2+a^2-2arsin\theta cos\phi-\phi'} f + \frac{asin(\phi-\phi')^2 cos\theta}{r^2+a^2-2arsin\theta cos\phi-\phi'} f + \frac{jakcos(\phi-\phi')^2 cos\theta}{\sqrt{r^2+a^2-2arsin\theta cos\phi-\phi'}} f + \frac{jaksin(\phi-\phi')^2 cos\theta}{\sqrt{r^2+a^2-2arsin\theta cos\phi-\phi'}} f$$

$$\bar{\boldsymbol{H}}_\theta = \frac{cos\,(\phi-\phi')(2r-2a\,cos(\phi-\phi')\,sin\theta)}{2(r^2+a^2-2arsin\theta cos\phi-\phi')} f + \frac{jkcos\,(\phi-\phi')(2r-2a\,cos(\phi-\phi')\,sin\theta)}{2(r^2+a^2-2arsin\theta cos\phi-\phi')} f - \frac{jaksin(\phi-\phi')^2\,sin\,\theta}{\sqrt{r^2+a^2-2arsin\theta cos\phi-\phi'}} f - \frac{asin(\phi-\phi')^2 sin\theta}{r^2+a^2-2arsin\theta cos\phi-\phi'} f$$

where

$$f = \frac{e^{-jk\sqrt{r^2+a^2-2arsin\theta cos\phi-\phi'}}}{\sqrt{r^2+a^2-2arsin\theta cos\phi-\phi'}}$$

which is commonly called the "Green's function". When we plot the pattern we can clearly see a null on the plane in which the coupler lies (Figure 2-16). This is beneficial for axial directed coupling, as the magnetic field is not attenuated in the direction of coupling.

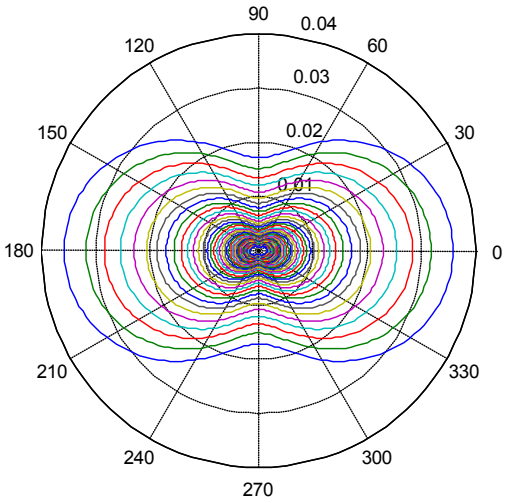


Figure 2-16 Magnetic Field at Differing Distances for a Loop Dipole at Broadside

The circular loop has a distinctly larger reactive near magnetic field as compared to the typical linear dipole. The loop has inductive properties which act as a storage device for magnetic field, which can be seen at distances ($d<.62\sqrt{\frac{D^3}{\lambda}}$) in the vicinity of the radiating device [Balanis]. Figure 2-17 shows the fields as from loop dipole as compared to a linear dipole using a FEKO full wave simulation.

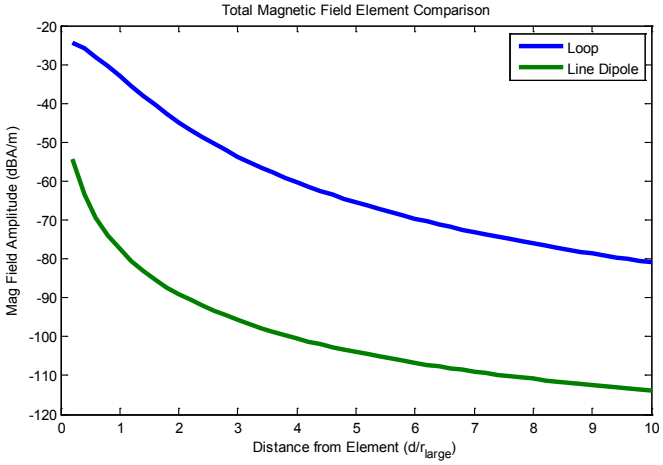


Figure 2-17 Element Comparison for Magnetic Field Strength

Typically a multiple turn loop element, called a helix, can be used in order to store greater amounts of magnetic energy. This is described from previous research, as most of inductive coupling is based around the helix. The amount of inductance within the structure is proportional to the amount of turns that structure has. Of course, the number of turns of a coil is also directly proportional to the physical length of the structure. This proportionality leads to issues for inductor creation in the RF regime. The

real loss from conductor dissipation dominates the reactance given the greater amount of wire that is needed to achieve a certain inductance. Also, unless the wire is shielded, the inductor begins to act as a capacitor at certain frequencies due to the gap capacitance between adjacent loops. These issues will be addressed mathematically and practically in the description of prototyping setup. It is due to these limitations that a helical structure will not be directly used during this experiment. The phased array's structural properties, however, lend themselves to be compared to a helix (several single turn loops as opposed to one multi-turn helix).

## 2.3 Structural Variations

The distance, *r*, between coupling elements will be measured from the center of the transmitting loop. If the receiver is at a different point in azimuth, it will be moved concentrically with respect to the origin (transmitter center), thus resulting in no *r* variation. This principal also applies to structures with multiple transmitting elements. In the case of multiple elements, the distance, *r*, is calculated from the closest transmitter (the shortest distance between coupling elements). There are three distinct structural variations. The first will be the single feed network. The single feed network will consist of two half-loops axially directed from each other. Consequently there will only be two resonant networks for this specific structure. A picture of this setup can be found in Figure 2-19. This structure will act as the control group as variations for phased arrays are tested against it.

The other two structural arrangements are variations of phased arrays. The most widely used type of phased array is the coplanar array. The coplanar array consists of multiple elements adjacent to each other on the same plane. This is not fully realizable for the imaged half-loop case. The array cannot have any z varied coupling elements, as they would be lifted from the infinite ground plane which would violate the consistency in which the elements were fed. The lesser used structural variation, with respect to loop antennas, is the Yagi reflector antenna. These structures will consist of either the elements being concentrically designed, which results in a bulls eye shape, or axially directed, acting as a semi-helical shape. As with the Yagi-Uda antenna concept, the use of the back end elements will be that of directivity enhancement and direction finding. This axially-directed structure will have three forms, that vary in accordance to the radial size of each loop in the array, and the fashion it is arranged in the array. The "back staggered" array will consist of the two smaller radii couplers placed in front (referenced to the receiver) of the largest. The "front staggered" array is the mirror image of the back staggered array. For simplicity's sake, the array with all elements of the same radius will be called the "axially directed array". Figure 2-18 illustrates all structures.

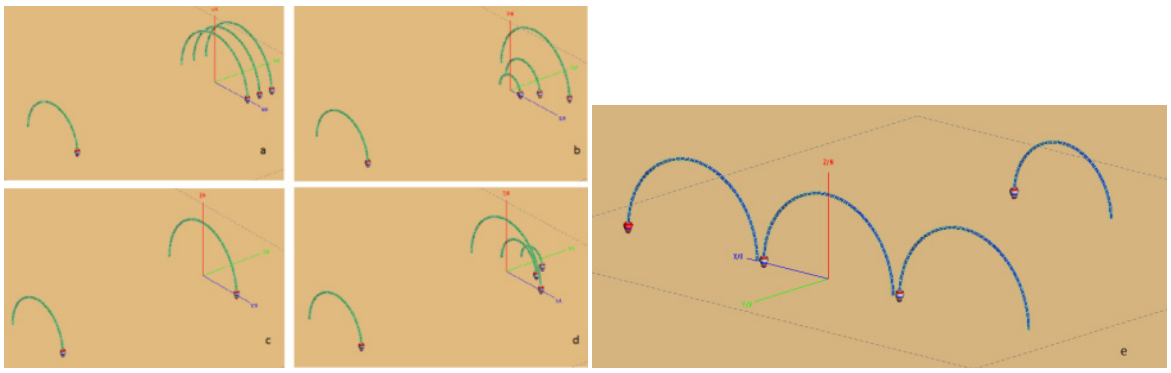

Figure 2-18 Structural Variations Under Consideration:
a. Axially Directed Array
b. Front Staggered Array
c. Single Feed
d. Back Staggered Array
c. Coplanar Array

## 2.4 Resonant Networks

In order to achieve a separation between pure inductive coupling and resonant coupling a resonant network can be connected in series with the coupling element. This resonant network adds reactance to the coupler, and acts as a storage device for both electric and magnetic energy. The majority of optimization will be based on the tuning and modeling of these networks.

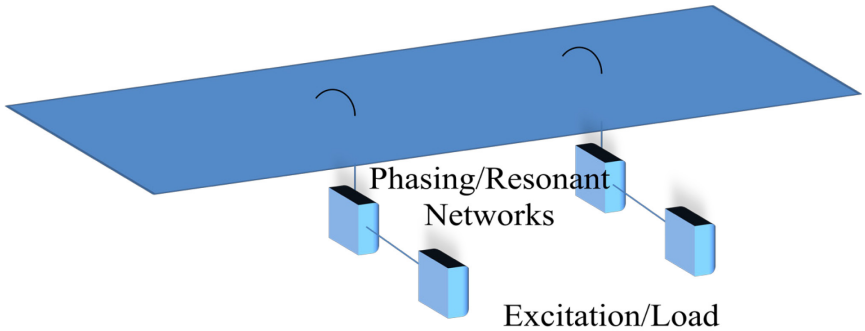


Figure 2-19 Network, Load, and Excitation Connections and Setup

It is important to define the feeding methodology of this network. The ports for each coupler were placed with a polarity feeding the antenna and the opposing polarity grounded. As can be seen from Figure 2-19, the excitation is connected to the phasing/resonant network, which will then be fed to the

coupler through the ground plane. This, in a practical sense, allows the networks to be shielded from the coupler, so as to directly measure the coupling between the half-loop elements. In the simulation, however, this is an unnecessary assumption. The two networks (half-loop coupler and phased network) are separated from one another by the use of an S-parameter file.

The resonant circuits that will be analyzed can be modeled by a simple RLC tank circuit. In order to get a greater understanding of the differing properties of the network, and how each contributes to coupling, we can describe the networks by the circuit illustration in Figure 2-20 (top). This illustration includes the full model for an inductor and capacitor, including gap capacitance and resistive properties (important at RF).

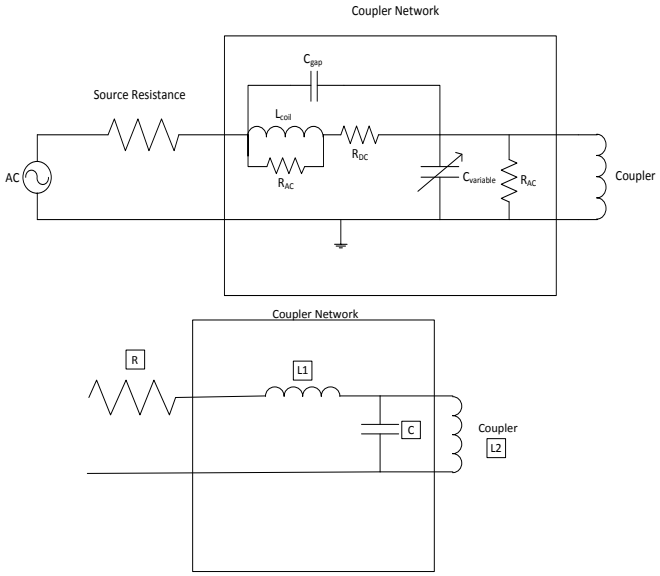


Figure 2-20 Expanded and Simplified versions of the RLC Resonant Networks

For simplicity's sake, the following analysis will be for an RLC tank circuit, with the coupling inductance, and the network inductance and capacitance. For the network described by Figure 2-20 (bottom), we can calculate the transfer function as:

$$H(s) = \frac{L_2 s}{CL_1L_2s^3 + CL_2Rs^2 + (L_2 + L_1)s + R}$$

From a quick examination of this transfer function we can quickly see that an increasing real impedance will lead to an attenuation of signal over the coupling element ($L_2$). This attenuation will lead to a proportional drop in the network Q, described by:

$$Q = \frac{f_c}{B_{3dB}}$$

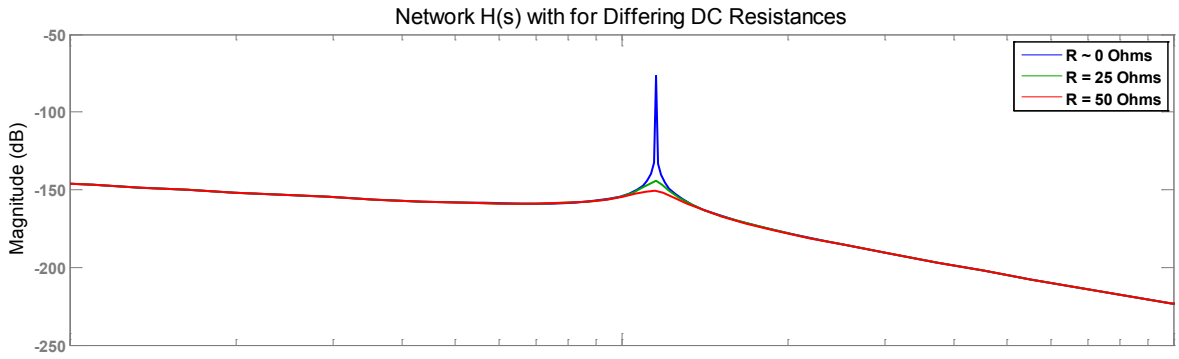


Figure 2-21 Effect of loss on the Output of a RLC Network at Resonance

This drop in Q will lead to a wider band network, at the expense of attenuation at resonance. This particular application of coupling requires an extremely narrow band, which suggests a small real impedance at the input of the networks. By observing Figure 2-21 it is clear that as the source resistance increases, and is not matched at the load, the Q will drop significantly. This shows the clear separation between pure inductive coupling ($R \rightarrow \infty$) and resonant coupling ($R \rightarrow 0$). For implementation, all elements will be designed around this particular low-loss goal, as to not add attenuation to the coupling (except for shunt elements). Practically, however, this real impedance will be intrinsic to each element, as well as dispersive. Thus when simulating and optimizing these networks, the $R$ value that is seen in these models will be kept at a constant value. Instead, another way to shift the response of the network is to change its reactance. The engineering methods for doing so will be described with prototyping, but for simulation and optimization only the variable reactive elements (not including the coupling half-loop) will be tuned to achieve resonant coupling. For a lossless network, shifting the reactance of the elements will shift the resonant frequency of the circuit. Figure 2-22 illustrates the resonant shift for a lossless network while tuning a capacitor between the *pF* and *nF* ranges. Notice that the total transfer peak is asymptotic to 0dB as the capacitance is increased.

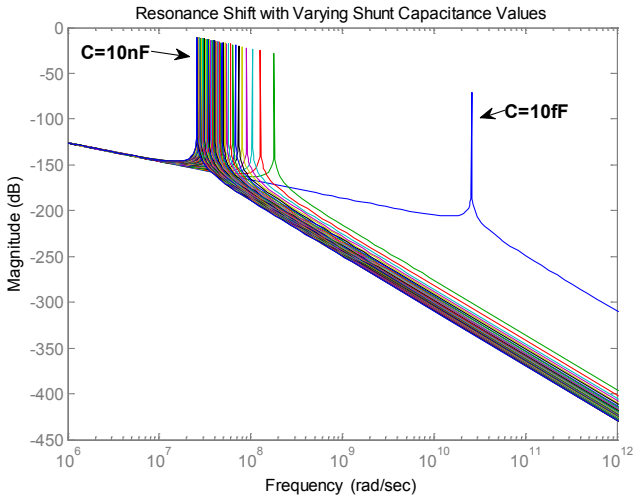

Figure 2-22 Resonant Shift for Varying Capacitances

## 2.5 Circuit Simulation (Advanced Design System®)

Advanced Design System® is a multi-use RF circuit analysis tool. Its primary use in this design process is as an optimization toolkit. As described before in Section 3.1, the 3D EM Simulator allows the user to extract the interactions between elements by way of an S-parameter matrix. This matrix gives insight to the return loss due to an amalgamation of reflections that we see from the coupling elements, ground reflections, and ohmic dissipation. With this information, the matching input impedance can be calculated in order to give the maximum power transfer at a given frequency.

The network will be simulated from lossless lumped element models. Figure 2-23 shows the full network schematic for a 4 port network (this is from the phased array). The ports have a 50Ω impedance, as well as the input impedance to the S-parameter block. The S-parameter block is an unmodified imported matrix from the 3D MoM Simulator, which is used to hold the EM signature of the couplers ($L_2$) in Figure 2-23. The matrix block is grounded with the same reference as the networks, which represents the semi-infinite ground plane that will be placed under the coupler during design construction. This is important as it shows that the inductive coupling between the half-loops (matrix block) are part of a total network, illustrated in Figure 2-23.

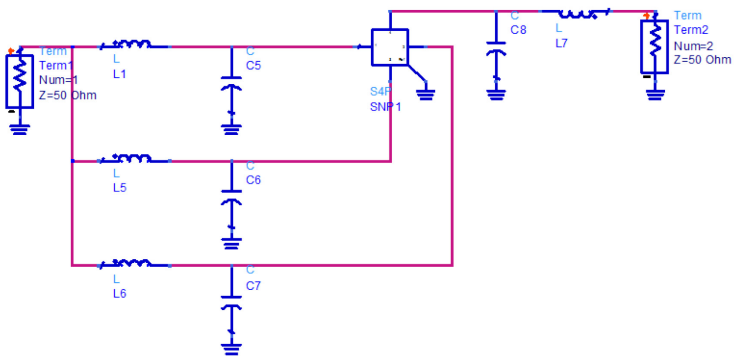


Figure 2-23 Full 3 Element Array Model ADS Schematic

Each reactive component to the network was given a practical constraint to limit the optimization time and to give reasonable reactance values for prototyping. There are a variety of optimization techniques that are available for this particular software. The general goal for the optimizer is acquiring an impedance match for the S-parameter matrix. The solution to this goal can be most efficiently isolated by using a gradient descent. The issue, however, with the gradient descent method is a "zig-zag" fashion in which it acquires a final solution to a contour's steepest descent. In this case it might be a better idea to isolate a solution, and then use a different technique to optimize in order to nullify the processing bottleneck.

A particular area of interest for the optimization is the frequency at which the maximum coupling occurs between terminal 1 and terminal 2 in Figure 2-23. This frequency is intrinsic to the resonant network, described in Section 3.3 for the lossless case. However, when the inductive coupling between the half-loops is integrated via S-parameter matrix, spurious losses have been added to the model of the resonant network, as well as an impedance that is dispersive which varies with differing half-loop structures (such as a phased array). This dispersive impedance causes a shift in the optimal frequency that should be used for optimization. Due to this variability, the process of optimization was repeated for a range of frequencies, which pinpoints an optimal frequency for the structure to couple. Once the solution for a single frequency was achieved, this result was compared to the optimization solutions to frequencies in a certain range. From the maximum coupling solutions a single frequency was determined for the most efficient coupling. An example of this output is displayed in Figure 2-24. For each structure this process must be repeated in order to secure optimal results.

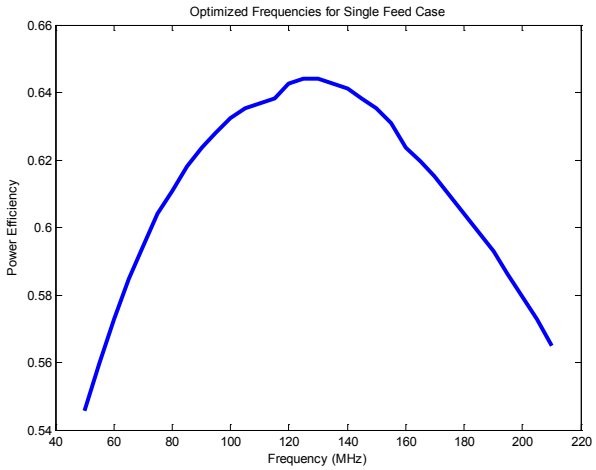


Figure 2-24 Example of Optimal Frequencies for the Single Feed Case

Once optimized, the achieved coupling will be sent to the 3D full wave simulation for validation. Statistical variant analysis can also be performed on this data to see how tuning can affect the network. Monte Carlo yield analysis will be the primary tool for displaying this. Controlling the variance of elements gives insight to the sensitivity of the network, and the limitations that are imposed during designing and prototyping.

## 2.6 Field Validation in 3D EM Simulator

ADS, as with FEKO, has the ability to export the S-parameter matrix of an entire network. This data will be imported back into the 3D simulation and connected, in series, to the coupling elements that were originally simulated as "general networks". A screenshot of the connection process can be seen in Figure 2-25. There are two reasons for this final simulation step. The first is to get a clear validation of the connection between circuit simulation (based primarily on Ohm's Laws), and EM simulation (based around Maxwell's equations). The second is to achieve a clearer understanding of the field interaction between the couplers at resonance. The Poynting Vector can be visualized on the axial plane's cut, and the directive power flow can be observed between the coupling elements. These field values can also be exported to any analytical toolkit in order to analysis on a field component level.

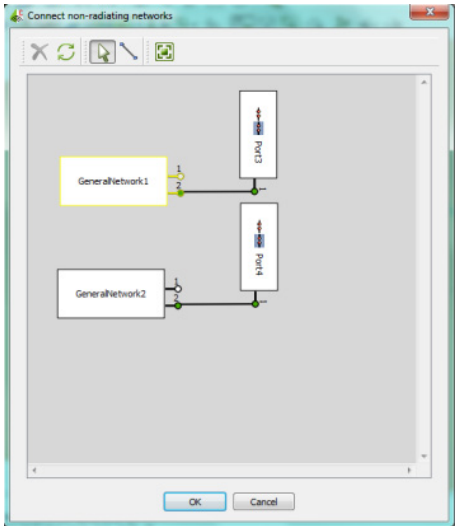

Figure 2-25 FEKO “General Network”

# Chapter 3: Numerical Results

As the basis for the numerical experimentation has been discussed, this chapter will provide all numerical results arising from any simulation analysis, including 3D full wave simulation, circuit optimization, and field analysis.

## 3.1 Inductive Coupling

### 3.1.1 Single Feed

The single feed network was simulated with θ=0 at varying frequencies. All couplers are considered to be in the electrically small regime (around $\frac{\lambda}{150}$) resulting in purely inductive coupling; no resonant networks were connected to the coupling elements. These elements were simulated between 10-250MHz with radii for the receiver and transmitter as 50mm and 37.5mm respectively. All couplers are simulated with the copper as the conductive medium. Table 3-1 shows the metallic medium properties for copper. Figure 3-27 displays the inductive coupling for differing receiver distances, normalized to the largest radius loop.

Table 3-1: Propeties of Copper

| Name | Conductivity σ | Relative Permeability $\mu_r$ | Magnetic Loss Factor δ |
|---|---|---|---|
| Copper | 16.68e6 | 1.0 | 0 |

As can be expected in practice, the receiver will move with reference to a specified transmitter location. This will cause a degradation to the ***H*** field and subsequently a degradation to the efficiency of the coupling that can be achieved between the couplers. During all simulation setups, when the receiver moves in azimuth, the distance, *r*, will be constant. Figure 3-28 shows the case of $r = 4r_{largeloop}$. This degradation is shaped by the pattern for the element that is coupling. It can be observed that the inductive coupling for a coplanar receiver ($\theta=90^o$) increases proportionally with frequency, a characteristic that isn't shared from off-plane angles. In this case it would be prudent to analyze higher frequency coupling at these angular variations (co-planar with very small grazing incidences).

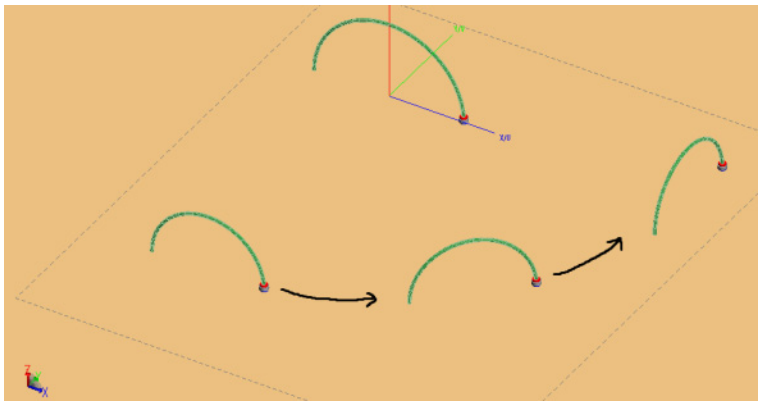

Figure 3-26 Azimuthal Variation for the Single Feed Case

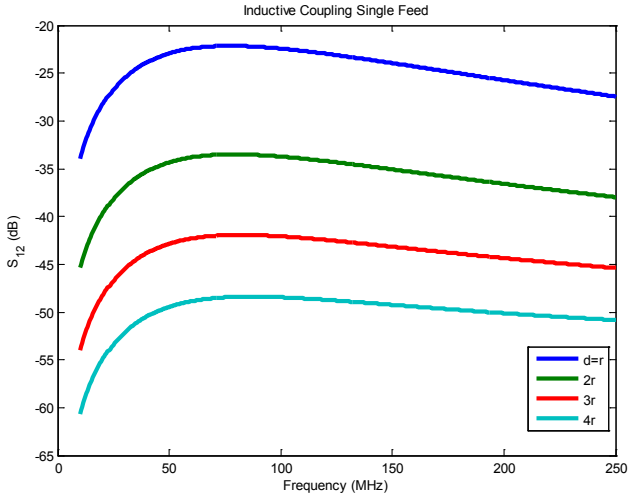


Figure 3-27 Inductive Coupling $S_{12}$ for Differing Coupler Seperation Distances

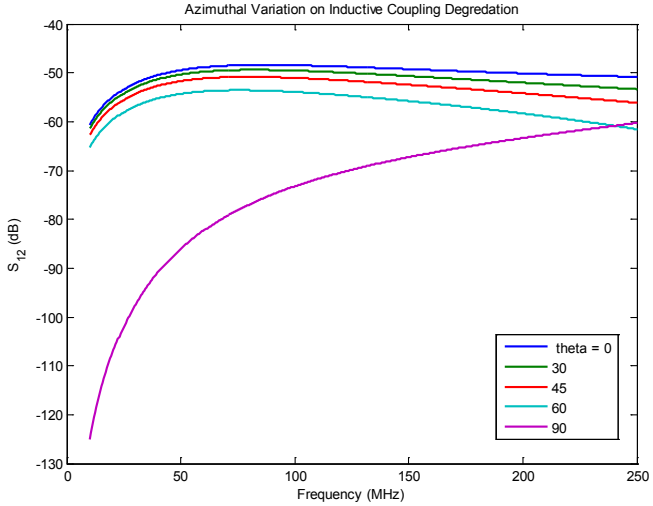


Figure 3-28 Inductive Coupling Degradation with Varying Azimuthal Displacement Angles

### 3.1.2 Array Feed

The four structural variations that were expressed in Chapter 3 were also simulated with the same controlled constraints as the single feed network for comparative purposes. Table3-2 gives the physical structural geometry of all variations. For both of the staggered cases, it should be emphasized that the distance, *r*, is normalized to the *closest* transmitting coupler of the array, and not the largest. Figure 3-30 gives a total comparison of axially directed inductive coupling between the different structural setups as compared to the control structure (single feed).

Table 3-2: Spacing and Geometry Variations

| Structure | Element Separation (mm) | $r_{close}$ (mm) | $r_{mid}$ (mm) | $r_{far}$ (mm) |
|---|---|---|---|---|
| Axially Directed Array | 15 | 50 | 50 | 50 |
| Back Staggered | 15 | 15 | 25 | 50 |
| Front Staggered | 15 | 50 | 25 | 15 |
| Coplanar | 5 | 50 | 50 | 50 |
| Single Feed | N/A | 50 | N/A | N/A |
| Receiving Element | N/A | 37.5 | N/A | N/A |

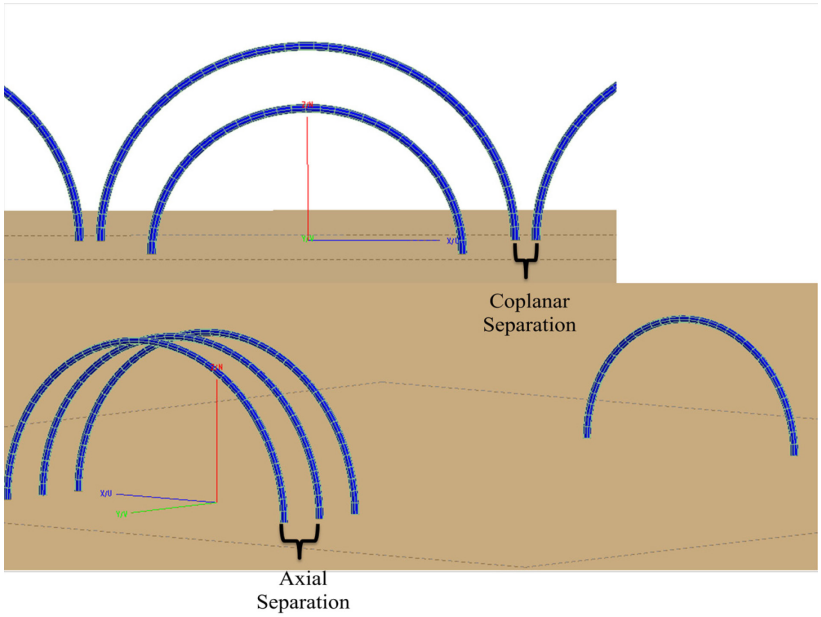


Figure 3-29 Elemental Seperation

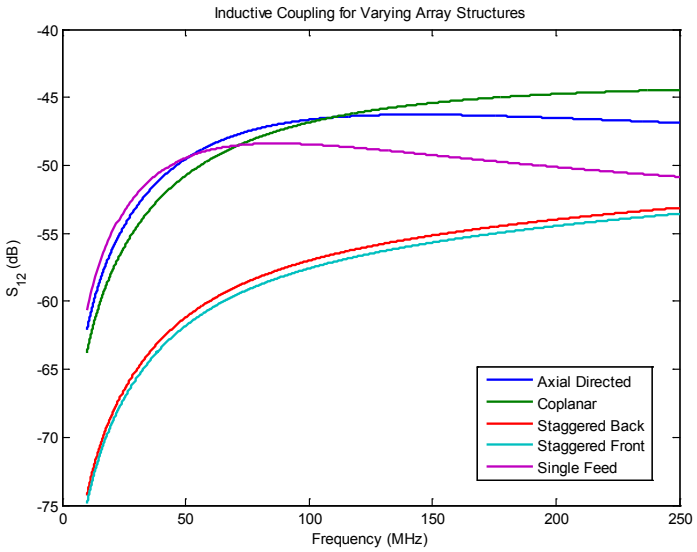


Figure 3-30 Inductive Coupling for Varying Array Structures

Element spacing and sizing was due to a number of factors. The main issue with coupling an array is the parasitic inductance that is received in between elements. The ratio to the distance an element is spaced from an adjacent element to the distance from the receiver is around 13, for the staggered cases. This parasitic power dissipation will occur most dramatically at the frequencies in which both of these elements are at resonance. If all elements are of different sizes (the staggered array cases) then it will be easier to decouple them with each other, while coupling with the receiver. As can be seen from the inductive properties of these arrays, the staggered arrays have significant power dissipation due to induction within the array. The parasitic effects of these arrays precipitate into resonant coupling.

### 3.1.3 Ground Plane

In designing around the implementation objective, it was prudent to cut the ground plane to a semi-infinite metallic sheet. This was accomplished in FEKO by using a metallic conductor (in this case brass at 28% copper conductivity) with dimensions 2ft x 4ft (.61m x 1.22m). This plane was connected in the same manner than the infinite PEC was connected to the coupling elements. The metallic ground plane, however, does not have the same simulation properties as the infinite ground plane, and is treated as a simulation geometry. The finite ground plane requires a mesh in order to be simulated. This mesh was formed more accurately by developing a finer mesh around the outer edges of the coupling elements, in order to accurately simulate any ground coupling that occurs. A cut was taken from the ground plan around the coupling elements in order to implement this meshing. Figure 3-31 illustrates this final mesh grid that was implemented for the infinite ground plane. The inductive coupling as compared to the infinite ground plane can be seen in Figure 3-32.

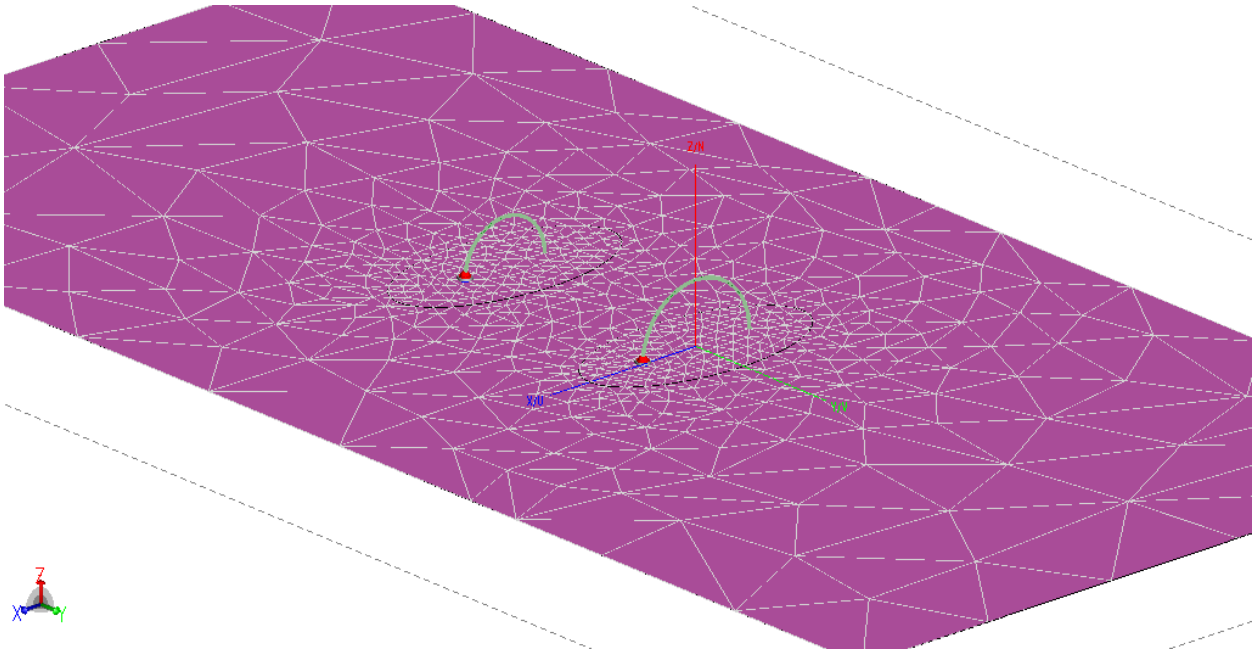

Figure 3-31 Meshing for the Finite Ground Plane, Single Feed Case

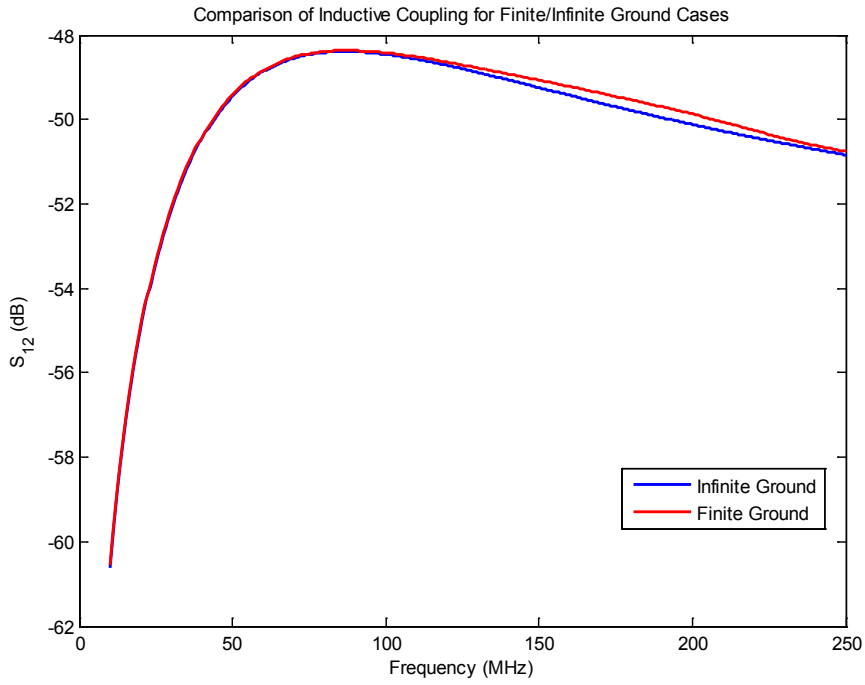


Figure 3-32 Comparison of Inductive Coupling for Finite/Infinite Ground Cases

## 3.2 Resonant Coupling Optimization ADS®

### 3.2.1 Lossless Element, Infinite Ground Plane Case

In order to achieve an acceptable and implementable solution to the resonant coupled case, there needs to be reasonable constraints placed on the elements within the network. Without these constraints, the optimizer could lock into a gradient dissent in which the solution would be implausible for prototyping. In this particular case let the amount of wire used for a coil inductor be:

$$l = \pi dN$$

As with the coupling elements themselves, the design of the coil needs to be away from its natural resonance in the microwave regime. This is discussed in detail in Chapter 4. Wavelengths range from 1.2m to 30m in the range under test (10-250MHz). Coils designed with these parameters have been tested and vary from nH to μH. It is under these conditions that the restraint for the inductors in the network has been set at 6000nH or 6μH. Inductive reactances greater than the constraint, in the microwave spectrum, require coil lengths to exceed that of the wavelength of the circuit. The resonant singularity that occurs causes the coil to act as a capacitor as frequency increases. Table 3-3 displays the constraints put on all elements in the resonant networks.

Table 3-3: Element Values

| Element | Minimum Value | Maximum Value |
|---|---|---|
| Inductor | 0H | 6000nH |
| Capacitor | 1fF | 1μF |
| Terminal Resistance | 50 Ohm | 50 Ohm |

When all networks are properly connected to the "data item" which holds the s-parameter matrix for the a schema for optimization must be followed for an entire frequency range. The methodology behind the optimization was to use a single frequency constraint and not optimize over a range. This method will provide the highest Q solution. The optimization was completed for the lower or upper bound on the *f* range, and each subsequent optimization step would be performed for a lower or higher using the values from the previous optimization as nominal values. For all structures this frequency step was 5MHz. This resolution gave an accurate measure to the range in which coupling reached a maximum. Figure 3-33

shows the results for this process for the single feed control structure. Figure 3-34 compares these results to all structures.

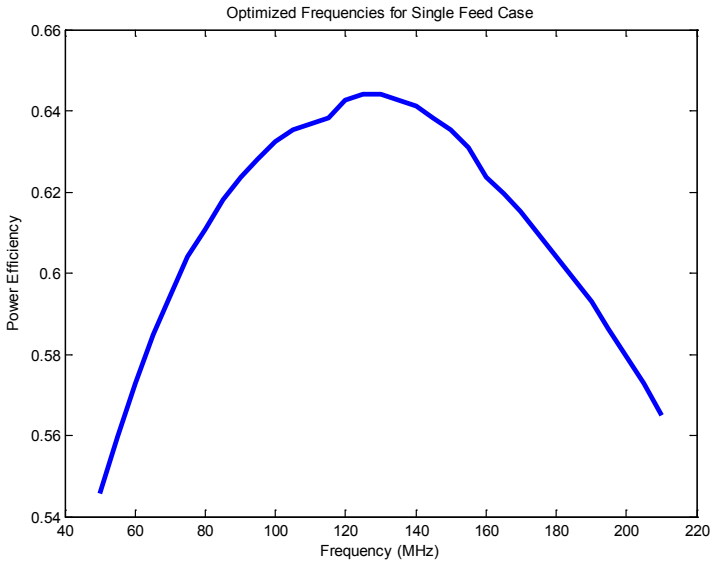


Figure 3-33 Optimal Frequency for Single Feed Case

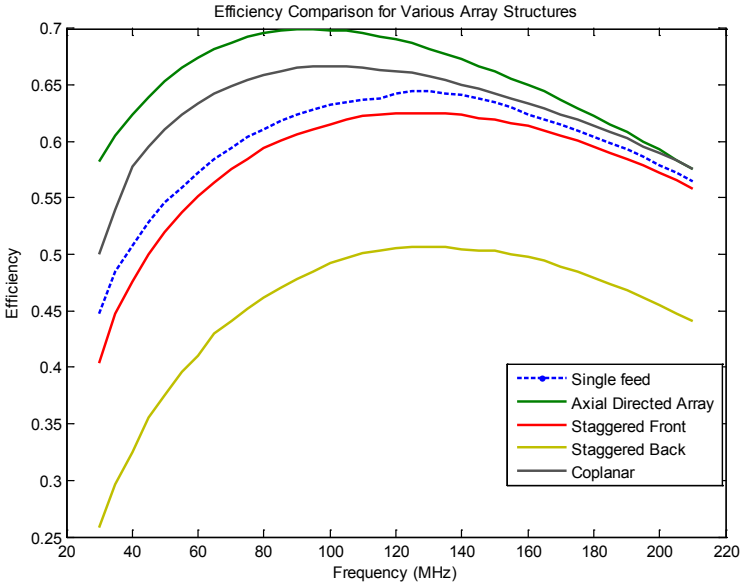


Figure 3-34 Coupling Efficiency Optimal Frequency Analysis for Varying Array Structures

In order to see the frequency response the optimal frequency was chosen for each of the structures. As can be seen for each structure there appears to be a range of optimal frequencies. In this case the smallest of the range was chosen to reduce skin/RF losses. From Figure 3-34, it is illustrated that the

staggered arrays would dissipate more power than the other arrangements. This is validated by the maximum optimized coupling curves, where the staggered arrays clearly have a larger margin of loss than any other structural variation. It can be observed in Figure 3-35 that the two staggered designs incorporate structures whose resonances do not coincide. The *f* domain data displays the multiple resonances for the staggered structures.

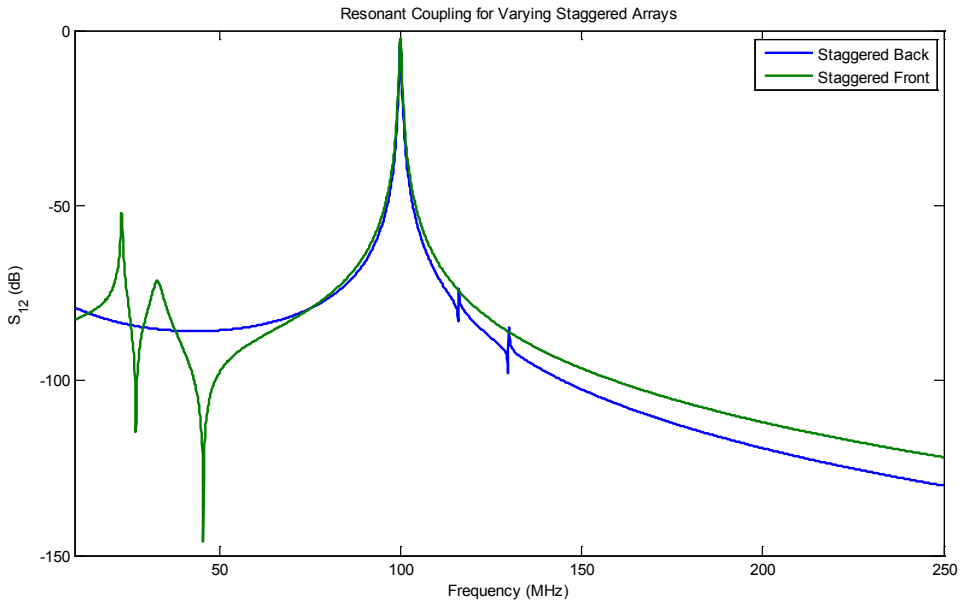


Figure 3-35 Staggered Array Comparison for Under Resonant Coupling

This disassociation of resonances could be due to an incorrect solution that was optimized, however all optimizer conditions were kept constant throughout this particular comparison, and so changing said condition was not part of this data collection. This process, for the staggered array case, was repeated for a differing set of optimizer goals. The optimizer was given three separate $S_{14}$, $S_{24}$, and $S_{34}$ maximization goals to find a balance between the individual resonances. Figure 3-36 gives an illustration of how this technique changes the optimized solution. By using the multi-goal approach it can be seen that the optimizer focuses two of the elements to the same resonance, while being unable to optimize the third pole to coincide. This is possibly due in part to the narrow constraint placed on the element values that inhibits the third pole to be shifted correctly.

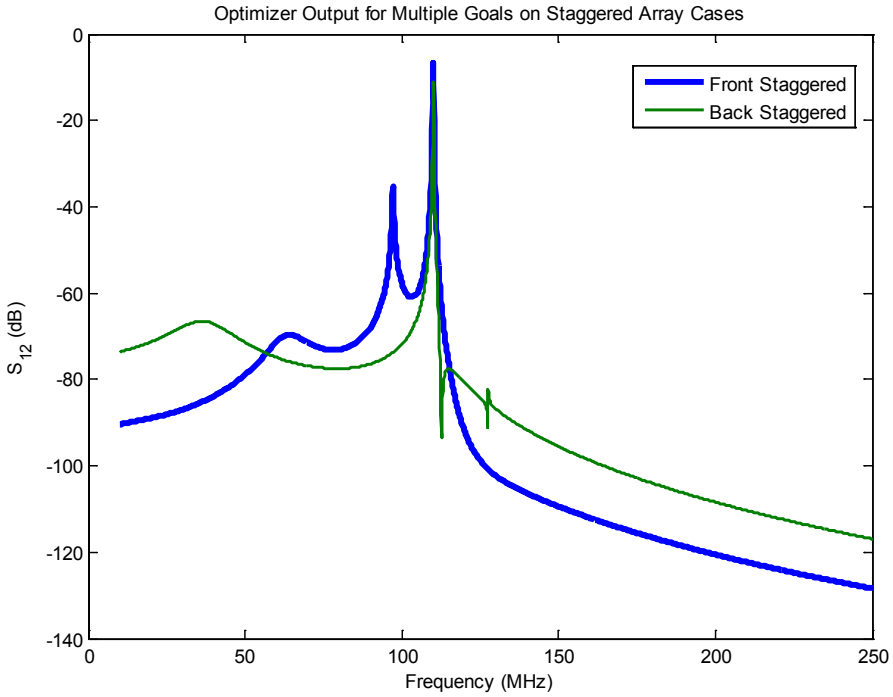


Figure 3-36 Optimized Networks for Resonance when using Multiple Goals for Optimization

Table 3-4: Maximum Coupling for Staggered Structures

| Array | Maximum Coupling with Multiple Optimization Goals |
|---|---|
| Front Staggered | -6.51 dB / .223 efficiency |
| Back Staggered | -11.42 dB / .0721 efficiency |

As was shown with the inductive coupling, the receiver was moved in azimuth to test the tracking capabilities of the resonant coupling techniques. The coupling associated with this movement can be associated with the magnetic field pattern than is illustrated in Figure 3-37 for the single feed case. As can be seen as the receiver moves in azimuth, the maximum coupling varies proportionally with this pattern. A comparison between the antenna pattern, and the coupling pattern in azimuth is shown in Figure 3-37. This test was repeated for all the structural variation, with the exception of the coplanar variation case. The coplanar structure varies in the plane perpendicular to the axis of rotation, and thus cannot have a common distance to test as compared to the other structures, which are varied in the plane of the axis of rotation.

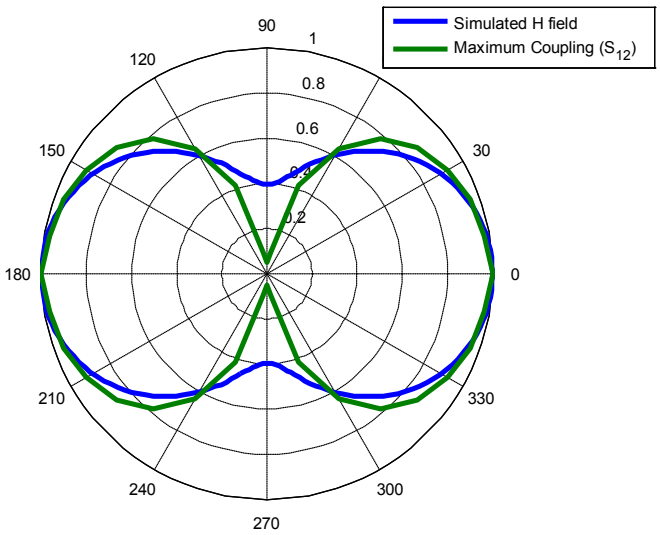


Figure 3-37 Maximum Coupling Pattern in Azimuth

As with the azimuthal variation, the coupling between elements can be represented by the distance between the elements. This is especially true for the distances between 1-10$r$ because the field begins a dissent out of the reactive near field (typically denoted as proportional to a $\frac{1}{R}$ attenuation). Figure 3-38 compares the attenuation as a function of distance for the single feed control case with the axially directed array. These measurements were made on the axis of rotation ($\theta = 0$).

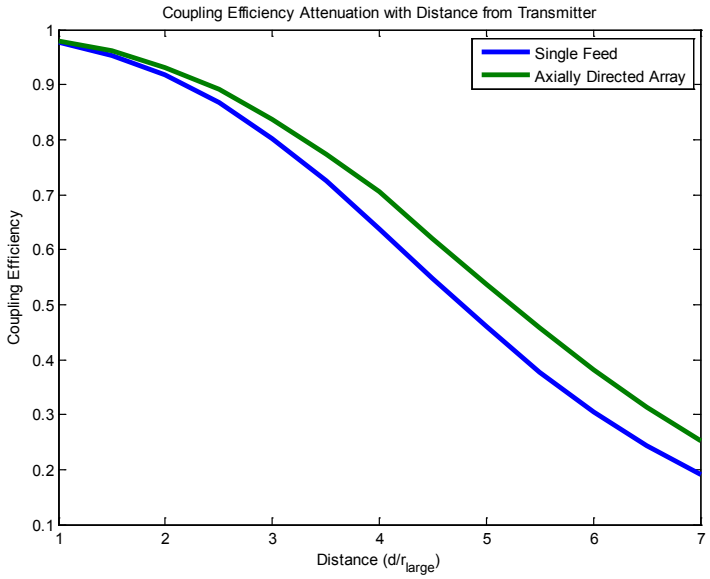


Figure 3-38 Distance Degredation of Coupling Axially Directed Array (3 Element)

As with the previous variation in azimuth, the coupling attenuation can be measured also as a function of angle off axis. Figure 3-39 displays this efficiency drop for the axially directed array structure. As can be expected, at distances greater than 150mm for this simulation, the greatest coupling occurs on the axis of rotation (θ=0). However, it seems closer to the transmitting loop the attenuation is less pronounced at any angle given the proximity of the receiver to the device.

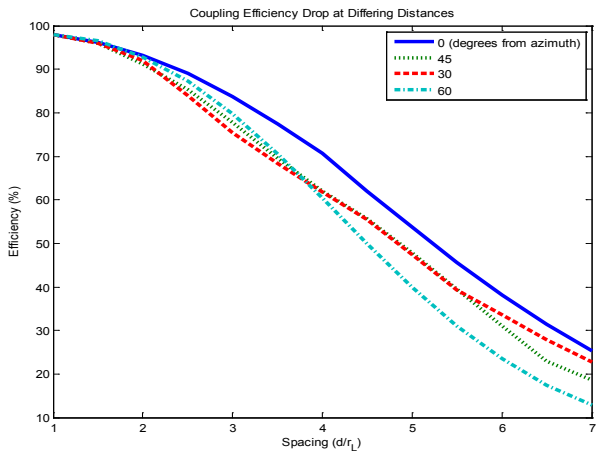


Figure 3-39 Coupling Degradation for Multiple Azimuthal Displacement Angles, Axially Directed Case

### 3.2.2 Lossless Element, Finite Ground Plane

The previous *f* response measurements were also conducted for the finite ground plane, as described in 3.1.3 for inductive coupling. The effect on the strength of the coupling was minimal, and the magnitudes of the finite ground with infinite ground varied by only .01dB, however, there was a shift in the optimal frequency that was used to tune the networks. Figure 3-41 shows the frequency response to the coupling strength between the two ground plane cases for a 5mm spaced axially directed array (3 elements).

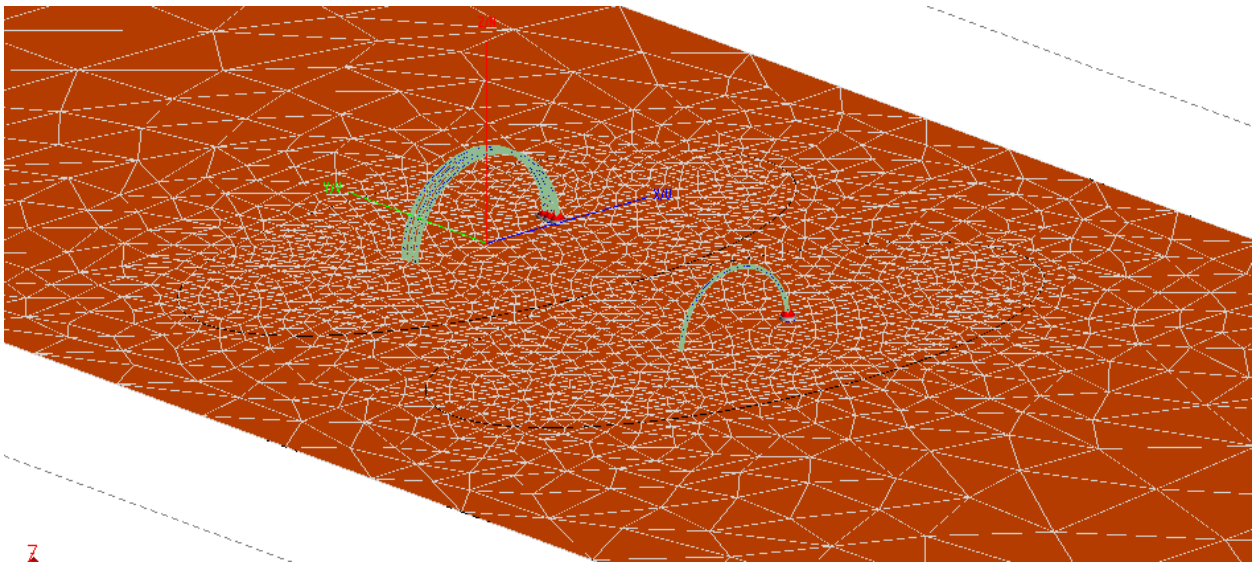

Figure 3-40 Finite Ground Meshing, Axially Directed Array Case

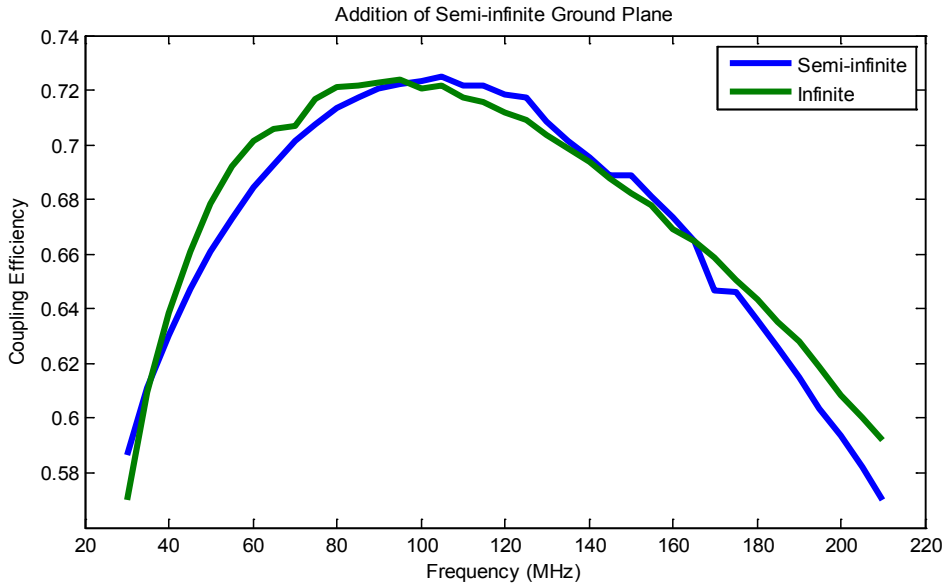


Figure 3-41 Comparison of Infinite/Finite Ground Cases for Optimal Frequency, Axially Directed Array

### 3.2.3 Axially Directed Array Structure

It can be discerned from the comparative results from the previous section that the axially directed array using multiple elements at the same radial size has more pronounced coupling that any structural variation

tested. In light of this observation a subset of tests were performed on this specific array, so as to optimize its structure for prototyping.

The structural spacing was varied, in order to observe the residual effects of gap capacitance between loops, as well as the increased near field magnetic field stored within the structure itself. The geometric variance is illustrated in Figure 3-42. Results from optimization show that as the spacing decreases between the elements, the magnitude of the coupling between that structure and the receiving element increases. This phenomenon is likely due to the tighter coupling between the loops themselves, causing an increase in stored magnetic energy in the structure. This will be more clearly examined in the validation field analysis at the end of this chapter.

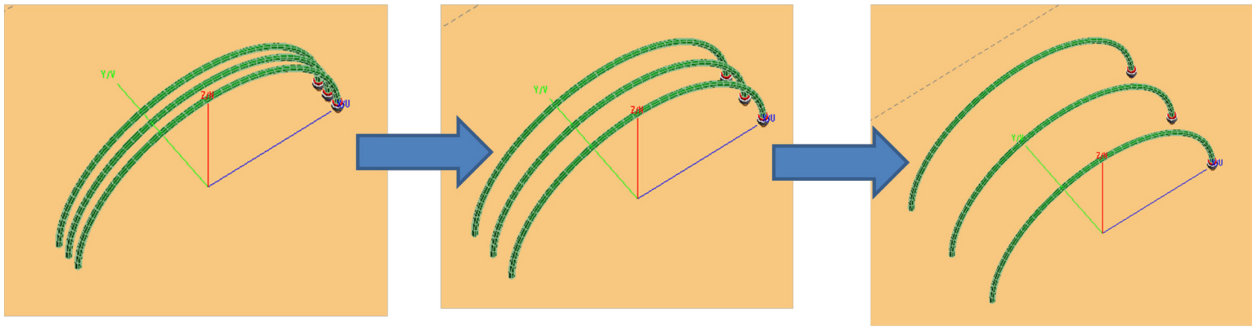

Figure 3-42 Element Seperation Modification

The optimized maximum coupling over the *f* range 30-210MHz for the varied spacing can be viewed in Figure 3-43.

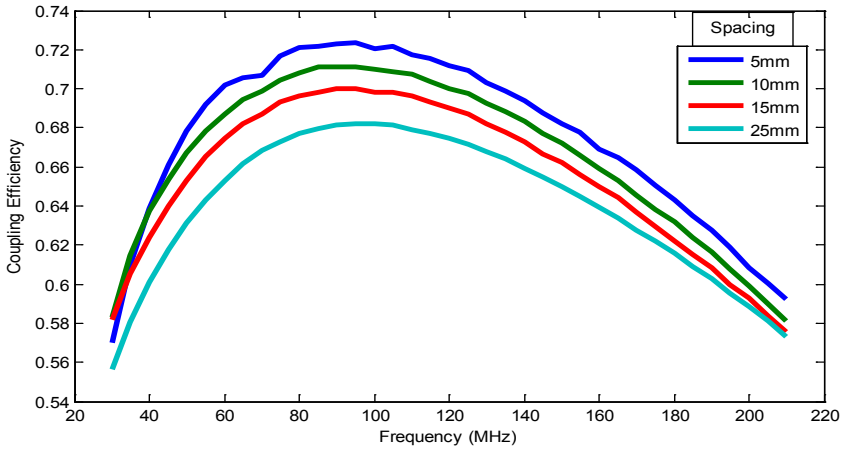


Figure 3-43 Comparison of Coupling Efficiency for Varying Element Separations

In order to have a nominal spacing value for this structure there needs to be some actual value to base it upon. For this particular case, the limiting factor to the spacing between the elements is the distance in between the small ground planes that are a part of the SMA connectors. These connectors are around 10mm in length (square), and thus the spacing should be set to a nominal value of 10mm.

This nominal spacing was used for the other geometric variation. In the structural comparative analysis, the amount of elements was set and kept at three to limit optimization and simulation time (simulation time significantly increases as the amount of ports in the S-parameter matrix increases). For the axially directed structure, it is important to understand the dynamics of how differing numbers of elements effect resonance. Figure 3-44 illustrates the aforementioned geometric variation.

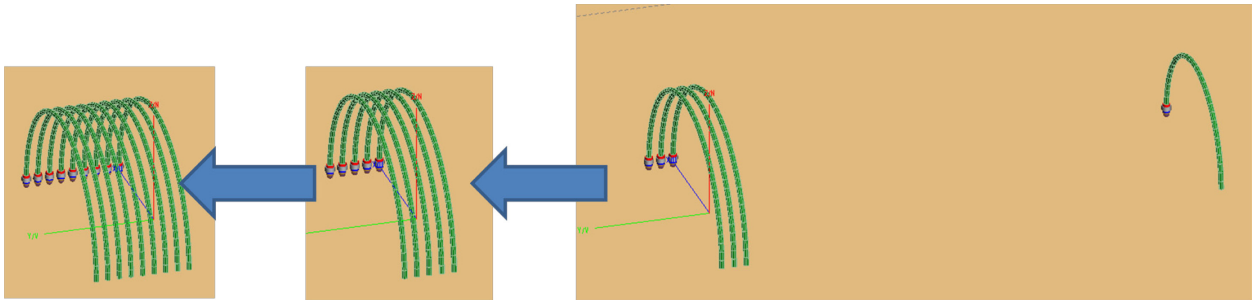

Figure 3-44 Addition of Elements to Axially Directed Array

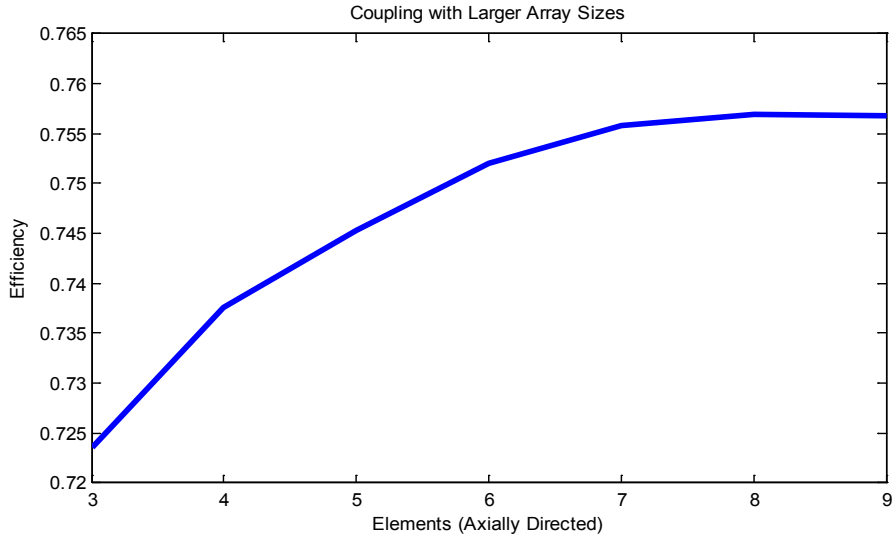


Figure 3-45 Coupling Efficiency Growth as Array Size Increases

In varying the amount of elements it can be seen that the transmitter/receiver coupling efficiency begins to increase, and then starts to become asymptotic (Figure 3-45 for spacing d=5mm). As the number of array elements begins to approach around 10, the distance between the first and last element is

in magnitude with the distance between the entire transmitting array to receiver (last element at d=50mm while receiver at d=200mm). The caveat with this particular variation comes in the optimized element values. The constraint on the inductors was broadened to see the total effect of the increased number of elements on the coupling efficiency. This constraint was then applied ($L \leq 6000nH$) and kept constant throughout the testing. The spacing was normalized to 15mm, in order to better represent what could be implemented. Figure 3-46 shows the response of the networks as the elements increased.

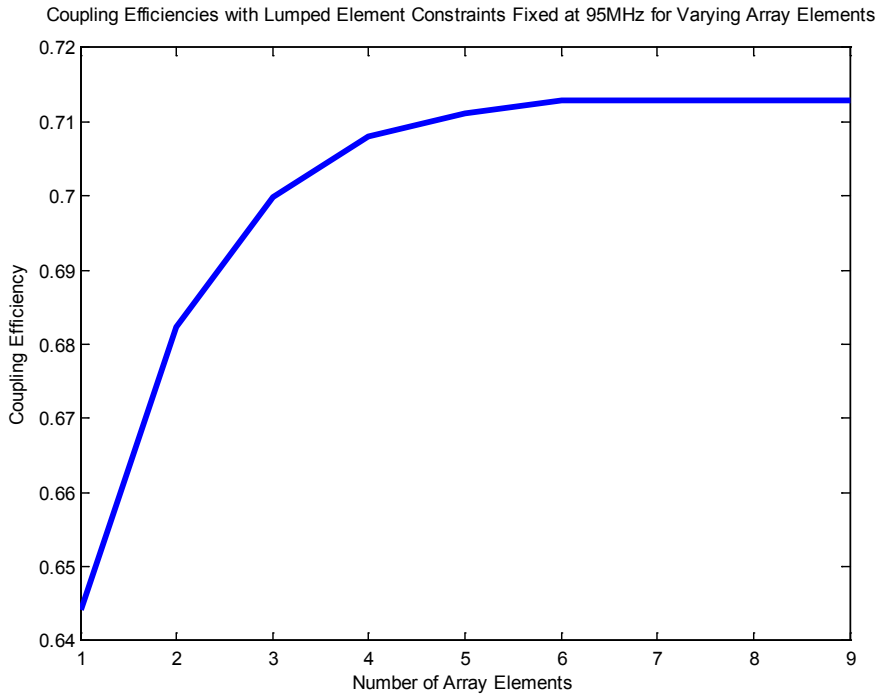


Figure 3-46 Coupling for Greater Array Sizes with Inductor constraint L< 6000nH

The ability to implement multiple loops diminishes as the number of loops exceeds 4, due to the lack of shielding/isolation between the resonant networks. The prototype will require all networks to be in close proximity to each other, which places the inductive elements within distances of significant inductive coupling.

### 3.2.4 Addition of Loss to Resonant Networks

The addition of a Q value for the resonant circuit elements will allows for a more accurate representation of the coupling that can occur between the two resonant networks. This is achieved by using the element model "induct_q" in ADS with a defined Q at a certain reference frequency. This Q, for definition's sake, is measured by using the bandwidth equation. The same experimental methodology was used in adding a loss factor to the resonant networks as with the lossless case. The same 3D full wave simulation results

were used as the representation of the EM signature from the image half-loops elements. Instead, the variation occurred within the lumped inductor element itself. Figure 3-47 gives a sweep for differing inductor Q's and the maximum magnitude of the coupling ($S_{12}$) between the networks for the single feed structure. Notice that as the Q is exponentially increased, the coupling begins to become asymptotic to the lossless case.

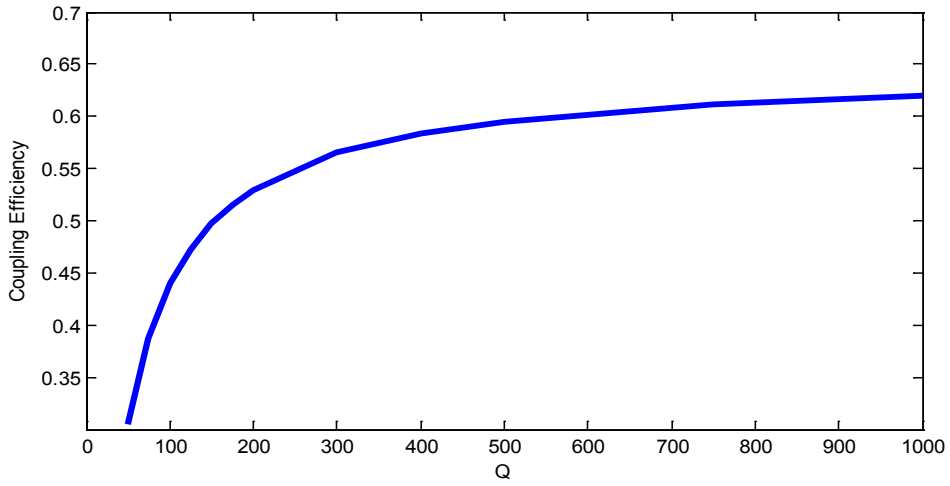


Figure 3-47 Coupling Efficiency with Respect to loss within the Inductor Element (shown as Q)

From an engineering perspective, it becomes difficult to create a helical inductor with a Q past 100 without varying some material and structural properties of the helix for this *f* regime (10-250MHz). This will be further discussed in Chapter 5 under "Coil Construction".

### 3.2.5 Statistical Variance Using Monte Carlo Analysis

Another advantage to utilizing a circuit simulation model to optimize the resonant networks is the ability to quickly analyze worst case scenarios during implementation. For a network that has an extremely high Q, it is important to analyze the variation that might occur during tuning to see the effect of such a variance on the strength of coupling overall.

The main method within the ADS environment to analyze variance is called a "yield" analysis. The particular technique used within the yield analysis spec is the "Monte Carlo Yield", which allows the user to pinpoint a certain aspect of the model under simulation, and vary it with a standard deviation percentage. The result is a combination of multiple *f* domain sweeps that show a variance around a single or multiple parameters. The particular yield analysis was applied to the lossless, infinite ground, single feed case in order to reduce the variance to only a single parameter. With knowledge of how the resonant network would be tuned, it was obvious that the shunt capacitor would be the only varying lumped element. A Monte Carolo yield analysis was performed for both of the shunt capacitors (transmitting and

receiving side) with a set of standard deviations. Figures 3-48 show these results with a 1% standard deviation, with 250 iterations being considered. Observing these results shows that at 1% deviation from the optimized capacitance, there can be a 25dB shift in the overall coupling efficiency. A summation of these observations for various standard deviations can be found in Table 3-5.

Table 3-5: Statistical Variances and Maximum Coupling

| Standard Deviation from Norm | Max $S_{12}$ (dB) | Min $S_{12}$ (dB) | $\Delta S_{12}$ (dB) |
|---|---|---|---|
| .01% | -1.950 | -1.959 | .009 |
| .1% | -1.95 | -2.99 | 1.04 |
| 1% | ~-2 | ~-27 | ~25 |
| 10% | ~-2 | ~-65 | ~63 |
| 50% | ~-2 | ~-90 | ~88 |
| 100% | ~-2 | ~-105 | ~103 |

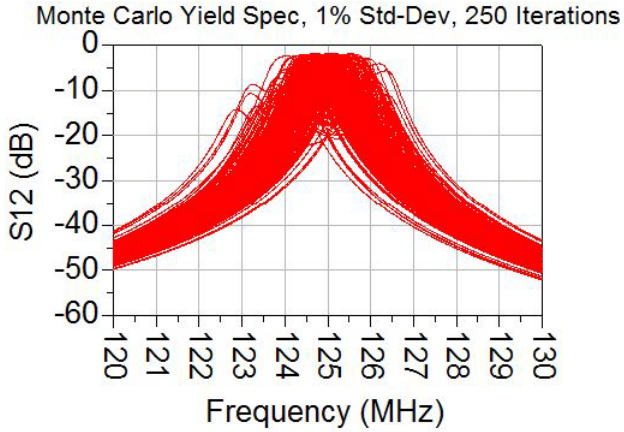


Figure 3-48 Monte Carlo Sensitivity Analysis for 1% Std. Deviation at 250 Iterations

### 3.2.6 Phasing Analysis

In order to determine whether the phasing of the networks effects the strength of the coupling between array and receiver, the networks must not only be isolated from each other, but the small phase difference between networks needs to be set to zero. The method that was utilized to delineate whether the phase difference between the elements was a useful quantity to the directivity and strength of the coupling was to completely eliminate all other resonant networks, save one. This network was optimized in order to find the proper tuning for maximum coupling. Figure 3-49 shows this transformation in ADS.

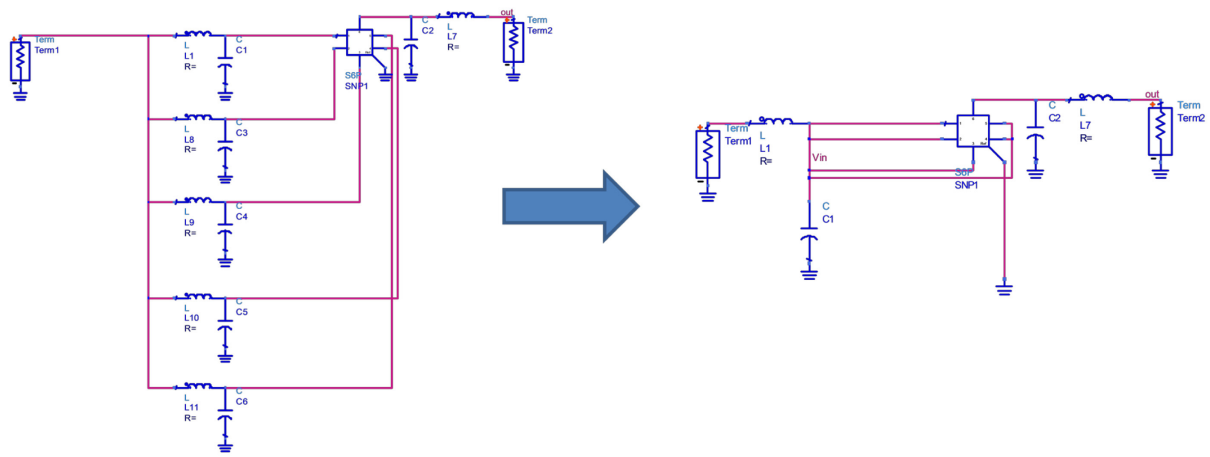


Figure 3-49 Network Changes with and without Element Phasing

This transformation allows the phasing at each port to be locked with the phase of all ports in the array. For instance, the variation of phase within the structural setup in Figure 3-49 (left) at optimization can be seen in Table 3-6. The element numbers correspond with the array element with respect to its distance from the receiver.

Table 3-6: Phasing on Elements in Axially Directed Array

| Element | $V_{phase}$ | $I_{phase}$ | $S_{phase}$ |
|---|---|---|---|
| 1 | -84.45 | -174.25 | 89.8 |
| 2 | -84.3 | -173.81 | 89.5 |
| 3 | -84.75 | -174.65 | 89.9 |
| 4 | -84.75 | -174.41 | 89.8 |
| 5 | -84.15 | -173.3 | 89.2 |

The maximum variance in phase is around .6 degrees at resonance. It is unclear the exact correlation between the phasing of the voltage and current at each port and the absolute strength of coupling between the entire network. In order to evaluate this phenomena, the network was then optimized with the network setup that is illustrated in Figure 3-49 (right). In this case it is known that the voltage phase on each port will be locked with the phase of adjacent ports. However, when the structure was optimized it was noticed that the current through each port was in fact phased. Table 3-7 displays the phasing at each port.

Table 3-7: Current Phase on Elements

| Element | Current Phase |
|---|---|
| 1 | -174.54 |
| 2 | -174.64 |
| 3 | -174.71 |
| 4 | -174.75 |
| 5 | -174.76 |

The cause of the current phasing on each of the elements is unclear, and must be determined in order to defend the need for phasing. Calculating the mutual inductance without the networks connected could give some insight to the current distributions on each element given a 6 port input. The S-parameter matrix is determined by

$$S_{ij} = \frac{V_i^-}{V_j^+}$$

which isn't prudent to use when determining the current distributions on all elements. It is possible to transform this matrix to another in terms of current, however this requires the use of a characteristic impedance $Z_0$, and might lend itself to numerical error (the error must be within the bounds of the phase variation from Table 3-7). Instead, a more favorable method exists with the mutual inductance matrix $L_{nn}$.

#### *3.2.6.1 Isolation/Mutual Inductance Method*

In order to validate the cause of the optimal phasing on the loops, the mutual inductance between each of the loops needs to be calculated. The mutual inductance L, can be calculated by:

$$v_i = \sum_{j=1}^{n} L_{ij} \frac{di_j}{dt}$$

Which for an N-port [time harmonic] network becomes:

$$v_n = L_{n1} j\omega I_1 + L_{n2} j\omega I_2 + \cdots L_{nn} j\omega I_n$$

Where $L_{ii} \approx L_{i+1,i+1}$ , ..., $L_{nn}$. To find the original inductances of the loops the disconnected S-parameter matrix was utilized, and the $v$ and $\frac{di}{dt}$ of each individual loop was measured. For simplicity's sake, since all of the imaged half-loops are identical, the inductance of each can be considered nearly the same. Figure shows the circuit design setup for the measurement of the single loop inductance.

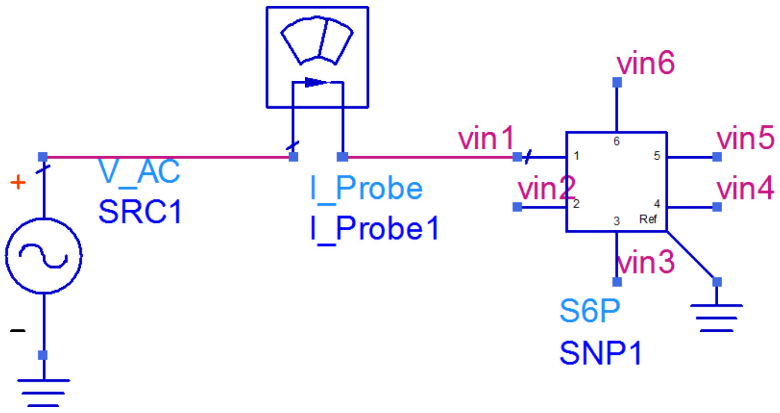


Figure 3-50 Model Setup for Measurement of Mutual Inductance

In order to negate the parasitic effects of the other loops, each loop interaction was measured separately. This was completed by circuit simulating the network with a single excitation and all other elements as open circuits. All elements within the array are identical (same radius and wire width), and the geometry of the array is symmetric (all elements are spaced at least 15mm away from each other and at most 60mm), except for the receiver. These characteristics allow the measurements of these two element full wave simulations to be used multiple times within the same matrix by *reciprocity*. For the inductance matrix it can be shown that:

$$L_{11} \approx L_{22} \ldots \approx L_{nn}$$

and

$$L_{nm} \approx L_{mn}$$

This principal of reciprocity fills $L_{nn}$ with a 5 by 5 distribution of currents, which describes the interaction of the array elements. There is however, a small inductive interaction between this array and the receiver loop placed at 200m. The placement of this receiver brings anti-symmetry to the geometry of the entire structure. This receiver inductance, as can be expected, showed a weaker interaction than inter-array element interaction.

The matrix problem can be described by the following equation:

$$\begin{bmatrix} V_1 \\ V_2 \\ \vdots \\ V_n \end{bmatrix} = \begin{bmatrix} L_{11} & \dots & L_{1n} \\ \vdots & \ddots & \vdots \\ L_{n1} & \dots & L_{nn} \end{bmatrix} \begin{bmatrix} \frac{dI}{dt_1} \\ \frac{dI}{dt_2} \\ \vdots \\ \frac{dI}{dt_n} \end{bmatrix}$$

By itself, by simply measuring currents and voltages, it is difficult to determine the inductance matrix. Even assuming reciprocity, $L_{11} = L_{22}$, and $n$ equations we have $\frac{n^2-n}{2}$ different unknowns. For matrices above $n$=3 we have more unknowns than equations, which requires the addition of equations from Ohm's law. This, however, is not completely necessary. It is possible to excite a single element while keep all other elements open circuit, and measure the voltages at each port, with the current of the excited loop. This will allow the matrix to be simplified to

$$\begin{bmatrix} V_1 \\ V_2 \\ \vdots \\ V_n \end{bmatrix} = \begin{bmatrix} L_{11} \\ L_{21} \\ \vdots \\ L_{n1} \end{bmatrix} \begin{bmatrix} \frac{dI}{dt_1} \\ 0 \\ \vdots \\ 0 \end{bmatrix}$$

for an excitation on element 1. By interchanging the excitation port the entire inductance matrix can be filled column by column.

Once the current interactions were measured with reference voltage $V_1$ , the mutual inductance matrix $L_{nm}$ was determined. As with the current matrices, the mutual inductance matrix is reciprocal about the 6x6 portion with the extra column and row being the receiver interaction. This mutual inductance matrix was calculated and the magnitude of the results are shown below.

Table 3-8: Mutual Inductance Matrix Axially Directed Array (5 element)

| | 1 | 2 | 3 | 4 | 5 | 6 |
|---|---|---|---|---|---|---|
| 1 | 1.30E-07 | 4.41E-08 | 2.48E-08 | 1.54E-08 | 1.01E-08 | 7.50E-10 |
| 2 | 4.41E-08 | 1.31E-07 | 4.42E-08 | 2.48E-08 | 1.54E-08 | 6.26E-10 |
| 3 | 2.48E-08 | 4.42E-08 | 1.31E-07 | 4.42E-08 | 2.48E-08 | 5.27E-10 |
| 4 | 1.54E-08 | 2.48E-08 | 4.42E-08 | 1.31E-07 | 4.41E-08 | 4.48E-10 |
| 5 | 1.01E-08 | 1.54E-08 | 2.48E-08 | 4.41E-08 | 1.30E-07 | 3.84E-10 |
| 6 | 7.50E-10 | 6.26E-10 | 5.27E-10 | 4.48E-10 | 3.84E-10 | 1.30E-07 |

We know that from the knowledge of the mutual inductance and inductance we can find the coupling coefficient from the expression:

$$k = \frac{L_{nm}}{\sqrt{L_n L_m}}$$

The following is the magnitude of the coupling coefficients for the network:

Table 3-9: Coupling Coefficient Matrix Axially Directed Array (5 element)

| $k$ | 1 | 2 | 3 | 4 | 5 | 6 |
|---|---|---|---|---|---|---|
| 11 | 1 | 0.33837 | 0.189856 | 0.118045 | 0.077432 | 0.005756 |
| 22 | 0.33837 | 1 | 0.338629 | 0.18999 | 0.118047 | 0.004799 |
| 33 | 0.189856 | 0.338629 | 1 | 0.338626 | 0.189856 | 0.004043 |
| 44 | 0.118048 | 0.189995 | 0.338634 | 1 | 0.338375 | 0.003438 |
| 55 | 0.077432 | 0.118047 | 0.189856 | 0.338367 | 1 | 0.002946 |
| 66 | 0.005756 | 0.004799 | 0.004043 | 0.003438 | 0.002946 | 1 |

These matrices give an overview of the amount of inductive coupling we have between multiple parts in an array. As illustrated, the amount of inductive coupling between the first and last elements in the array have at least 94% stronger inductive coupling than does any element in the array with the

receiver. The real significance of these values, however, is to validate the original premise of determining the cause for current phasing after optimization.

The technique for validation required the resonant networks to be optimized first. Once optimization/tuning was completed (ie. Optimal coupling was reached), the resultant inductance matrix found from the previous steps above was used to predict the phases for current on each of the elements. If the phases could be accurately predicted by the cross-inductive model with no resonant networks connected, then it can be assumed that any phasing during resonance is a consequence of mutual induction, and not the spurious effects of the resonant coupling or numerical error. As can be seen in the table below comparing the predicted phase with the simulated phase, the prediction matched simulation at a level $\gg$99.9% accuracy. This explains that the phase variation between the elements is not due to simulation numerical error, or the spurious effects of resonant coupling, but lie directly within the signature of the mutual inductive coupling between the elements.

Table 3-10: Predicted Versus Expected Current Phases

| Element Number | Predicted *I* phase | Simulated *I* phase |
|---|---|---|
| 1 | -173.4510158359123 | -173.4524 |
| 2 | -173.5945247646668 | -173.6023 |
| 3 | -173.7211866525317 | -173.6889 |
| 4 | -173.7420640549565 | -173.7499 |
| 5 | -173.7752783037647 | -173.7767 |
| 6 | 81.632952928897340 | 81.632952 |

## 3.3 Field Validation FEKO®

### 3.3.1 Single Feed Structure

Resonant networks were imported to FEKO using the general network option. This was applied most importantly to analyze the field variations at resonance. The following Figures show different cross-sections and the field components within them (time harmonic case).

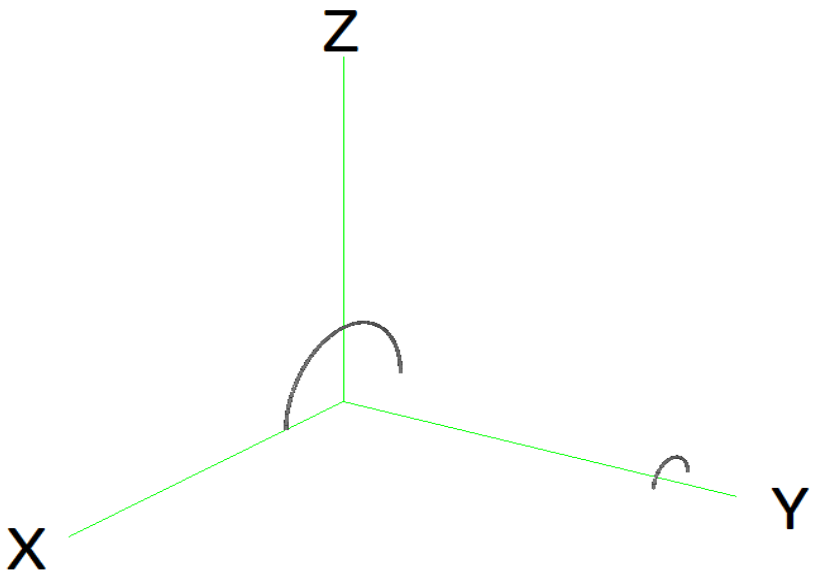


Figure 3-51 Geometry of Loops and Fields in FEKO

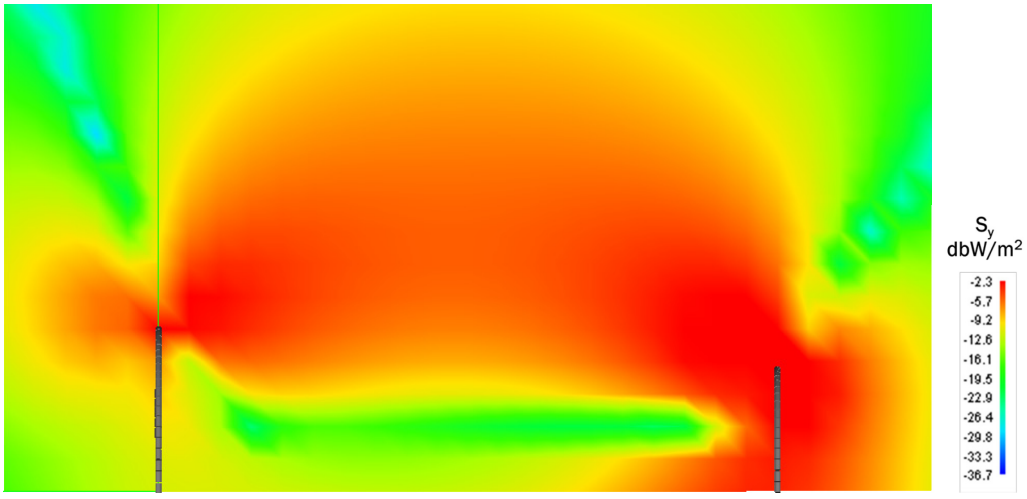

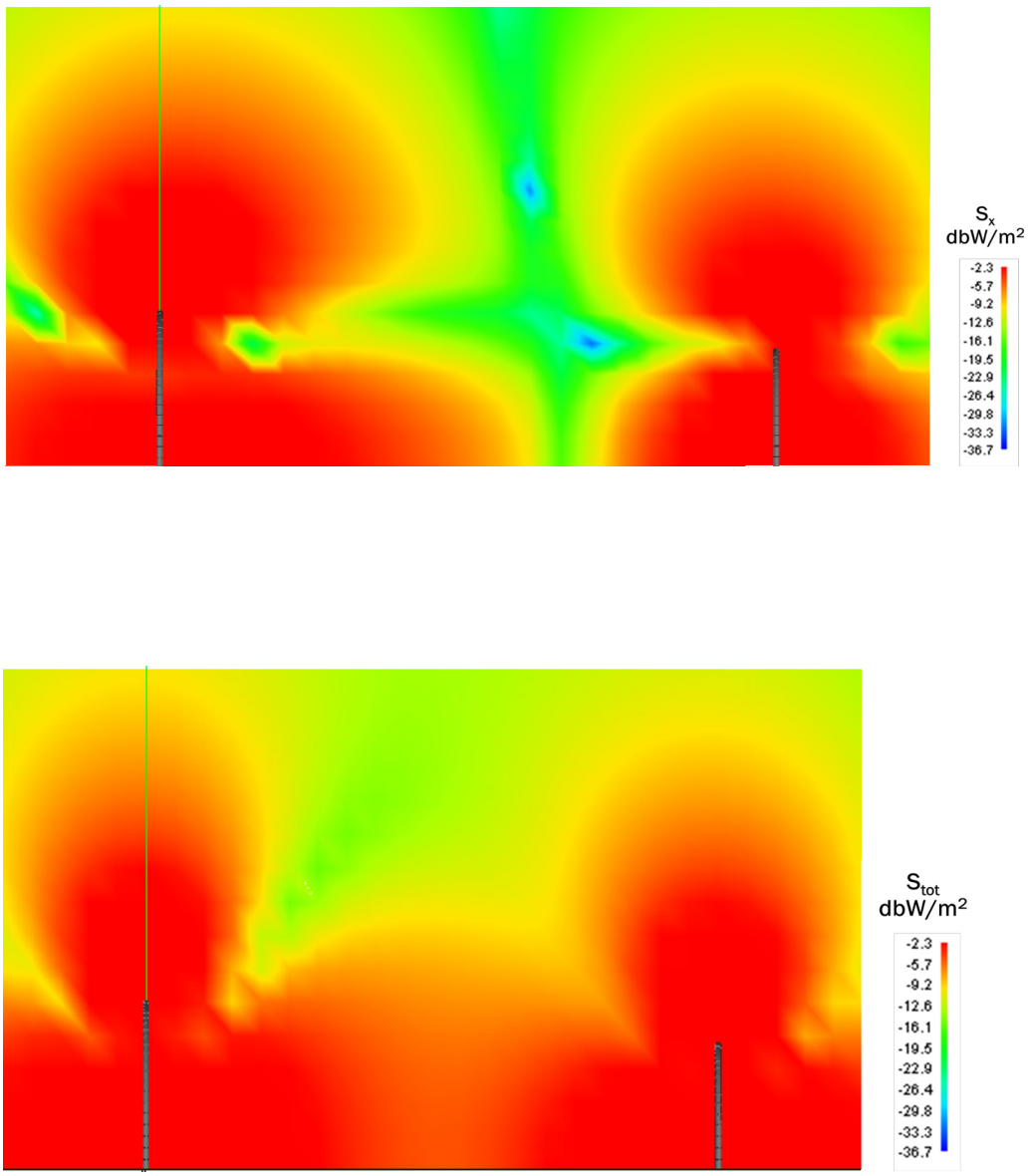


Figure 3-52 Field Variations Single Feed Case
Top: Y-Directed Poynting Vector
Middle: X-Directed Poynting Vector
Bottom: Total Poynting Vector

**ZY-plane Cross-Sections**

As was tested previously, it is prudent to test the coupling at varying positions in space. This was applied to the single feed case by following the same numerical method, with elements rearranged in azimuth from the beginning. The following figures show the fields for a receiver that is moved in azimuth to an angle $\theta = 45^{o}$.

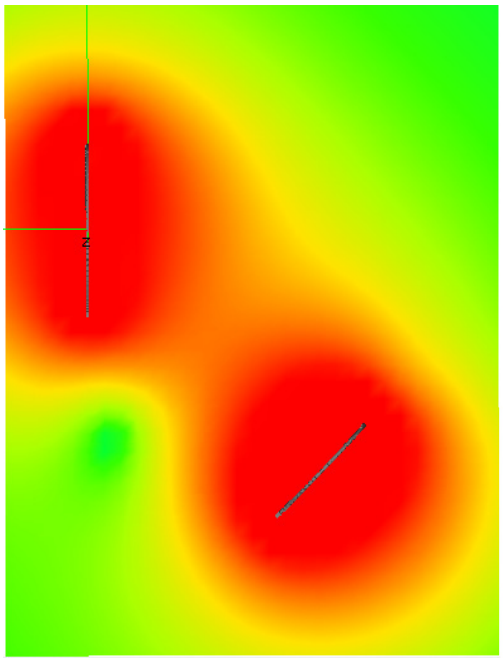

$S_{tot}$
$dbW/m^2$

-7.2
-10.4
-13.5
-16.7
-19.9
-23.1
-26.3
-29.5
-32.6
-35.8
-39.0

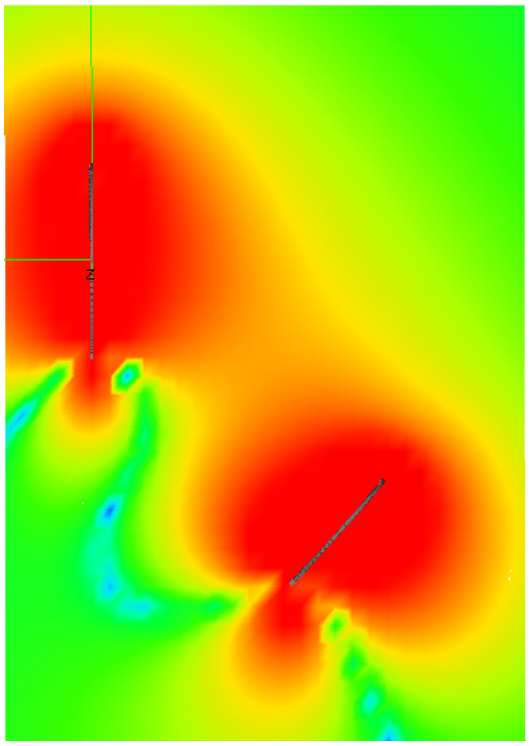

$S_x$
$dbW/m^2$

-7.2
-10.4
-13.5
-16.7
-19.9
-23.1
-26.3
-29.5
-32.6
-35.8
-39.0

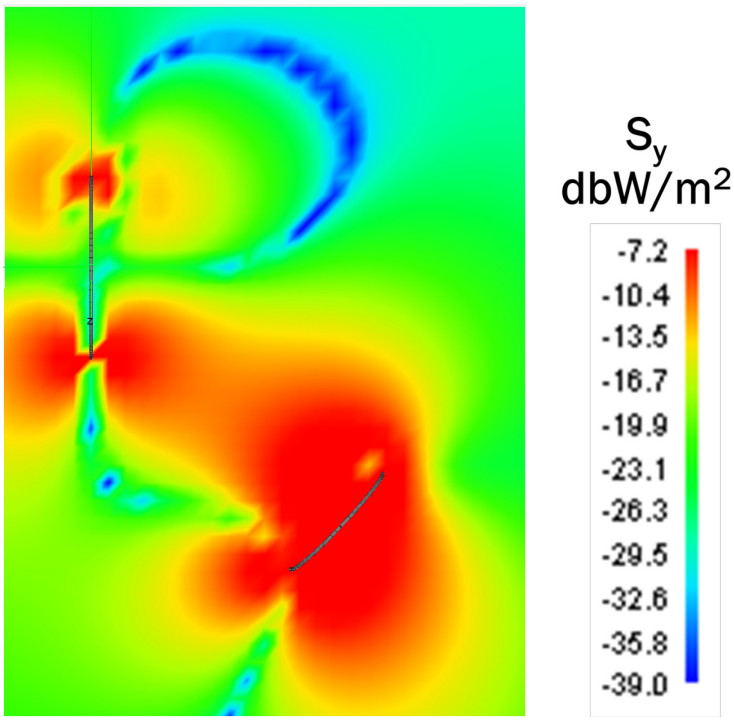


Figure 3-53 Field Variations Single Feed Case with Azimuthal Variation
Top: Total Poynting Vector
Middle: X-Directed Poynting Vector
Bottom: Y-Directed Poynting Vector

**XY-Plane Directional Cross-Section**

The Poynting vectors displayed are the real time averaged portion of the total vector. The XY plane illustrations show the real valued power flow at a slight distance away from the ground plane (approximately 1mm). The clearest view for showing the magnetic field line path for power flow comes from Figure 3-52 (top). This illustrates the arching line of power flow, and its directionality when the receiver has no azimuthal variation.

### 3.3.2 Axially Directed Array Structure

The same validation was repeated with the axially directed array (with no staggered elements). The following Figures show the planar cross-sections of the Poynting Vector.

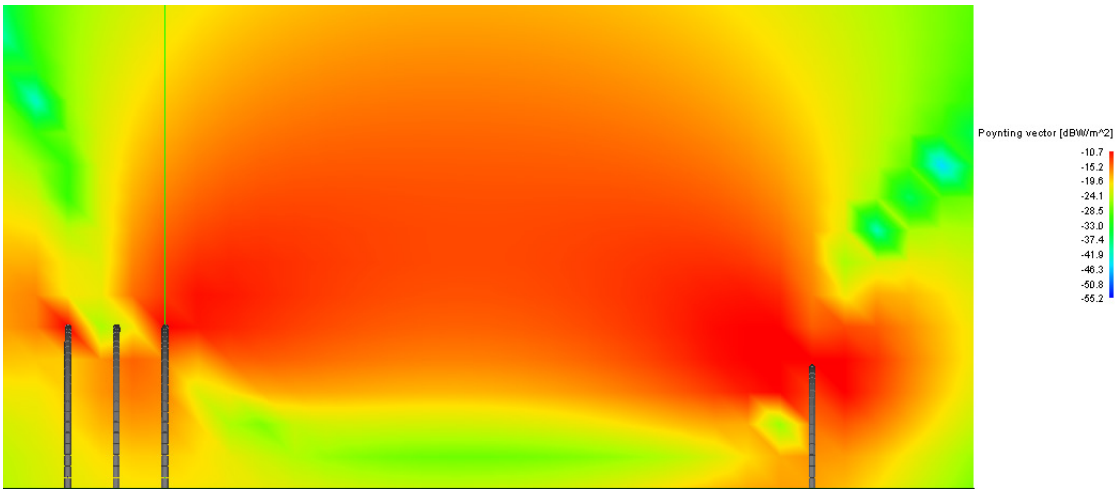
Poynting vector [dBW/m^2]
-10.7
-15.2
-19.6
-24.1
-28.5
-33.0
-37.4
-41.9
-46.3
-50.8
-55.2

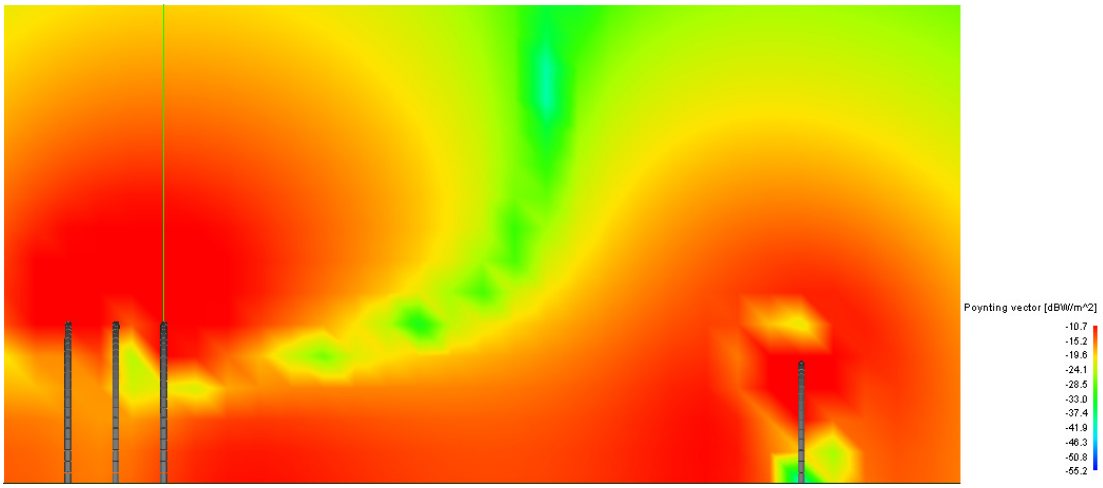
Poynting vector [dBW/m^2]
-10.7
-15.2
-19.6
-24.1
-28.5
-33.0
-37.4
-41.9
-46.3
-50.8
-55.2

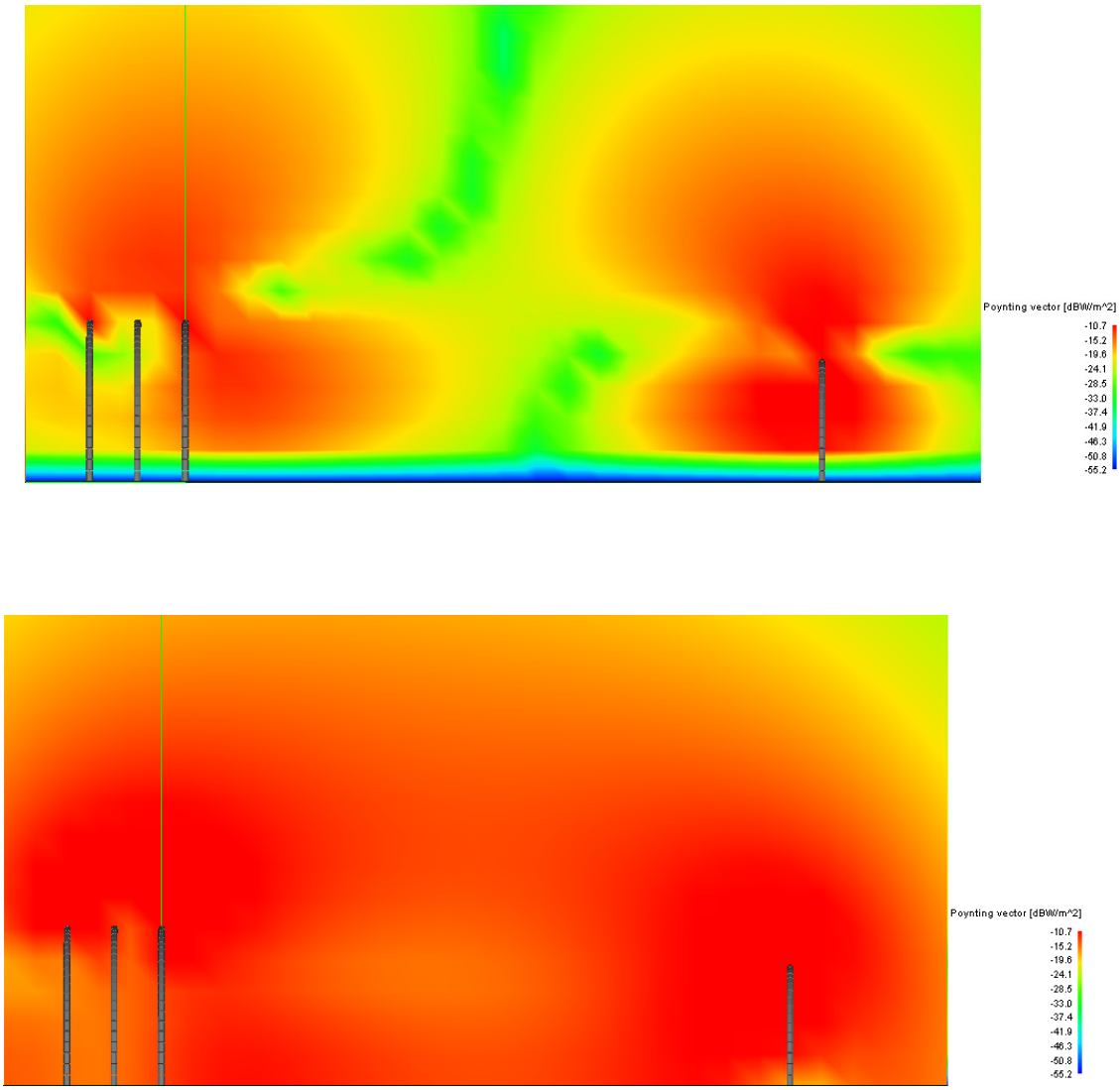


Figure 3-54 Field Variations Axially Directed Array Case
Top: Y-Directed Poynting Vector
Middle (top): X-Directed Poynting Vector
Middle (bottom): Z-Directed Poynting Vector
Bottom: Total Poynting Vector

**ZY-Plane Cross Sections**

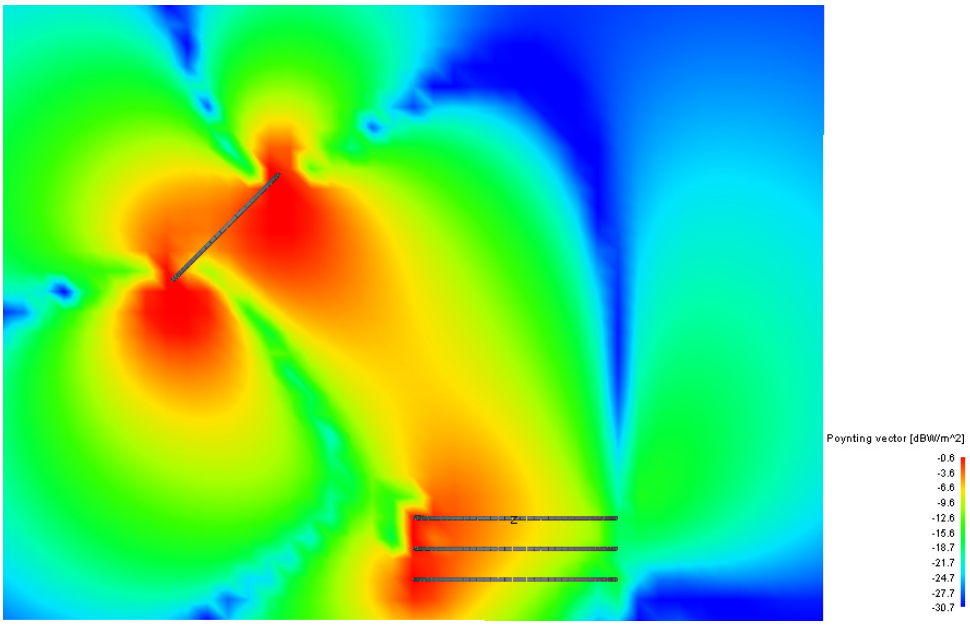
Poynting vector [dBW/m^2]
-0.6
-3.6
-6.6
-9.6
-12.6
-15.6
-18.7
-21.7
-24.7
-27.7
-30.7

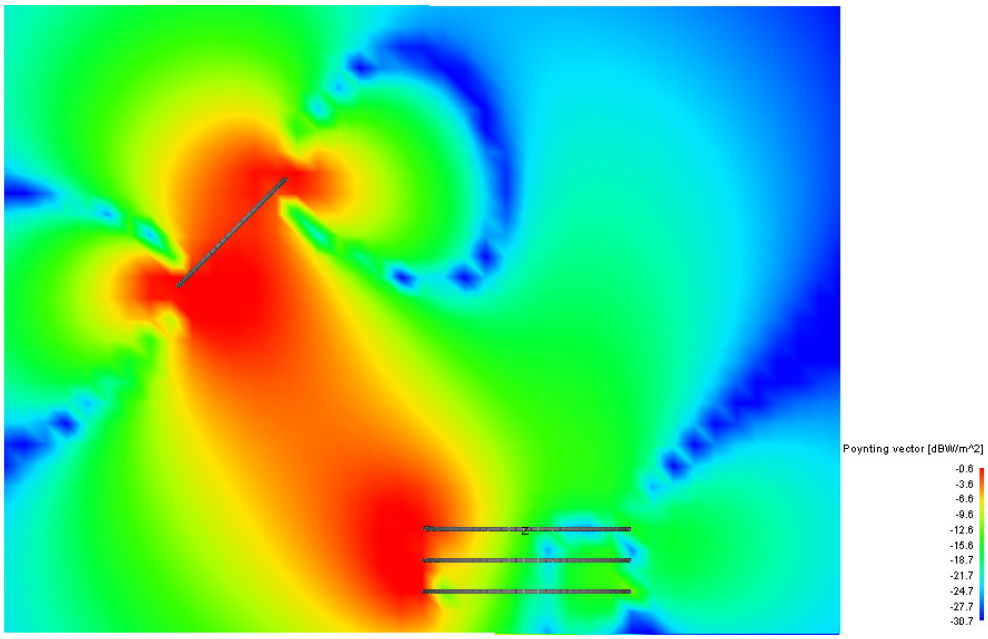
Poynting vector [dBW/m^2]
-0.6
-3.6
-6.6
-9.6
-12.6
-15.6
-18.7
-21.7
-24.7
-27.7
-30.7

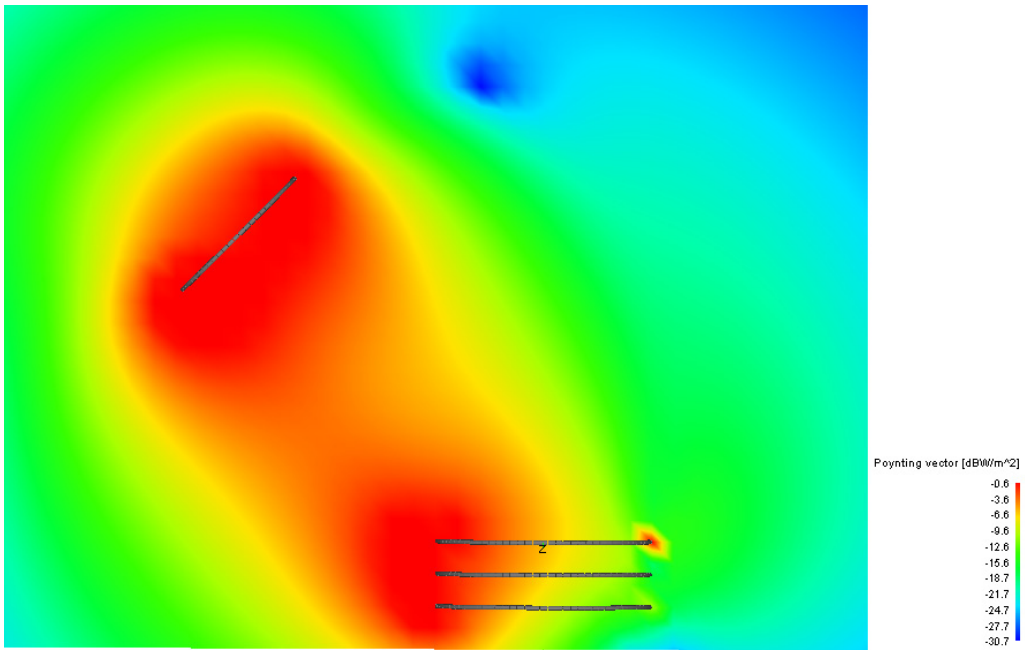


Figure 3-55 Field Variations Axially Directed Array Case with Azimuthal Variation
Top: Y-Directed Poynting Vector
Middle: X-Directed Poynting Vector
Bottom: Total Poynting Vector

**XY-Plane Cross Sections**

An interesting observation about the field patterns for the axially directed array are the y-directed Poynting vector in the ZY-plane cross section. It seems as though the second element in the array is not coupling with the receiver in the y-direction. This closely resembles the phenomena that occurs in the Yagi-Uda array, and allows for beam forming capabilities within the array.

This observation about the reflective nature of a select portion of the elements expresses the need for field validations with greater numbers of elements. In this way the effect of each individual element can be analyzed to see its contribution to the structures coupling capability as a whole. This also gives insight as to how the optimizer tuned the resonant networks. The following figures illustrate the coupling with a 5 element array.

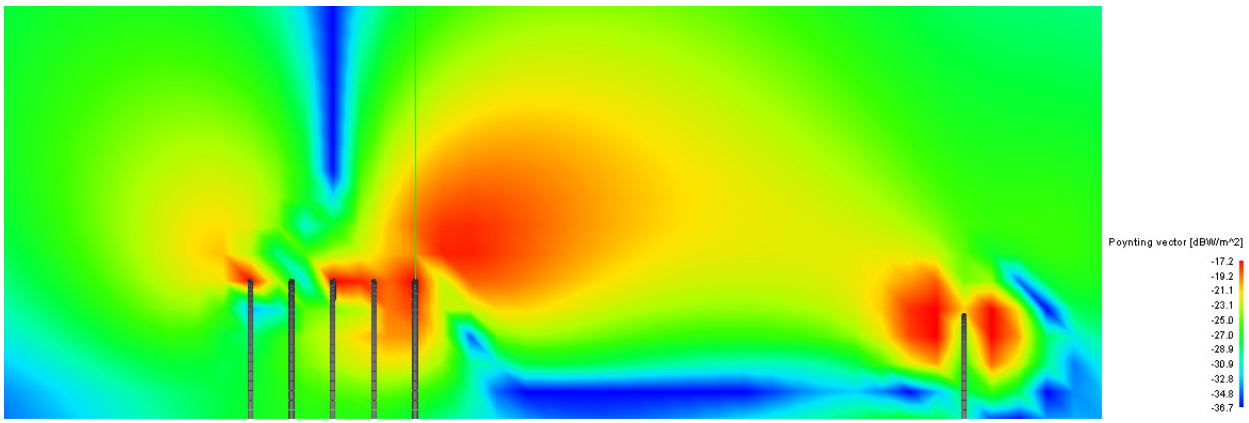
Poynting vector [dBW/m^2]
-17.2
-19.2
-21.1
-23.1
-25.0
-27.0
-28.9
-30.9
-32.8
-34.8
-36.7

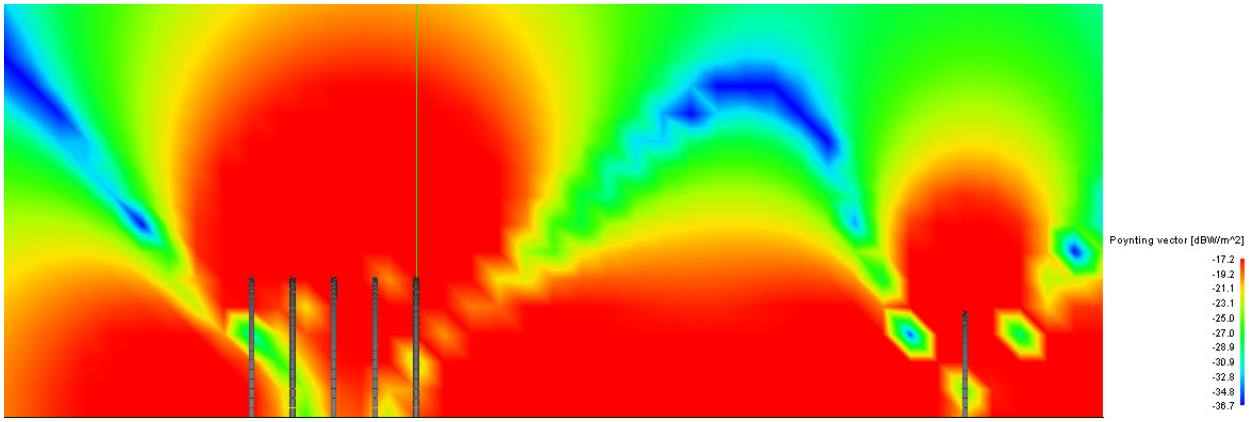
Poynting vector [dBW/m^2]
-17.2
-19.2
-21.1
-23.1
-25.0
-27.0
-28.9
-30.9
-32.8
-34.8
-36.7

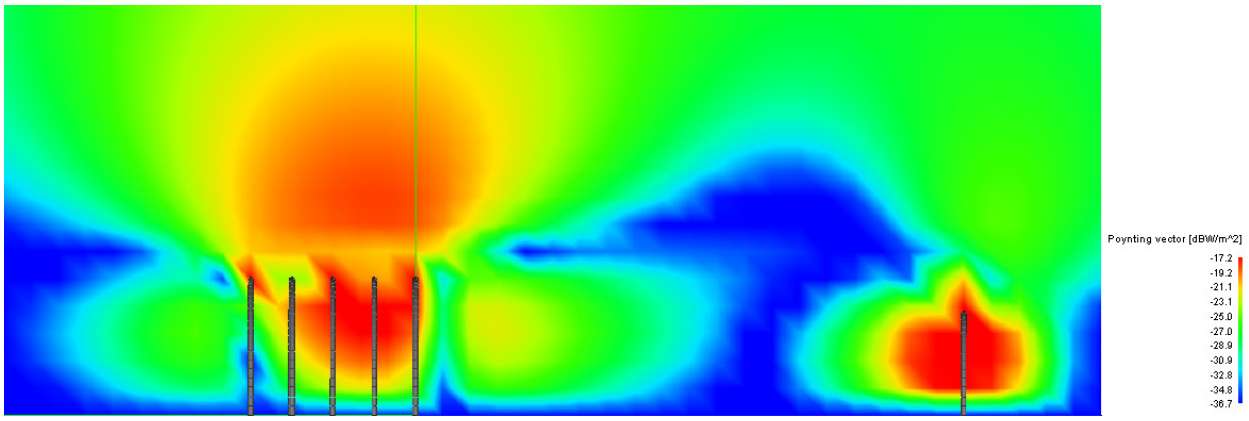
Poynting vector [dBW/m^2]
-17.2
-19.2
-21.1
-23.1
-25.0
-27.0
-28.9
-30.9
-32.8
-34.8
-36.7

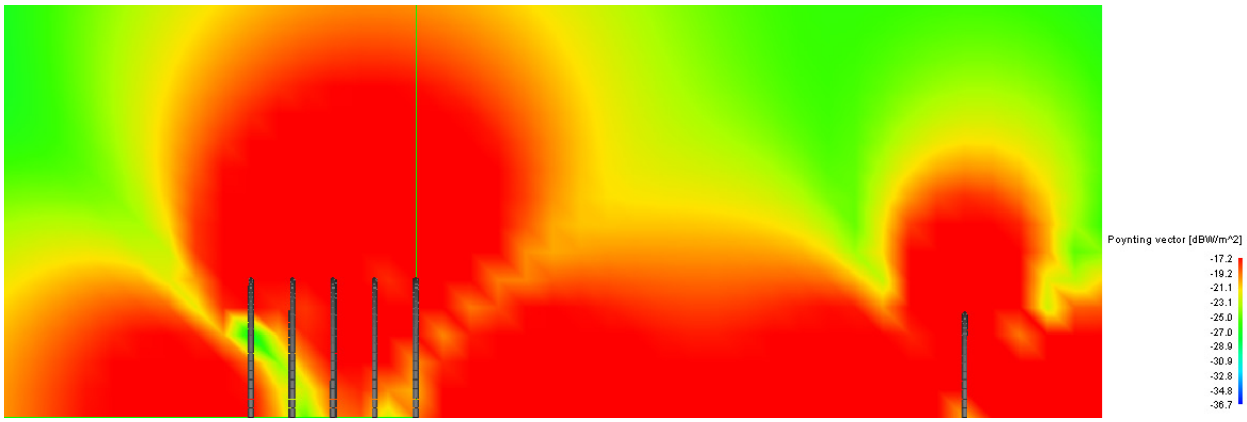

Figure 3-56 Field Variations Axially Directed Array Case (5 Element)
Top: Y-Directed Poynting Vector
Middle (top): X-Directed Poynting Vector
Middle (bottom): Z-Directed Poynting Vector
Bottom: Total Poynting Vector

## 3.4 Strip-loop Coupler Design

Described in section 4.2.3, the elements within an axially directed array can be separated and converged to give differing coupling strengths. As the element spacing converges to zero, the coupling between the array and the receiving element seemed to become stronger. This phenomena is closely related to the strength of the magnetic field, which is also related to the distance between each element and the amount of inductive coupling between them. In light of this correlation, it was determined that another antenna candidate could be used to further strengthen coupling achieved. This element structure takes advantage of the benefits observed by combining the spacing of the elements into a continuous sheet, or strip. This strip was then curled along the center axis of the wire's geometry to form a half imaged strip-loop design. An illustration of this design can be found in Figure 3-57. The thickness of the strip was set to 1mm and the width of the strip in the direction of coupling (y-direction) was 30mm.

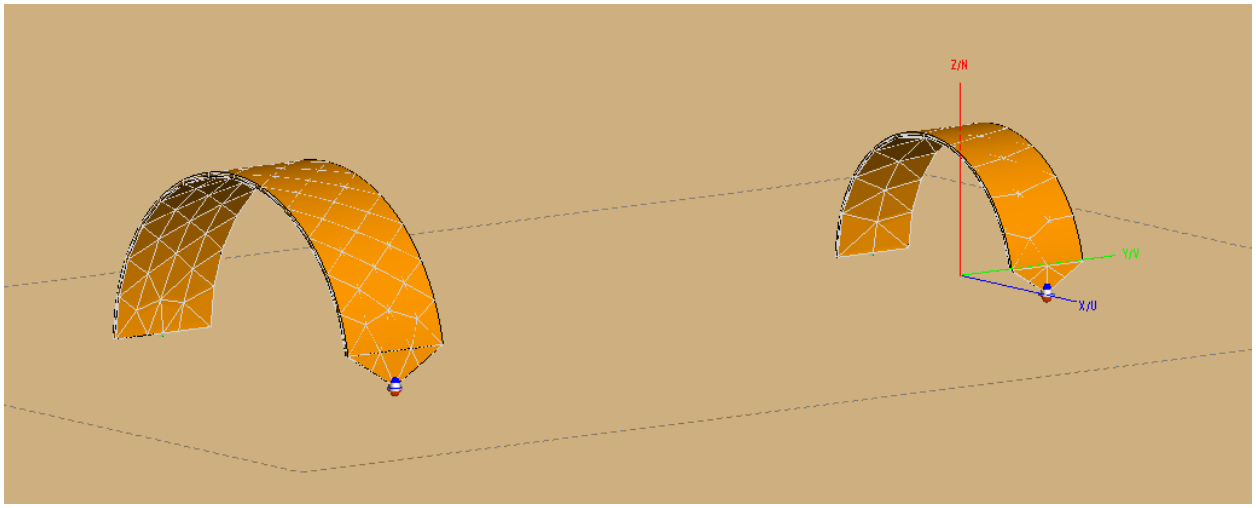


Figure 3-57 Strip-Loop Structural Design in FEKO

This structure was optimized/tuned in a similar fashion to the other structures under consideration. As can be seen from Figure 3-59, the optimal frequency was observed to be 80MHz. This frequency is slightly lower than that of any of the other structures under test. The strongest coupling between the two elements, with the same radius, was -.63875dB (corresponding to an 86.3% efficiency), and for transmitter and receiver radii 50mm 37.5mm respectively the $S_{12}$ was -0.9028091dB (corresponding to an 81.2% efficiency) at 90MHz. A comparison between the strip-loop model and the wire model can be seen in Figure 3-58 for 95MHz, lossless, and differing radii. This figure was taken during validation of the circuit simulation model (imported back into FEKO).

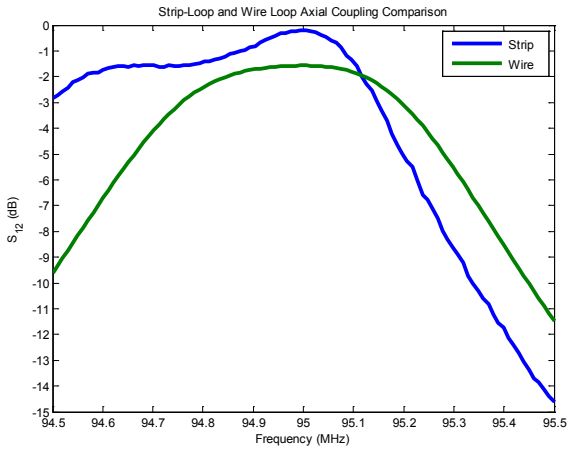


Figure 3-58 Comparison of Resonant Coupling between Wire and Strip Loop Optimized at 95MHz

The advantages of this structure are twofold. As observed in simulation, this structure couples more strongly than the wire loop model. This allows the user to transfer energy at longer distances. The

degradation of the strength of coupling with variation in radially directed distance can be seen in Figure 3-60.

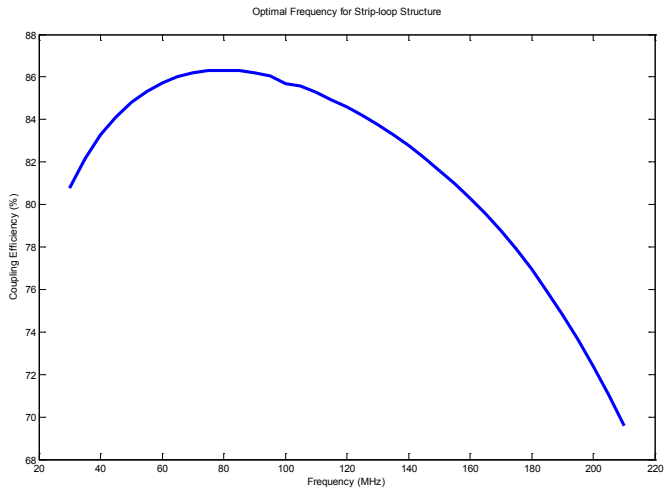


Figure 3-59 Strip Loop Optimal Frequency Analysis

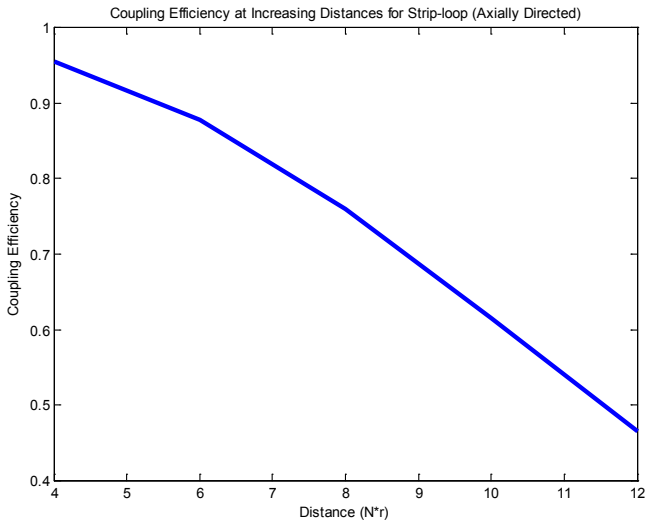


Figure 3-60 Distance Coupling Degradation for Strip-Loop Structure

The second advantage to this method is the requirement of this structure's resonant networks to store magnetic energy. The structure itself acts as a stronger inductor than the wire structures, as thus alleviates the larger inductance values required for the series resonant circuit networks. Table 3-11 compares the final optimized values for both the strip loop structure and the wire structure.

Table 3-11 Element Value Comparison for Wire and Strip Structures

| | $L_{transmitter}$ | $C_{transmitter}$ | $L_{receiver}$ | $C_{receiver}$ |
|---|---|---|---|---|
| Wire | 1618.21nH | 23.3844pF | 1358.25nH | 33.7561pF |
| Strip | 913.07nH | 66.9399pF | 961.31nH | 49.8075pF |

The benefits to this will become more clear when describing the prototype, and how coils must be built in order to ensure low-loss characteristics.

As with the other structures, the results from optimization were validated in the full wave simulator, and the resulting fields were displayed using a 3D shaded plot. The following figures are Poynting vector fields for the x, y, and z directed cases respectively.

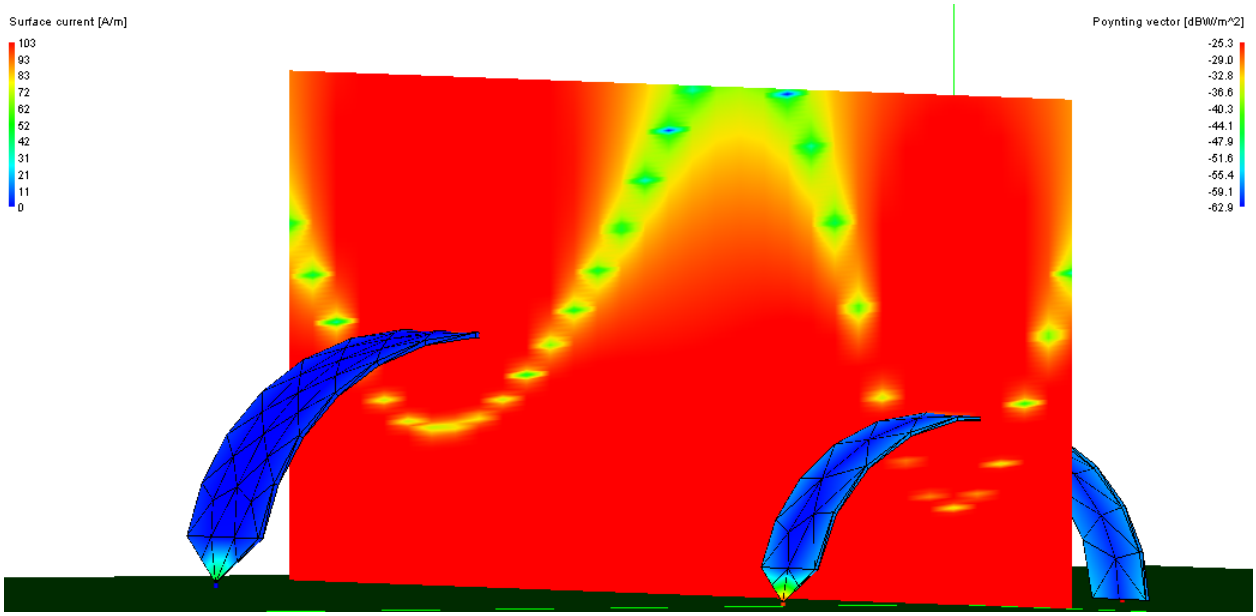

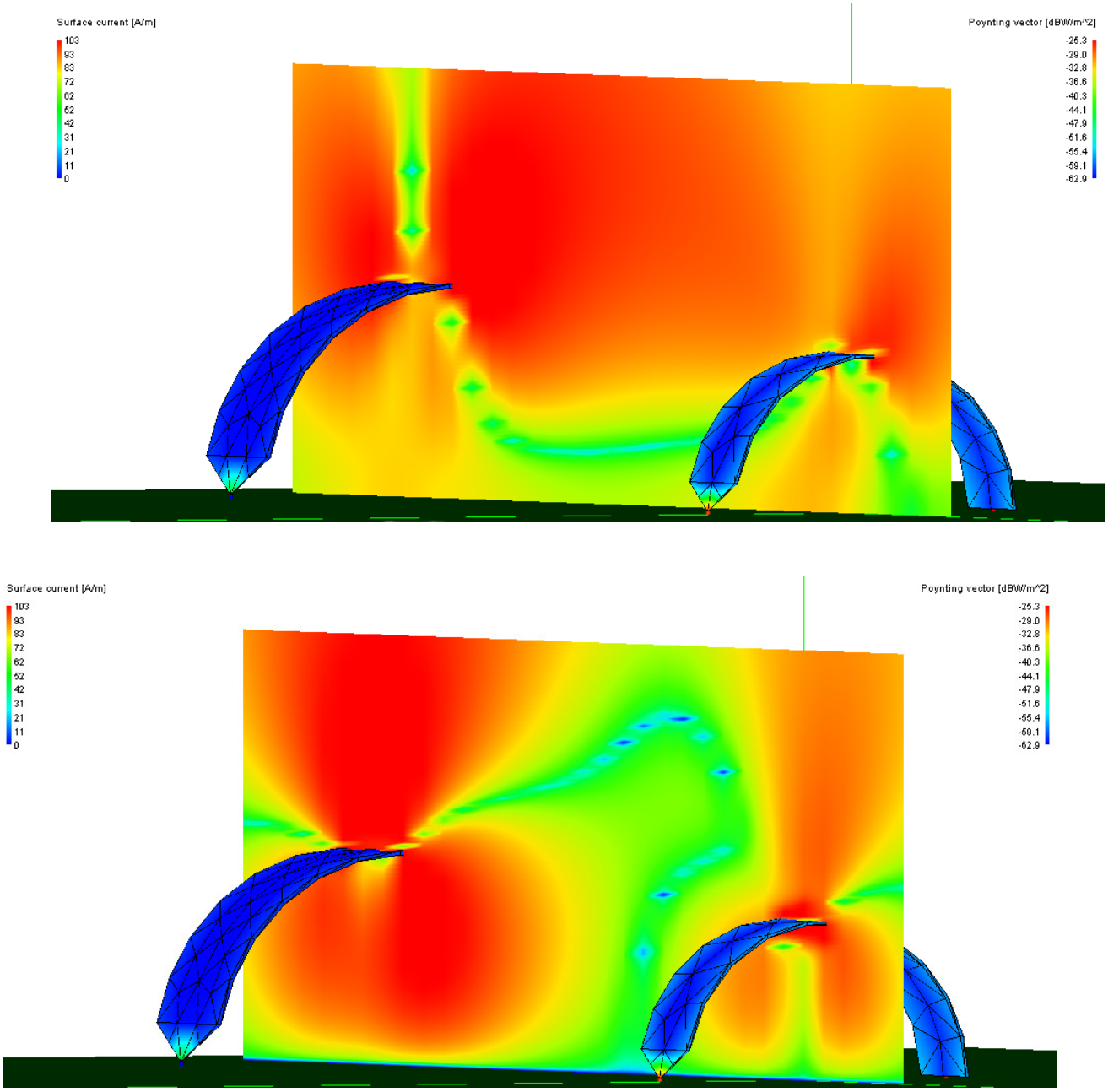


Figure 3-61 Field/Current Variations Strip Loop Case
Top: X-Directed Poynting Vector
Middle (top): Y-Directed Poynting Vector
Bottom: Z-Directed Poynting Vector

For all cases the shading that can be observed on the structure itself is a measure of the surface current on each of the mesh triangles, whereas the colored portion on the planar slice refers to the magnitude of

$$\frac{1}{2}Re\{\bar{E} \times \bar{H}^*\}$$

The legend for each magnitude can be found in the upper corners of each figure.

## 3.5 Removal of Ground Plane

In order to address practical implementation of these structures, removing an infinite ground plane must be considered. This consideration refers to the case that the ground plane of the Earth will not suffice for proper imaging. The methodology behind the removal of the ground plane is simple. The structure is symmetrically copied about its axis of rotation, and the re-optimized using the same resonant networks as the imaged case. In the case of the imaged half-loop dipole structure, the adjustment is to create full loops with a balanced excitation. The result of this structure is illustrated in Figure 3-62.

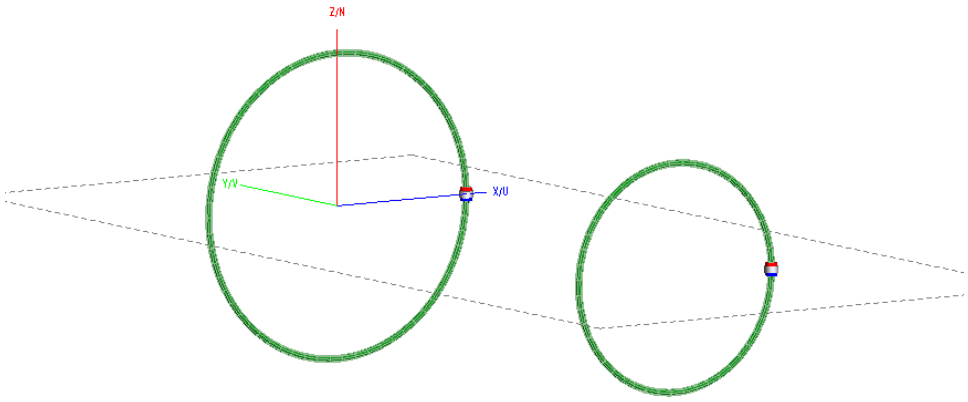


Figure 3-62 Full Loop Single Feed Structure in FEKO

This structure was similarly designed for the axially directed array, and this particular array can be observed in Figure 3-63.

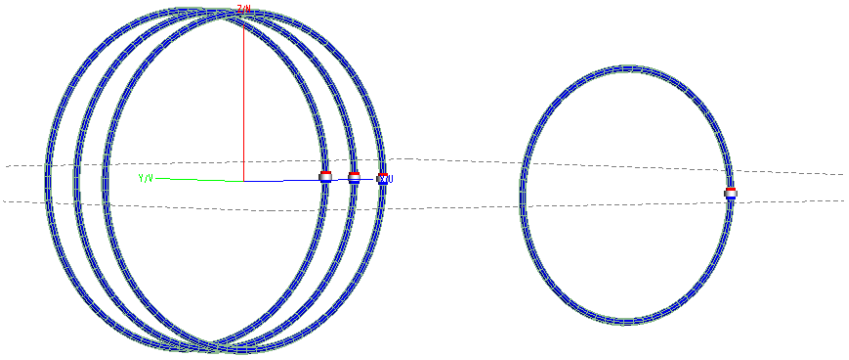

Figure 3-63 Full Loop Axially Directed Array in FEKO

The third structure under consideration is the strip loop. The strip loop was originally designed so that the point of the end of the stripline was connected to a wire that was then attached to the ground plane. This structure was then mirrored about the ground plane to give a double point, with a wire connecting the two points. A screen capture of this design in the FEKO window can be seen in Figure 3-64.

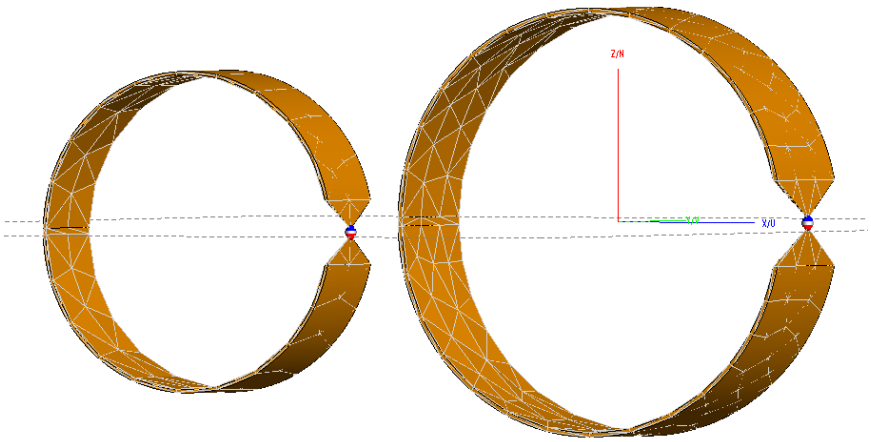

Figure 3-64 Full Loop Strip-Loop Structure in FEKO

The optimal frequency analysis for each of these structures is displayed in Figure 3-65.

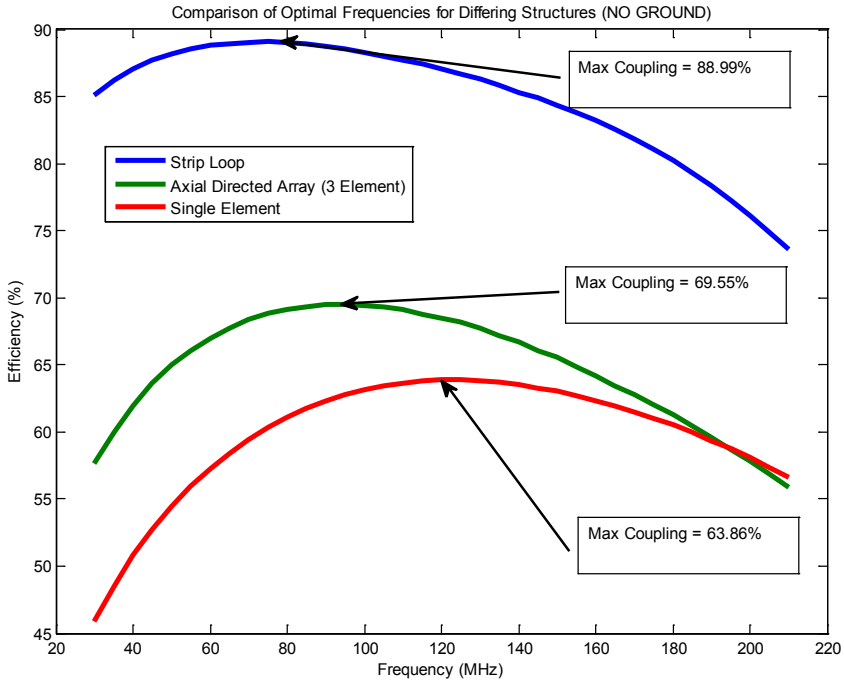


Figure 3-65 Comparison of Optimal Frequencies for all Full Loop Structures

It is important, as a note for implementation, to have knowledge of the reactance of the elements that will comprise the resonant network for each structure. Table 3-12 displays this data including optimal frequency, maximum coupling, and reactance values.

Table 3-12: Element Values for Various Optimal Frequencies

| | Frequency | $L_{transmitter}$ | $L_{receiver}$ | $C_{transmitter}$ | $C_{receiver}$ |
|---|---|---|---|---|---|
| Single Feed Wire | 125MHz | 1918.31nH | 1707.64nH | 6.90176pF | 9.9442pF |
| Three Element Axial Array | 90MHz | 1688.13nH | 1747.62nH | 24.836pF | 19.381pF |
| Stripline Loop | 80MHz | 1414.43nH | 1374.12nH | 33.3736pF | 44.2298pF |

The field validation for these structures was organized in the same manner as the original imaged structures. The unit directed fields for each of the structures can be seen in the figures below.

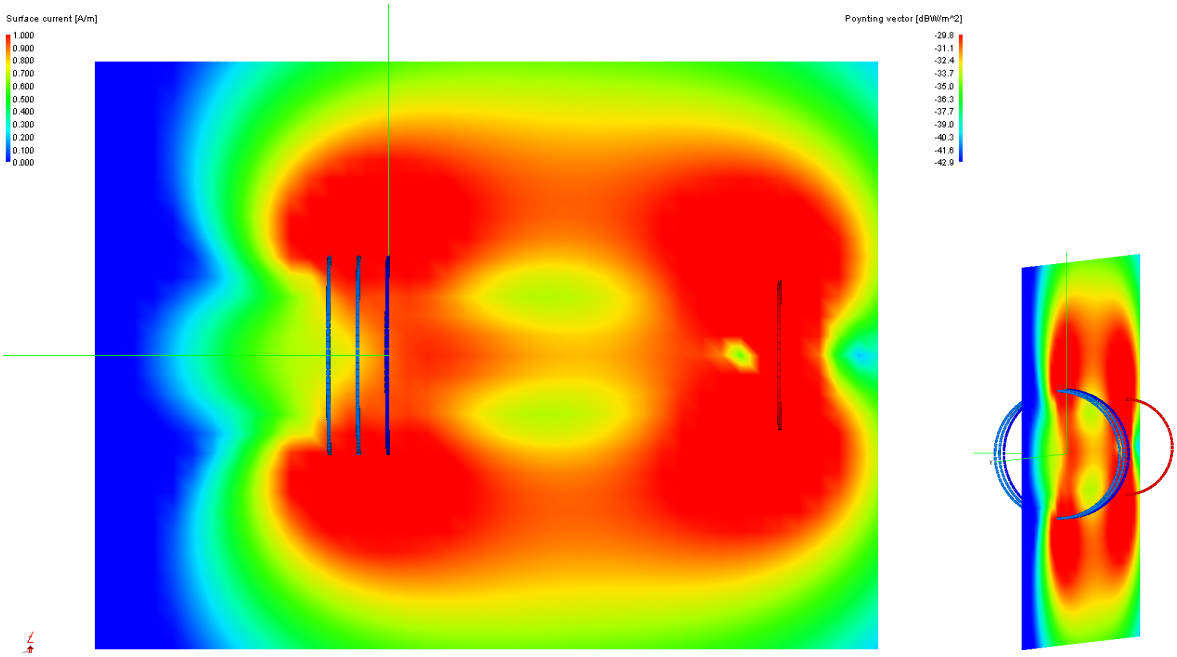
Surface current [A/m]
1.000
0.900
0.800
0.700
0.600
0.500
0.400
0.300
0.200
0.100
0.000
Poynting vector [dBW/m^2]
-29.8
-31.1
-32.4
-33.7
-35.0
-36.3
-37.7
-39.0
-40.3
-41.6
-42.9

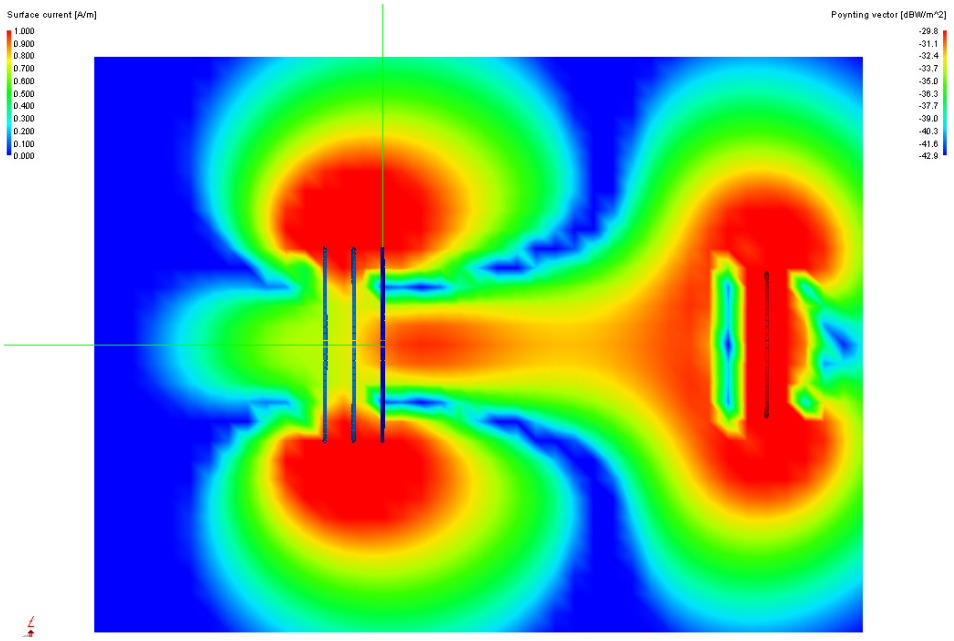
Surface current [A/m]
1.000
0.900
0.800
0.700
0.600
0.500
0.400
0.300
0.200
0.100
0.000
Poynting vector [dBW/m^2]
-29.8
-31.1
-32.4
-33.7
-35.0
-36.3
-37.7
-39.0
-40.3
-41.6
-42.9

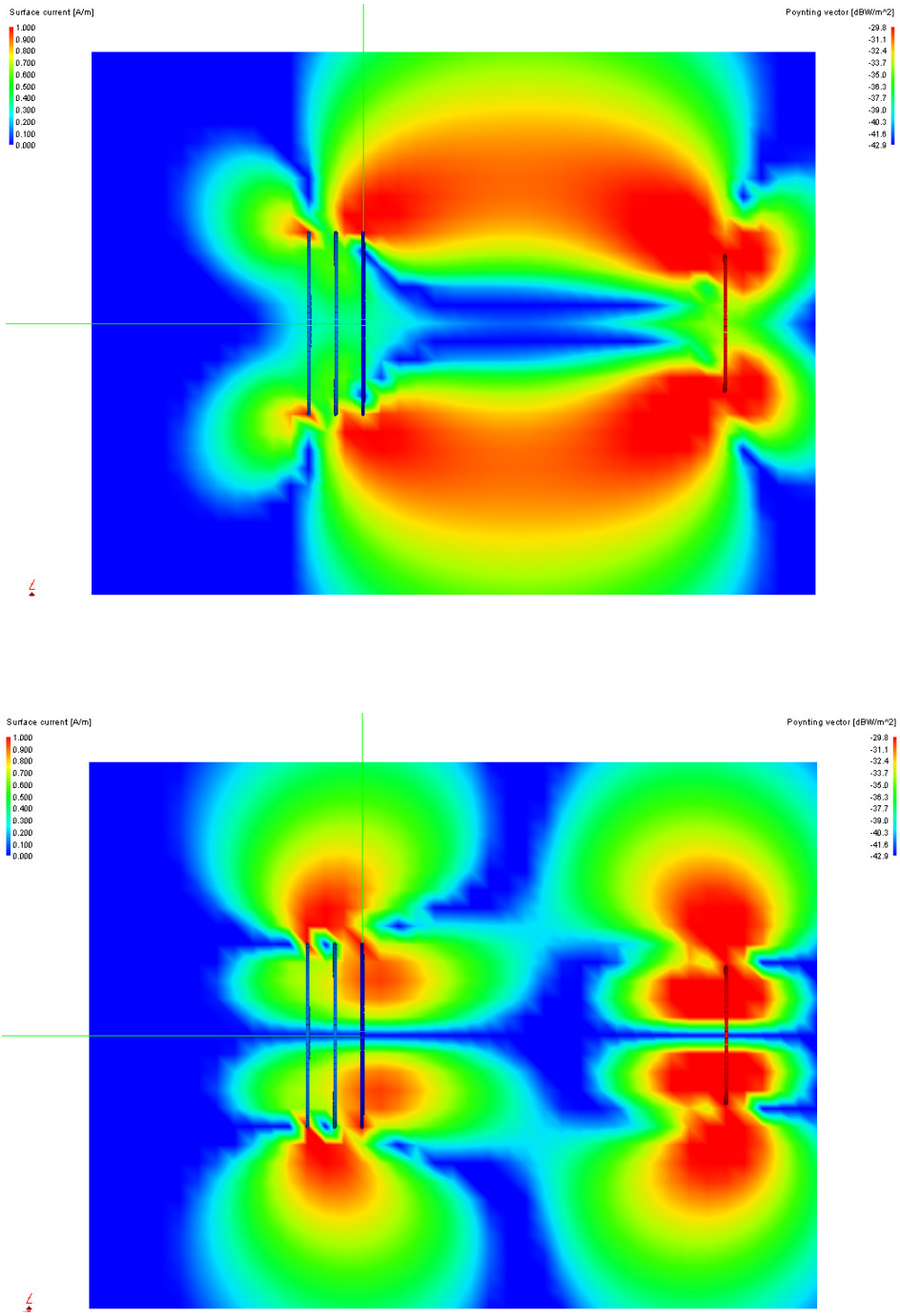


Figure 3-66 Field Variations Axially Directed Array Full Loop Case
Top: Total Poynting Vector
Middle (top): X-Directed Poynting Vector
Middle (bottom): Y-Directed Poynting Vector
Bottom: Z-Directed Poynting Vector

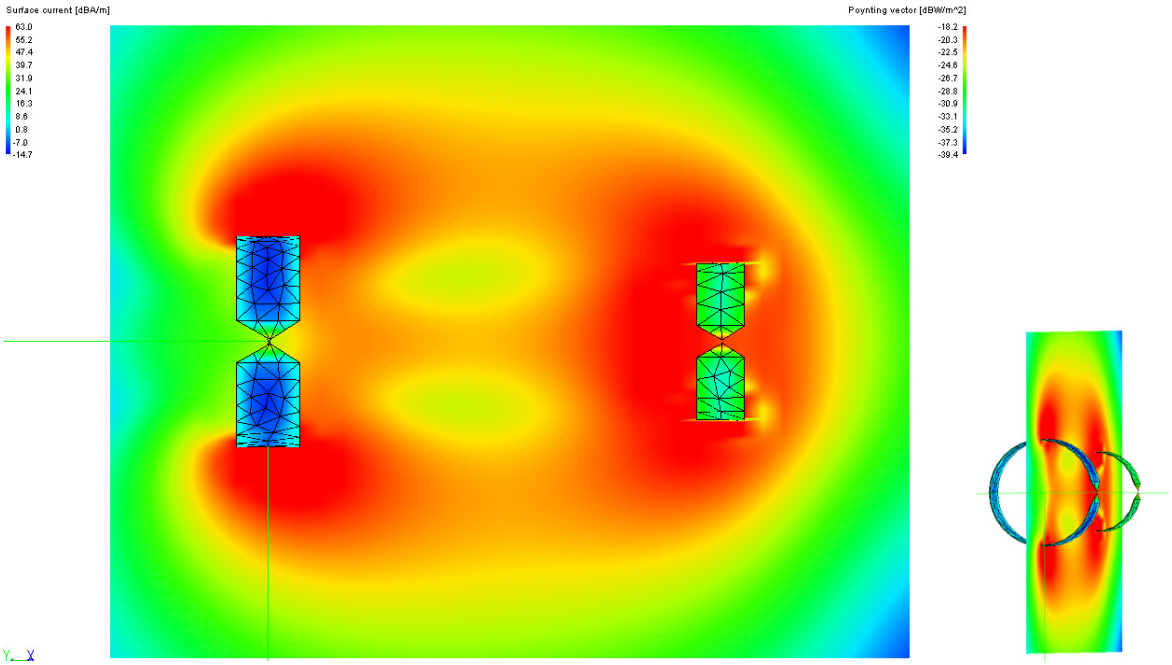
Surface current [dBA/m]
63.0
55.2
47.4
39.7
31.9
24.1
16.3
8.6
0.8
-7.0
-14.7
Poynting vector [dBW/m^2]
-18.2
-20.3
-22.5
-24.6
-26.7
-28.8
-30.9
-33.1
-35.2
-37.3
-39.4

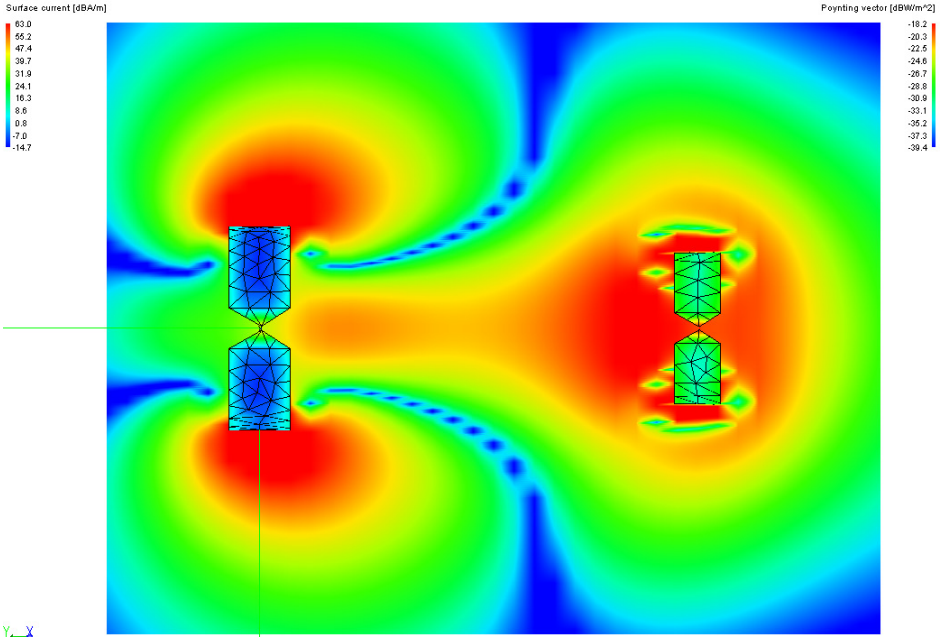
Surface current [dBA/m]
63.0
55.2
47.4
39.7
31.9
24.1
16.3
8.6
0.8
-7.0
-14.7
Poynting vector [dBW/m^2]
-18.2
-20.3
-22.5
-24.6
-26.7
-28.8
-30.9
-33.1
-35.2
-37.3
-39.4

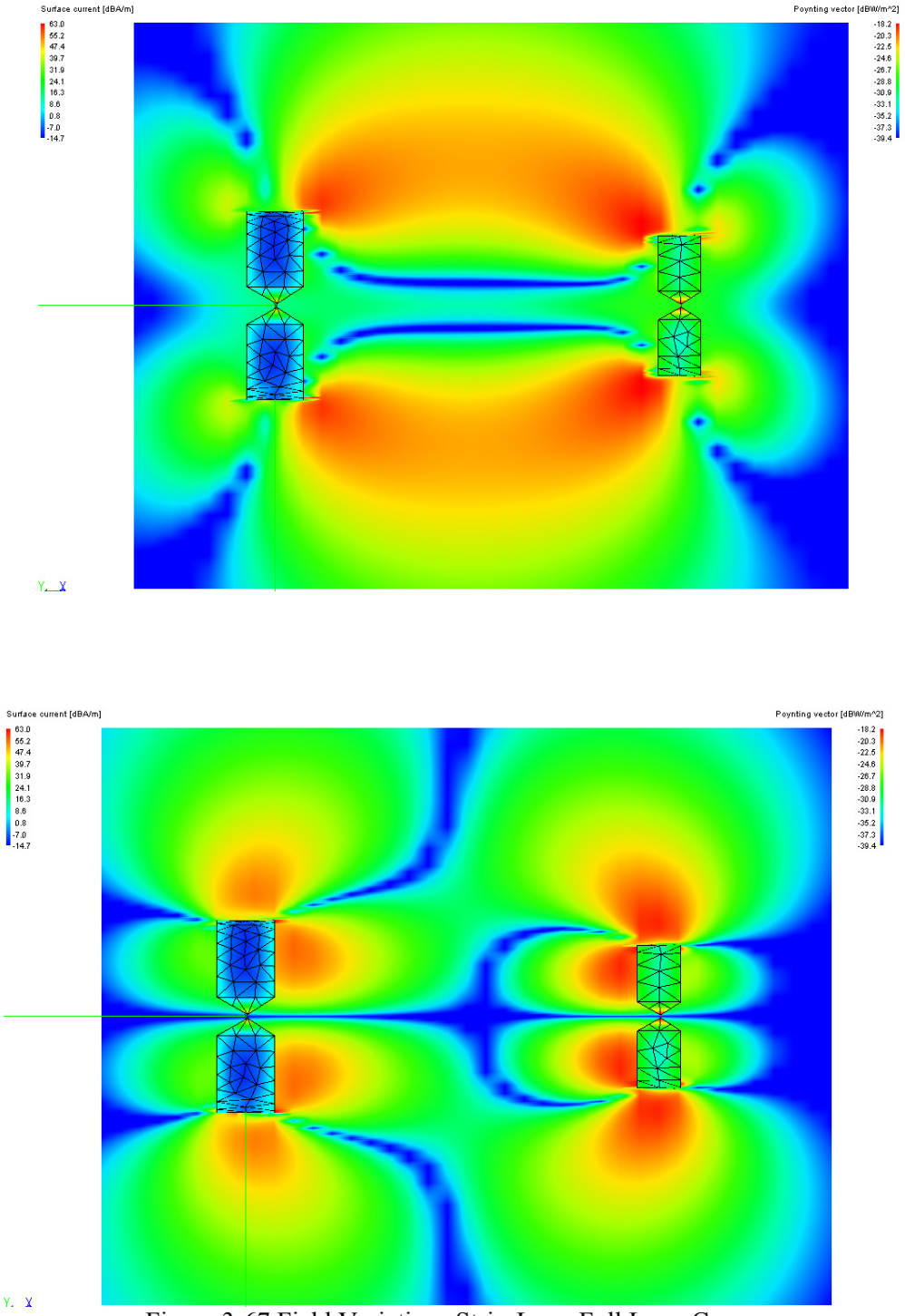


Figure 3-67 Field Variations Strip-Loop Full Loop Case
Top: Total Poynting Vector
Middle (top): X-Directed Poynting Vector
Middle (bottom): Y-Directed Poynting Vector
Bottom: Z-Directed Poynting Vector

# Chapter 4: Prototyping Results

The implementation of these networks into a prototype required careful design and consideration for many spurious effects of surroundings. All efforts were directed at reducing the loss in the networks, in order to achieve the large Q values expected from simulating lossless elements. This chapter will describe the process of construction, and results measured from the near field coupling prototype.

## 4.1 Ground Plane/Connector Assembly

The ground plane was required to have a surface that easily bonds with solder flux in order to solder any sort of SMA connector or coupling device to it. It was concluded that brass, instead of copper, would provide a surface that would strengthen the solder connects between all devices. A 2ft by 4ft sheet of brass, with a thickness of 1mm. The metallic sheet can be seen in Figure 4-69. In order to ensure that this planar thickness is applicable for the frequencies under consideration, the skin depth for the minimum frequency must be calculated. Skin depth, or the depth above which surface current flows in the conductor. The skin depth can be mathematically defined by

$$\delta = \sqrt{\frac{2}{\omega\mu\sigma}}$$

where $\sigma$ is the conductivity of the metal. For brass it is known that $\sigma = 2.56 * 10^7 \frac{S}{m}$. The skin depth of

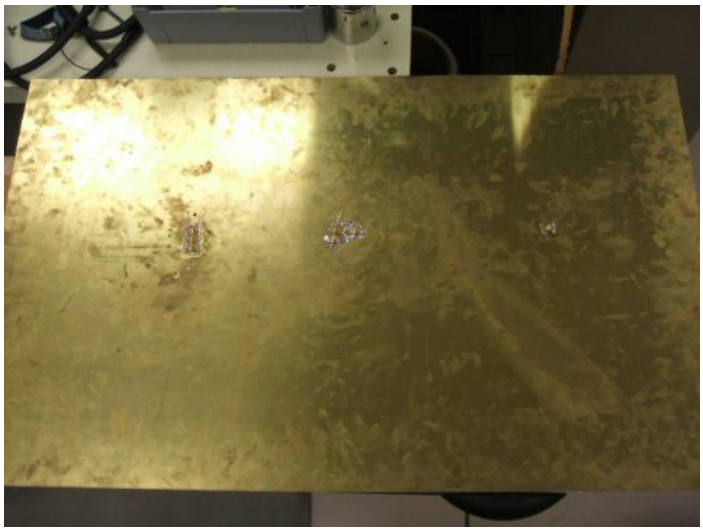

Figure 4-68 Brass Ground Plane with SMA Connections

copper is, at 10MHz maximum, is $3.1 * 10^{-5}m$ which is well within the thickness of the sheet. Connections on the ground plane were made in two areas. On one side of the plane there is a connection for the resonant networks, and this takes the form of an SMA 3.5mm connection. An approximate 3mm diameter hole was drilled at different points in the sheet corresponding to different distances between transmitter and receiver. The distances were 200mm, 300mm, and 500mm from the original transmitter placement. The hole for the SMA connector was constructed to be wide enough for the dielectric to fit through the sheet and become visible on the opposite side. The additional space insured that the coupling structure soldered to the tip of the SMA pin would have additional room between it and ground to avoid shorting the element. Once the connectors were fit through the holes, the ground plane of the SMA was soldered onto the ground plane. Figure 4-70 illustrates three SMA connectors soldered to the ground plane (this arrangement would eventually be used for the three element axially directed array). Each element was placed apart with a distance determined by the width of the SMA connector individual grounds. This distance was 13mm, and was a nominal spacing reflected in simulation and numerical analysis. This is the extent of connections on the network side of the ground plane. On the opposite side the SMA pins were soldered to the various structures that were under test (either a wire or strip loop). As in simulation, a side of the element was soldered to the pin while the other end of the half-loop structure was soldered directly onto the ground plane. This maneuver required the user to heat the brass sheet in the area of soldering considerably before attempting to lead the solder onto the element from the sheet for a strong connection. Figure 4-70 displays the coupler structure side of the metallic sheet for the various structures under consideration.

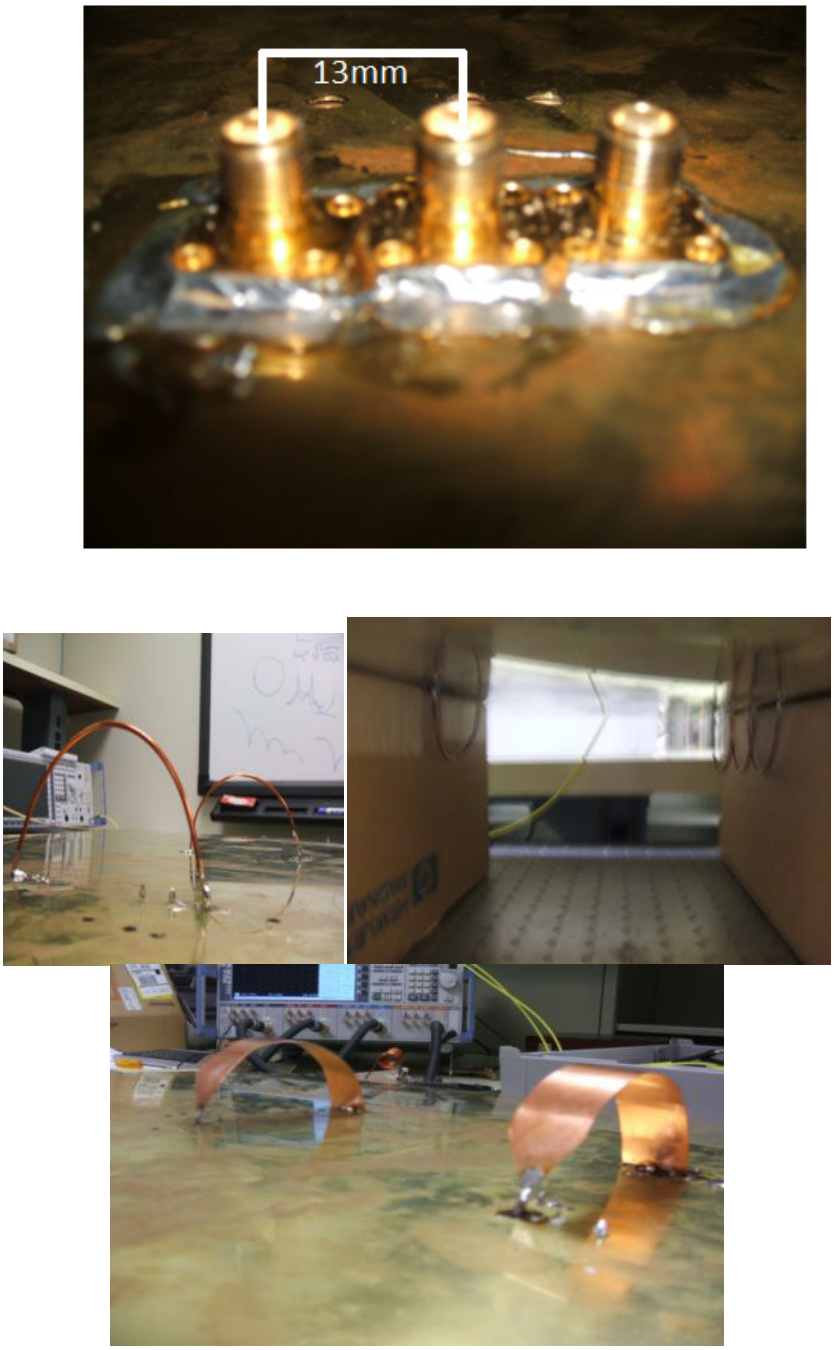


Figure 4-69 SMA Connection Separation and Prototype Structural Variations

## 4.2 Resonant Network Assembly

The resonant networks under prototyping will be modeled by a simple RLC tank circuit, where R is described as any loss mechanism in the circuit (no physical resistors were used). To understand an idea of the complexity of the loss within the circuit, observe Figure 2-21 in Section 2.4. These networks are connected to the elements via the 3.5mm threaded female SMA connection on the "underside" of the brass metallic ground plane.

The resonant network is built upon an FR4 dielectric board. The underside of the board is a copper sheet and will provide the ground for the network. The connection port of the resonant network (opposite the excitation port) was tightly fastened to a male to male barrel connector in order to give the board, in which the resonant network was placed, a small offset above the ground plane for tuning purposes. This distance allows for connections to be made under the FR4 board and above the brass ground plane. The excitation port utilized a $90^{o}$ male to male 3.5mm SMA connector in order to create an easier connection for VNA cables.

### 4.2.1 Variable Capacitor

The primary method of tuning the networks was the variable shunt capacitor placed in series with coupling element. These capacitors ranged from 2-22pF in product specifications. They are designed as plate capacitors that adjust the amount of surface area between two plates as the plates are slid across each other. This design leads to a somewhat linear (should be $2^{nd}$ order given area) capacitance to turn ratio. Figure 4-71 shows the two different variable capacitors used for prototyping of the resonant networks. Both of the variable capacitors are tuned using a flathead adjustment on the center column of rotation. This tuning screwdriver must have a dielectric tip in order to negate the effects of the electrical length of the screwdriver on the overall performance of the network. It is imperative that the center rotational column is placed on the ground side of the shunt capacitor or the effect of tuning the capacitor, regardless of flathead type, will affect the coupling of the network.

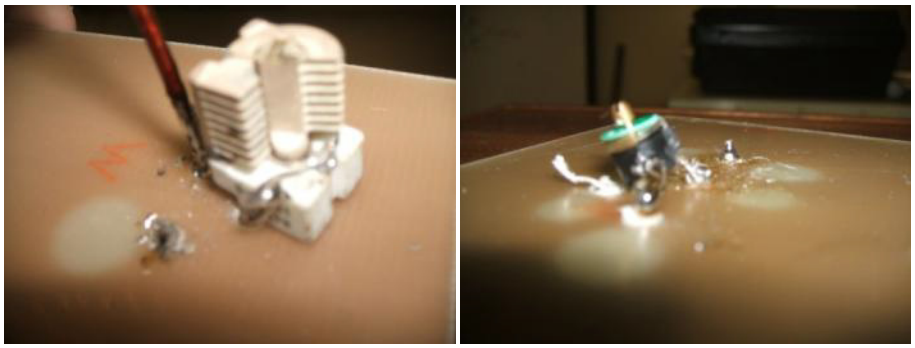

Figure 4-70 Comparison of Variable Capacitors

### 4.2.2 Inductor Design and Implementation

The primary method for storing magnetic energy in the circuit was the series inductor. As with all elements in this design, the minimization of loss was an important factor in determining the overall Q of the network. There are a variety of structural inductor designs that can be implemented for the frequency range under prototype testing. Since the primary objective of this element is to provide an inductive reactance without loss, an air core inductor was used. Ferromagnetic and dielectric core inductors tend to show higher loss characteristics. Furthermore, any magnetic core material will saturate with a strong applied *B* field and would thus be inappropriate for any high power applications.

There are several different structural types of air core inductors. These "types" are organized according to the geometry in which the conductor is shaped. "Coil" inductors are structures in which the wire is curved around a central axis of rotation, in a pattern similar to a helix. These air-core coil inductors can take a variety of forms, such as toroidal, helical, and circular. Toroidal inductors have a circular axis of rotation, and are typically used in conjunction with a core material. The helical and circular coil inductors have a linear axis of rotation, and are generally used for inductive coupling purposes. For prototyping purposes, the toroidal inductor was not considered in the design process given its typical uses, and difficulty of construction. Both the helical and circular inductors were designed and tested in the prototype resonant networks. A third variety of inductor was also used for the prototype resonant networks: the spiral inductor. The gap capacitance for the spiral inductor is highly reduced given the proximity of the conducting wire loops to each other, with reference to a helical or circular inductor. The Archimedean spiral was used as it gives a linear spacing between adjacent loops.

Each of the inductors' loss characteristics were tested by soldering each end of the inductor to two ports on the FR4 test board. Figure 4-72 shows examples of how each of these appeared during testing.

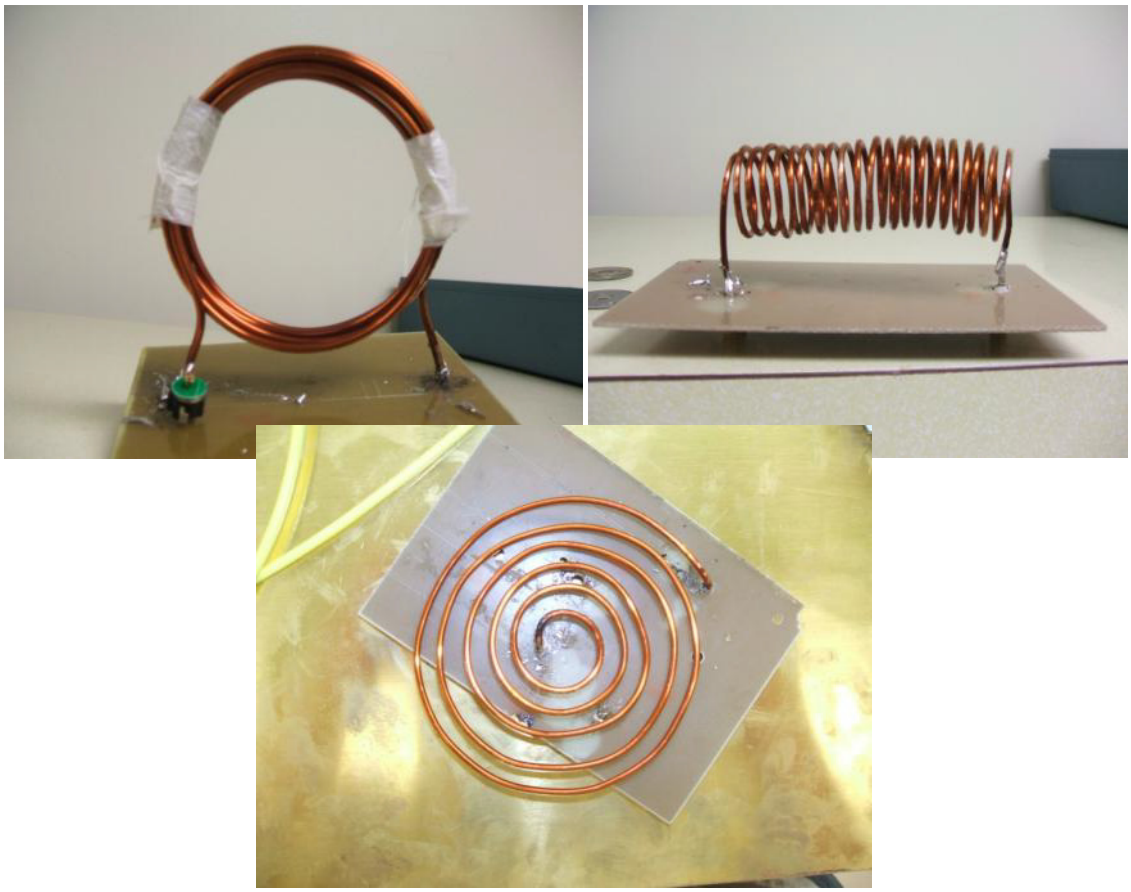

Figure 4-71 Coil Inductor Variations

All of the aforementioned coils were tested for loss characteristics. This was observed by measuring the $S_{12}$ for each of the inductors in series, and measuring the Q from the first harmonic. It is important to note that given the amount of wire required to make the inductors, the resonance of the inductor may have occurred within the frequency range under consideration (10-250MHz). This was undesirable considering an increase in radiation resistance would subsequently increase the loss in the network. Figure 4-73 shows a comparison of the three types of inductors and their $S_{12}$. In the figure "coil" refers to the helical coil while "compressed coil" refers to the circular coil. All inductors were created with the same length of wire (1.2*m*) in order to normalize the effect of the inductors' antenna properties.

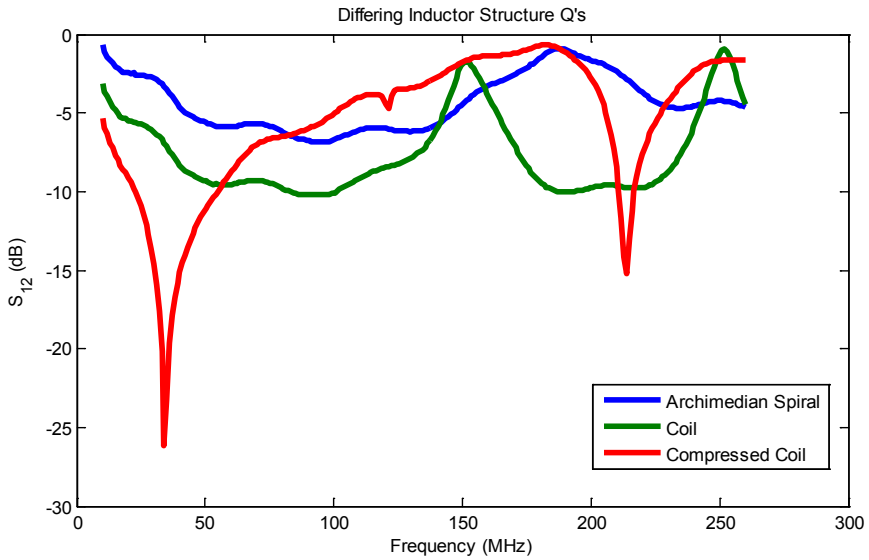


Figure 4-72 Comparison of $S_{12}$ for Differing Coils

From observing the reverse voltage gain of each of the structures it is apparent that the circular coil structure has a lower Q, with a capacitive characteristic over much of the HF/VHF range. The capacitive characteristic is most likely correlated to the distance between subsequent loops of the coil. For the circular case, these loops are touching each other (held together by dielectric tape). This is an undesirable characteristic as it leads to more loss in the network. The spiral and helical coils both had somewhat similar characteristics with the helical coil providing the highest Q, around 26. By this comparison it was determined that the helical coil was the optimal choice for to implement on the prototype.

## 4.3 Connections/Isolation/Tuning

The networks were directly connected to the coupling elements through the ground plane via a straight male to male 3.5mm SMA connector. These connectors were configured for multiple element arrays to align with each individual element's SMA connector so no stress was placed on adjacent connectors from bending or torsion of any kind. All connects were firmly tightened using a torque wrench intended for use with the VNA that was used for all measurements. Under these conditions the resonant networks were held firmly parallel with the ground plane approximately 3.5*cm* above the ground plane. Figure 4-74 displays the full networks connected for the 3 element axial directed array. This particular prototyping utilized the three inductors, as presented in Chapter 4. It can be seen that there is a brass sheet standing in the center of the two networks lying normal to the ground plane surface. This purpose of this sheet is to increase isolation between the network inductors. Figure 4-75 compares the coupling between this array and the simulated version of this array. As can be seen from the prototyping, there is a small amount of coupling that occurs around 150MHz, and a larger coupling that occurs just after 250MHz. These two

peaks are examples of the inductors in the resonant networks coupling rather than the coupling elements themselves coupling. The strongest peak, however, represents the resonant coupling between the elements and networks combined. For the axially directed array this occurred the strongest at 105.85MHz, around 10MHz higher than prediction in simulation. Figure 4-75 (right) shows an expansion of the frequency range around maximum coupling for the axially directed array.

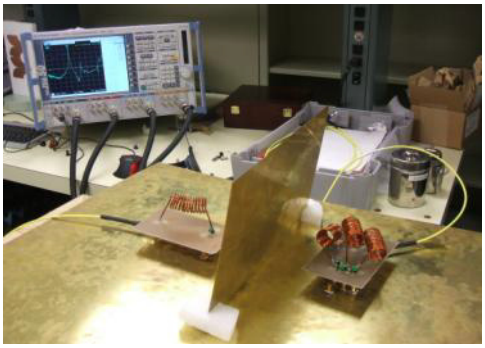

Figure 4-73 Full Setup for Resonant Tuning

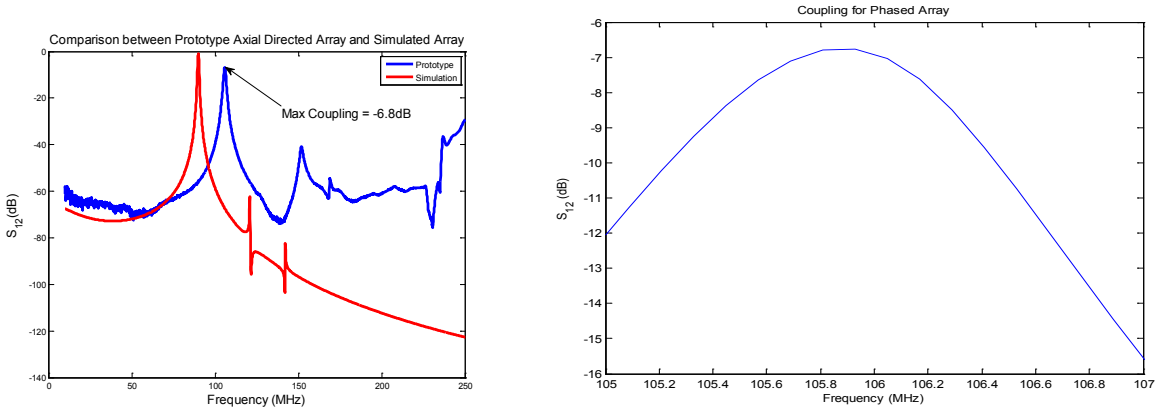


Figure 4-74 (left) Comparison between Simulation and Prototype for Axially Directed Array (3 Element) (right) Expanded View of Prototype Coupling under Resonance

This process was also duplicated for the single feed case, and for the strip-loop cases. Figure 4-76 compares the prototyping frequency sweep with that of the simulation for the single feed case.

This primary structure that was configured as the optimal candidate for maximum coupling was the strip-loop. In order to properly prototype this structure, the inductive coupling between the two loops must be similar, to provide integrity for the simulation to measurement. Figure 4-77 displays the inductive coupling between the prototype strip loop and the simulation. Figure 4-78 displays the resonant coupling comparison for the strip-loop structure. All of the array prototypes had relatively the same

maximum coupling between them. This result directly relates the efficiency of the network as a whole to the loss associated with each resonant network. It can be assumed that the load of resonant network (the coupler) has some Q value, called $Q_c$. It can also be assumed that the resonant network has an unloaded Q as well, which can be called $Q_r$. If the coupler is connected to the resonant network, the total Q, $Q_l$ is

$$\frac{1}{Q_l} = \frac{1}{Q_c} + \frac{1}{Q_r}$$

which results in the majority of the loss stemming from the resonant networks, if all prototype structures tend toward the same maximum coupling. This, in effect, taking into account the derivation for coupling, eliminates the ability to differentiate which structure/network combination forms the strongest coupling. Of course, by reducing the loss in the resonant network, the effects of the couplers will become more apparent, and thus the ability to test specific resonant structures would be available.

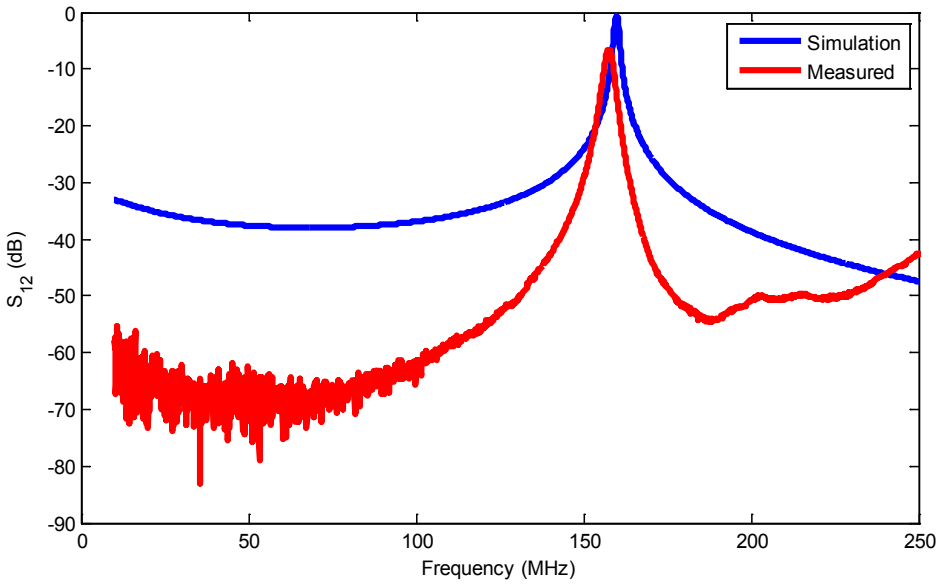


Figure 4-75 Comparison of Prototype and Simulation Coupling for the Single Feed Case

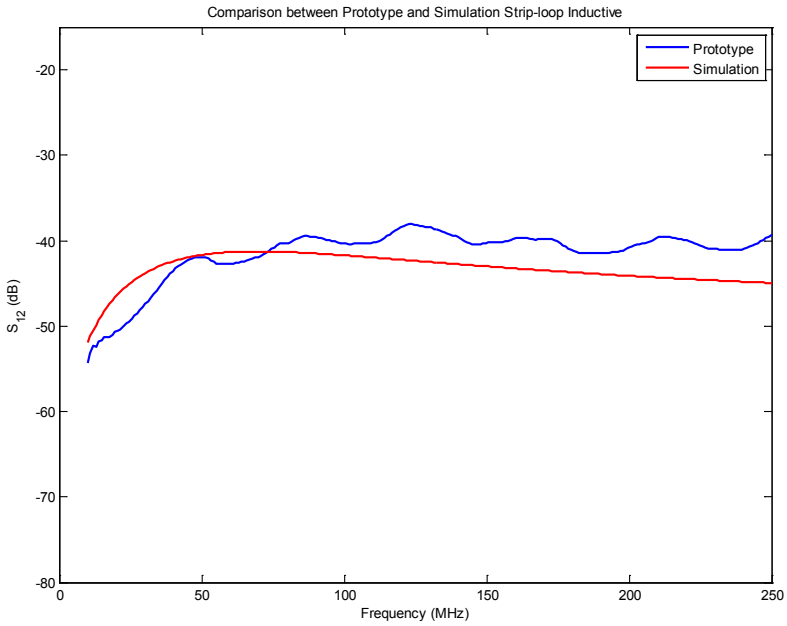


Figure 4-76 Inductive Coupling Comparison between Prototype and Simulation for Strip-Loop Structure

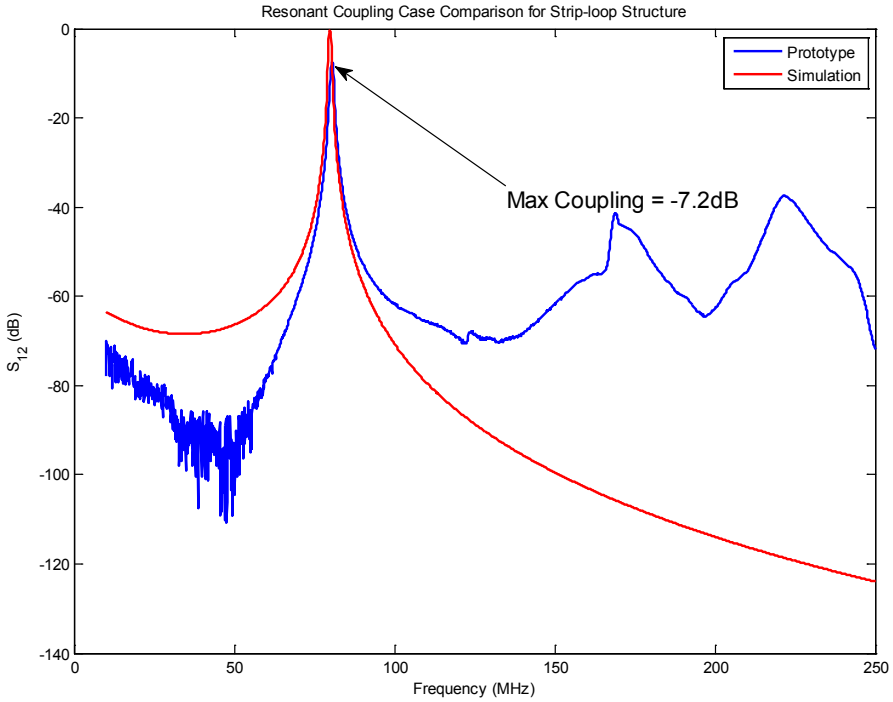


Figure 4-77 Comparison of Prototype and Simulation Coupling for the Strip-Loop Structure

# Chapter 5: Discussion of Results and Conclusion

Results are summarized as to clarify conclusions to the original motivations for the research. The following section serves as reference for what has been presented in this paper, and the possibilities for future investigations in the area of magnetic resonant coupling.

## 5.1 Numerical Results

A fully developed hybrid EM Full Wave/Circuit Simulation optimization process was developed and validated. The primary structural variations used were the: single feed loop, axially directed array of loops, and the strip-loop. The original design under test was the axially directed phased array. As the elements of the array converged inward (closer to each other) it was observed that the coupling between the entire array and the receiving element also increased. It was by this observation that the strip-loop structure was tested, as a structure that would implement this element convergence into a single structure. As was expected, there was a noticeable increase in efficiency at mid-ranges, and also a noticeable decrease in the degradation of coupling at longer distances. Table 5-13 summarizes the maximum coupling that was achieved for the lossless resonant network case between the differing structures. This results display the coupling strength limit to these specific structures at the distances under question.

As was also analyzed, the azimuthal displacement of the transmitting coupler also led to degradation of coupling strength. In the more extreme displacements, such as $\pm\frac{\pi}{2}$, the efficiency of coupling diminished to zero. This displacement phenomenon presents the limitations to tracking a receiver in azimuth.

Table 5-13: Summary Table of Maximum Coupling for Varying Structures

| Structure | Distance, *d* | Optimized Frequency | Coupling Efficiency |
|---|---|---|---|
| Single Feed Loop | 200mm | 125MHz | 64.41% |
| 3 Element Axially Directed Array | 200mm | 90MHz | 69.99% |
| 5 Element Axially Directed Array | 200mm | 90MHz | 71.14% |
| Strip Loop Single | 200mm | 80MHz | 86.32% |

Table 5-14:Summary Table of Maximum Coupling For Varying Structures Full Loop Cases

| Structure | Distance, *d* | Optimized Frequency | Coupling Efficiency |
|---|---|---|---|
| Single Feed Loop | 200mm | 125MHz | 63.87% |
| 3 Element Axially Directed Array | 200mm | 90MHz | 69.55% |
| Strip loop | 200mm | 80MHz | 88.99% |

The total numerical results show the possibility of increasing the strength of coupling by using a ring strip coupler. This was determined as a suitable structure when the axial directed elements were converged in a center point 200mm away from the receiver. As the elements converged, the strength of the coupling increased. The same $S_{12}$ increase occurred when the amount of elements in the array was increased. It was then conjectured that a continuous structure such as a strip of wire would combine these effects. The results were in alignment with the conjecture for simulation purposes.

## 5.2 Prototyping Results

Results from prototyping were met with a weaker coupling efficiency for a variety of reasons. The primary cause for the reduction in energy transfer was the loss present in the system. In Section 2.4, the effect of loss on a resonant network passband was discussed. The loss in the network can be effectively expressed as a parallel impedance with the entire network:

$$\frac{1}{Q_l} = \frac{1}{Q_c} + \frac{1}{Q_r}$$

The maximum coupling from each of the structures is displayed in Table 5-15. The general result from prototype is that, since the coupling from all of the structures seems to be relatively similar (18-22%), the primary factor in the loss of the networks must be networks, as the structures had little loss associated with them. Due to this characteristic limitation of the networks, a prudent topic for future discussion would be high Q inductive coil construction and high Q capacitor construction. As the majority of the reactance in the circuit is inductive, the high Q coil is of utmost importance, especially with the limitations on length as described in Chapter 4.

Table 5-15: Summary of Maximum Coupling for Prototype Structures

| Structure | Distance, *d* | Coupled Frequency | Coupling Efficiency |
|---|---|---|---|
| Single Feed | 200mm | 155MHz | -6.5dB → 22.39% |
| Axially Directed Array (3 element) | 200mm | 110MHz | -6.8dB → 20.89% |
| Strip-loop | 200mm | 80MHz | -7.2dB → 19.05% |

## 5.3 Future Investigations

The majority of the investigations within the scope of this project have focused primarily on increasing the strength of coupling between two conducting structures. In order to continue this lead, it is prudent to continue testing various types of couplers, and analyzing the characteristic advantages/disadvantages of each. Of course, as evident from previous work in the area of magnetic resonance, coils are a prevalent choice for couplers. In order to successfully implement the coil coupler however, there must be an extensive EM validation process, in that the coil structure complicates electromagnetic interactions (there are more interactions, coupling, and scattering). Figure 5-79 shows a possible loosely coupled concentric coil array that can be implemented for coupling purposes.

As discussed in the previous section a limiting characteristic of the networks is the loss of the inductor. In order to progress further with analyzing differing structures for coupling, the issue of loss through the resonant networks must be addressed. There are a variety of possibilities for high Q inductors however, what must be explored is how to implement these designs within the HF and VHF regime. Material properties of the inductor and the geometry of the coil, toroid, or solenoid take a role in the loss that is apparent through the device. Also, a future priority for this research is to implement for high power, and thus linearity within the inductor is a must. This effectively eliminates all inductors that use a

magnetic or dielectric core. Once a proper reactive element is developed for the frequency range under question, a clearer understanding of the effects of the coupler will become possible.

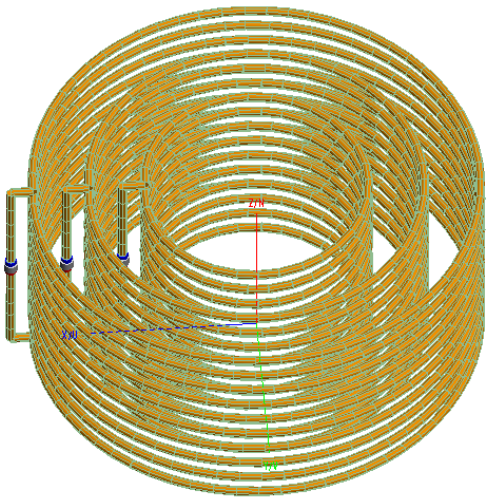

Figure 5-78 Concentric Helical Array for Consideration

Immediate investigations to this topic include scaling and removal of the ground plane for testing. These changes are strictly to show the possibility of practical implementation, as the availability of a ground plane between coupling elements is not practical or realistic. All simulations have been tested for a balanced input to the couplers (see Section 3.5) and it can be seen that the results do not vary from the imaged case. Of course, there are engineering limitations on the ability to create a balun or choke to feed the networks, and this must be investigated to implement properly. The practicality of a full loop for coupling relies in its versatility and size. Regarding size, the ability to scale the prototype also exists. When the entire network is scaled, including the structure and element values, the distance that coupling can occur between transmitter and receiver also scales. This allows for a greater range for coupling, and will be used to apply these designs for large scale implementation (charging vehicles, robots, mobile devices) to smaller and even nanoscale applications (biomedical implant powering, RFID energy harvesting).

Future investigations on the topic of magnetic resonant coupling are essential for the development of a reliable system for transmitting energy wirelessly.

# References


[1] Hertz Heinrich [Rudolph] 1857-1894. [from old catalog] and D. E. Jones, *Electric waves; being researches on the propagation of electric action with finite velocity through space*. London,: and New York, Macmillan and co., 1893.

[2] N. Tesla, "Patent 1119732: Apparatus for Transmitting Electrical Energy," *US Patent Office,* 1902.

[3] N. Tesla, "On Electrical Resonance (Reprinted)," *M D Computing,* vol. 12, pp. 137-140, Mar-Apr 1995.

[4] J. A. Ewing, *Magnetic induction in iron and other metals*, 3d ed. New York,: The D. Van Nostrand company; etc., 1900.

[5] U. Gianola, "Application of the Wiedmann Effect to the Magnetostrictive Coupling of Crossed Coils," *Journal of Applied Physics,* vol. 26, pp. 1152-1157, Sept. 1955 1955.

[6] R. R. A. Syms and L. Solymar, "Magneto-inductive cable arrays: Estimation and reduction of crosstalk," *Journal of Applied Physics,* vol. 109, pp. -, Feb 15 2011.

[7] B. J. K. G. K. LaMeres, S.P., "Controlling inductive cross-talk and power in off-chip buses using CODECs," *Design Automation, 2006. Asia and South Pacific Conference on,* 2006.

[8] D. Mizoguchi, N. Miura, Y. Yoshida, N. Yamagishi, and T. Kuroda, "Measurement of inductive coupling in wireless superconnect," *Japanese Journal of Applied Physics Part 1-Regular Papers Brief Communications & Review Papers,* vol. 45, pp. 3286-3289, Apr 2006.

[9] A. Shadowitz, *The electromagnetic field*. New York,: McGraw-Hill, 1975.

[10] B. L. Cannon, J. F. Hoburg, D. D. Stancil, and S. C. Goldstein, "Magnetic Resonant Coupling As a Potential Means for Wireless Power Transfer to Multiple Small Receivers," *Ieee Transactions on Power Electronics,* vol. 24, pp. 1819-1825, Jul 2009.

[11] W. Guoxing, L. Wentai, M. Sivaprakasam, M. S. Humayun, and J. D. Weiland, "Power supply topologies for biphasic stimulation in inductively powered implants," in *Circuits and Systems, 2005. ISCAS 2005. IEEE International Symposium on*, 2005, pp. 2743-2746 Vol. 3.

[12] J. Bing, J. R. Smith, M. Philipose, S. Roy, K. Sundara-Rajan, and A. V. Mamishev, "Energy Scavenging for Inductively Coupled Passive RFID Systems," in *Instrumentation and Measurement Technology Conference, 2005. IMTC 2005. Proceedings of the IEEE*, 2005, pp. 984-989.

[13] A. Kurs, A. Karalis, R. Moffatt, J. D. Joannopoulos, P. Fisher, and M. Soljacic, "Wireless power transfer via strongly coupled magnetic resonances," *Science,* vol. 317, pp. 83-86, Jul 6 2007.

[14] A. Karalis, J. D. Joannopoulos, and M. Soljacic, "Efficient wireless non-radiative mid-range energy transfer," *Annals of Physics,* vol. 323, pp. 34-48, Jan 2008.

[15] H. A. Haus and W. P. Huang, "Coupled-Mode Theory," *Proceedings of the Ieee,* vol. 79, pp. 1505-1518, Oct 1991.

[16] H. A. Haus, *Waves and fields in optoelectronics*. Englewood Cliffs, NJ: Prentice-Hall, 1984.

[17] A. Kumar, S. Mirabbasi, and C. Mu, "Resonance-based wireless power delivery for implantable devices," in *Biomedical Circuits and Systems Conference, 2009. BioCAS 2009. IEEE*, 2009, pp. 25-28.

[18] L. Rindorf, L. Lading, and O. Breinbjerg, "Resonantly coupled antennas for passive sensors," in *Sensors, 2008 IEEE*, 2008, pp. 1611-1614.

[19] A. K. RamRakhyani, S. Mirabbasi, and C. Mu, "Design and Optimization of Resonance-Based Efficient Wireless Power Delivery Systems for Biomedical Implants," *Biomedical Circuits and Systems, IEEE Transactions on,* vol. 5, pp. 48-63, 2011.

# Appendix A: Ancillary Figures and Derivations

The derivation as described in chapter 1 by:

$$Z_{in} = \left\{\{\{L_1, C_1\} + Z_{11} - Z_{12}, Z_{12}\} + Z_{22} - Z_{12}, C_2\right\} + L_2$$

when fully expanded looks like:

$$-\left(i\left(-Z_{12}^2 + Z_{11}Z_{22} + L_2\omega\left(C_2\omega Z_{12}^2 + Z_{11}(i - C_2\omega Z_{22})\right) + L_1\omega\left(iZ_{22} + C_1\omega(Z_{12}^2 - Z_{11}Z_{22}) + L_2\omega(-1 - iC_2\omega Z_{22} + C_1\omega(-iZ_{11} - C_2\omega Z_{12}^2 + C_2\omega Z_{11}Z_{22}))\right)\right)\right)$$
$$-C_2\omega Z_{12}^2 + Z_{11}(i - C_2\omega Z_{22}) + L_1\omega\left(1 + iC_2\omega Z_{22} + C_1\omega(iZ_{11} + C_2\omega Z_{12}^2 - C_2\omega Z_{11}Z_{22})\right)$$

The following figures are from the strip loop structural modification, with a finer mesh on the receiver. The figures show the field values, and the variance in surface current (in dBA/m) due to the finer mesh.

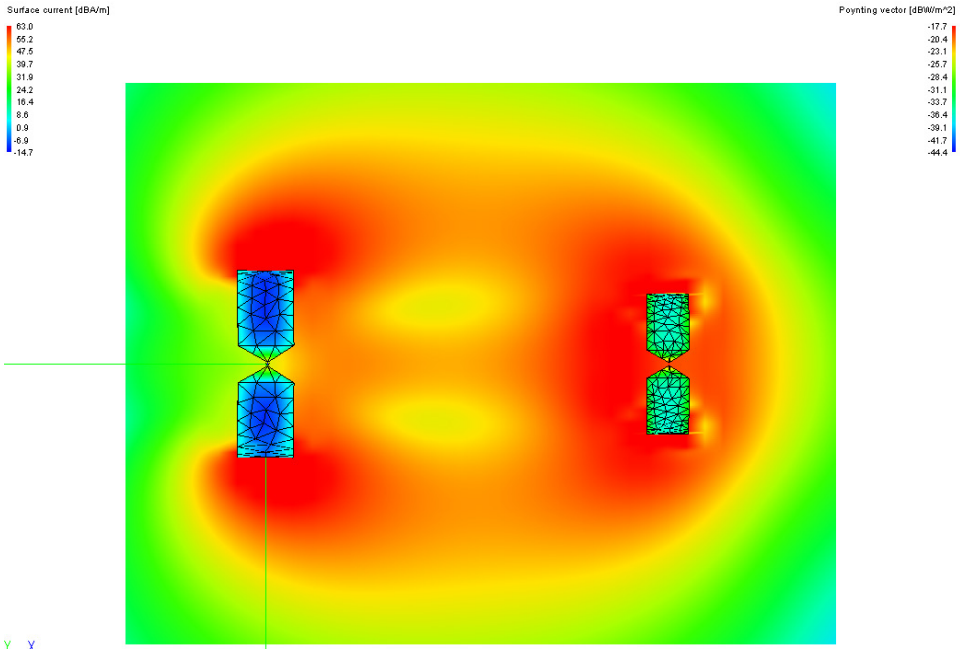

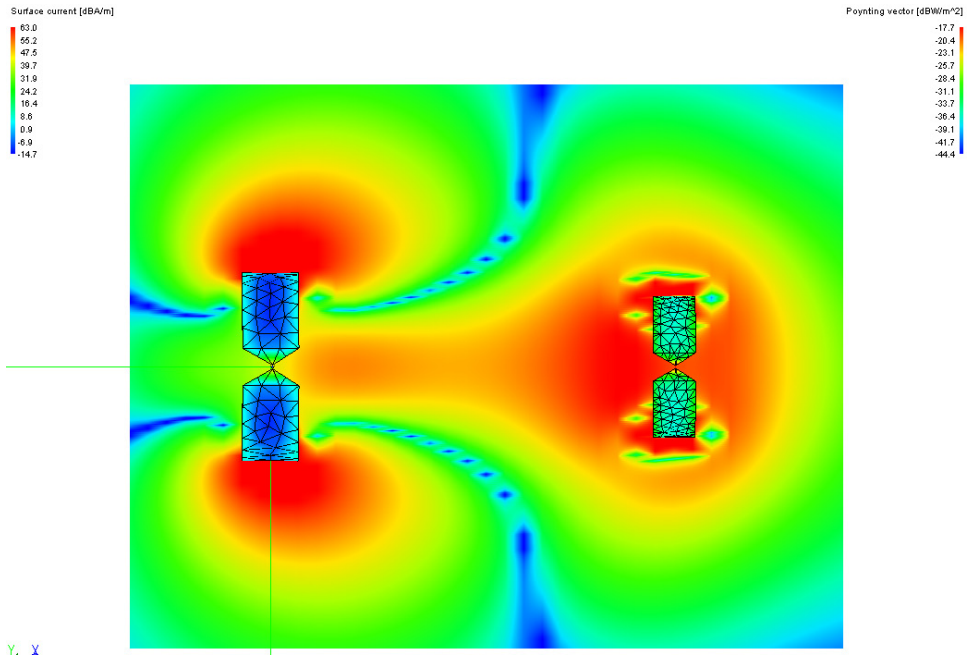
Surface current [dBA/m]
63.0
55.2
47.5
39.7
31.9
24.2
16.4
8.6
0.9
-6.9
-14.7
Poynting vector [dBW/m^2]
-17.7
-20.4
-23.1
-25.7
-28.4
-31.1
-33.7
-36.4
-39.1
-41.7
-44.4
Y
X

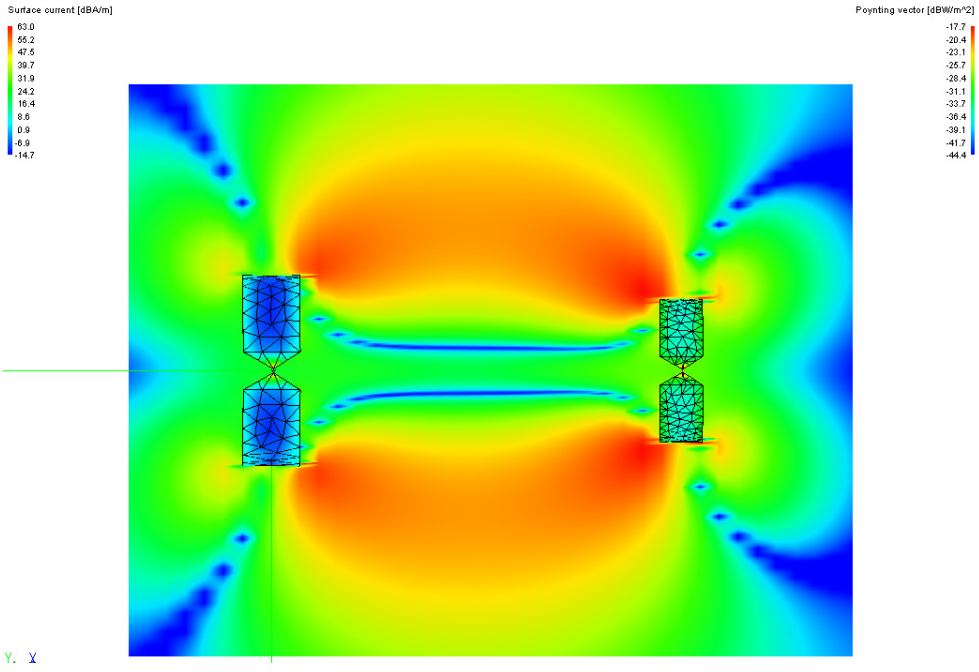
Surface current [dBA/m]
63.0
55.2
47.5
39.7
31.9
24.2
16.4
8.6
0.9
-6.9
-14.7
Poynting vector [dBW/m^2]
-17.7
-20.4
-23.1
-25.7
-28.4
-31.1
-33.7
-36.4
-39.1
-41.7
-44.4
Y
X

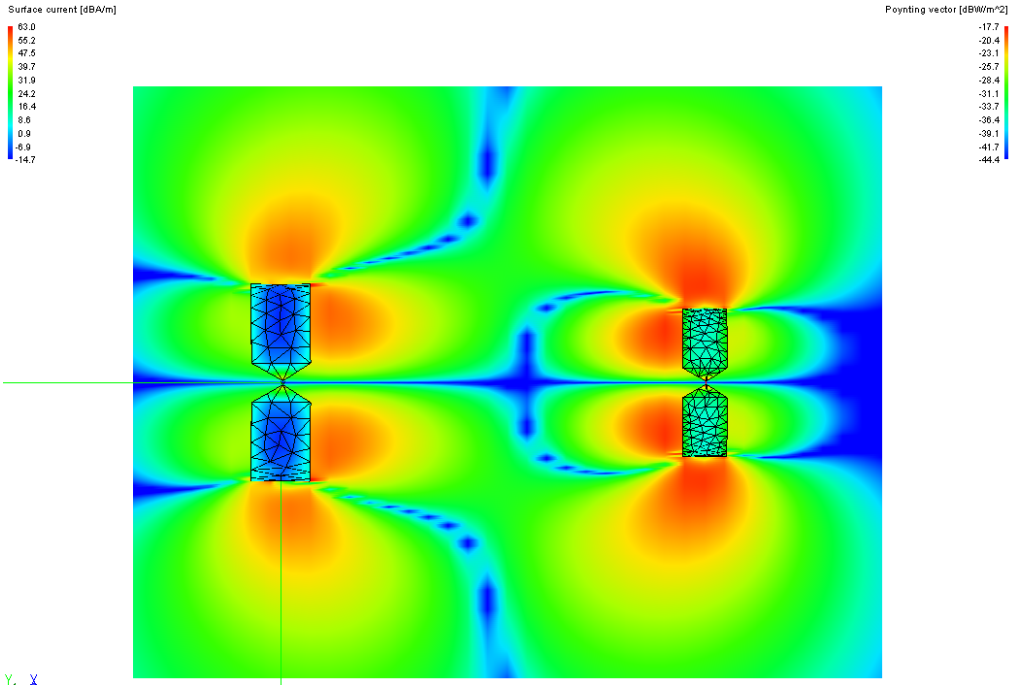


Figure A-79 Field Variations Strip-Loop Full Loop Case
Top: Total Poynting Vector
Middle (top): X-Directed Poynting Vector
Middle (bottom): Y-Directed Poynting Vector
Bottom: Z-Directed Poynting Vector